Massive MIMO for Future Wireless Networks: Energy Efficiency, Interference Management and Symbiotic IoT Networks

by

Mahtab Ataeeshojai

A thesis submitted in partial fulfillment of the requirements for the degree of

Doctor of Philosophy

in

Communications

Department of Electrical and Computer Engineering
University of Alberta

Abstract

Due to the dramatic increase in wireless data traffic and the energy consumption of wireless networks, spectral- and energy-efficient wireless networks are imperative. Using multiple-input multiple-output (MIMO) transceiver structures and cell densification through small cell (SC) deployment increases both spectral efficiency and energy efficiency significantly and meets future network requirements, but also brings new challenges. These are severe interference, limited fronthaul capacity, computational complexity, cost, and power consumption. Promisingly, radio frequency (RF) energy harvesting, that helps technologies such as Internet of things (IoT) to further reduce the power consumption of devices while providing the desired quality of service (QoS), can benefit from MIMO systems in an overlaying network. This thesis designs high spectrum and energy-efficient cellular networks via three main objectives: 1) design and performance evaluation of an energy-efficient network by integrating MIMO and SC deployments with well-designed interference management and resource allocation methods; 2) design and performance evaluation of computationally efficient precoding algorithms for co-located and cell-free (CF) massive MIMO (mMIMO) systems; 3) design and performance evaluation of energy-harvesting IoT networks underlying and symbiotic with massive MIMO cellular networks. First, we focus on maximizing the energy efficiency of a MIMO-enabled heterogeneous cloud radio access network (H-CRAN) as a candidate architecture for beyond 5G cellular systems. A joint radio resource block allocation and antenna selection algorithm is proposed for the SCs, and a single RF chain structure is considered for the mMIMO macro base station (BS). Moreover, while coordinating transmissions between cells

subject to user-centric clustering, an energy-efficient beamforming design, and power allocation optimization problem is formulated and its solution is proposed. Second, we address the implementation complexity of matrix inversion associated with precoding in mMIMO systems. We investigate the convergence of different iterative matrix inversion methods in the presence of small-scale fading, large-scale fading, and spatial correlation and compare their performance and complexity. Third, by considering the coexistence of CF mMIMO and symbiotic backscatter communication and deriving the upper bound for signal-to-interference-plus-noise ratios (SINRs) and also the average harvested power, we provide a novel insight toward efficient implementation of massive machine-type communications (mMTC) use case of 5G and beyond cellular networks.

Preface

The essential content of Chapter 3 has been published in the following journal paper:

- M. Ataeeshojai, R. C. Elliott, W. A. Krzymień, C. Tellambura and J. Melzer, "Energy-Efficient Resource Allocation in Single-RF Load-Modulated Massive MIMO HetNets," in *IEEE Open Journal of the Communications Society*, vol. 1, pp. 1738-1764, Oct. 2020, doi: 10.1109/OJCOMS.2020.3032351.

The essential content of Chapter 4 has been published in the following journal paper:

- M. Ataeeshojai, R. C. Elliott, W. A. Krzymień, C. Tellambura and I. Maljević, "Iterative Matrix Inversion Methods for Precoding in Cell-Free Massive MIMO Systems," in *IEEE Transactions on Vehicular Technology*, 2022, vol. 71, no. 11, November 2022, pp. 11972-11987.

The essential content of Chapter 5 has been submitted as the following journal paper:

- M. Ataeeshojai, R. C. Elliott, W. A. Krzymień, C. Tellambura and I. Maljević, "Symbiotic Backscatter Communication Underlying a Cell-Free Massive MIMO System," submitted (02-12-2022) to *IEEE Internet of Things Journal* (submission ID IoT-27156-2022).

For each publication listed above, I carried out the system model development, the mathematical analysis and computer simulations under the supervision of Prof. Witold Krzymień and Prof. Chintha Tellambura and cooperation with Dr. Robert C. Elliott and Dr. Jordan Melzer (for Chapter 3) and and Dr. Ivo Maljević (for Chapters 4 and 5). I was responsible for the manuscript composition, Dr. Elliott and

Prof. Witold Krzymień and Prof. Chintha Tellambura contributed to its content and writing.

Dedicated to my beloved parents and lovely husband, who have always supported and encouraged me during this journey

Acknowledgements

First and foremost, I would like to express my deepest gratitude to my co-supervisors, Profs. Witold Krzymien and Chintha Tellambura for the amazing opportunity they provided me with. Their effective guidance, consistent support, and timely feedback made the completion of this work possible. I would also like to express my thanks to Dr. Robert C. Elliott for being a patient, knowledgeable and supportive mentor to me throughout my program.

I would also like to thank the members of my final PhD examination committee Profs. Lutz Lampe, Yindi Jing, and Hai Jiang for their invaluable comments on improving this thesis.

I would like to express my gratitude for the financial support that I received from the Natural Sciences and Engineering Research Council (NSERC) of Canada, the Rohit Sharma Professorship, and TELUS. This work has been facilitated by the computing resources of Information Services and Technology (IST) at the University of Alberta, WestGrid, and Compute/Calcul Canada.

Finally, I would like to express my gratitude to my parents and my sisters for their constant love, support, and inspiration that encourages me to move forward and achieve my dreams. Last but not least, my deepest gratitude goes to my husband, Amir, for his unconditional love and support. This journey would not have been the same without his presence by my side.

Table of Contents

List of Tables

List of Figures

List of Symbols

$(\mathbf{A})^H$ Hermitian transpose of matrix $\mathbf{A}$

$(\mathbf{A})^T$ Transpose of matrix $\mathbf{A}$

$(\mathbf{A})^\dagger$ Moore-Penrose pseudoinverse matrix $\mathbf{A}$

$(\mathbf{A})^{-1}$ Inverse of matrix $\mathbf{A}$

$(\mathbf{A})^{1/2}$ Square root of matrix $\mathbf{A}$

$[\mathbf{A}]_{:,b}$ bth column of $\mathbf{A}$

$[\mathbf{A}]_{a,b}$ Element (a, b) of matrix $\mathbf{A}$

$\angle x$ Phase/argument of complex number x

$\lceil x \rceil$ Ceiling operator

$\lfloor x \rfloor$ Floor operator

$\mathbf{0}_n$ All-zero $n \times n$ matrix

$\mathbf{A}$ Matrix

$\mathbf{A}^{\circ 1/2}$ Hadamard (i.e., element-wise) square root of matrix $\mathbf{A}$

$\mathbf{I}_n$ $n \times n$ identity matrix

$\mathbf{a}$ Vector

$\mathcal{A}$ Set

$\odot$ Hadamard product of matrices

$\text{diag}(\mathbf{A})$ Diagonal of matrix $\mathbf{A}$

$\text{tr}(\mathbf{A})$ Trace of matrix $\mathbf{A}$

$\rho(\mathbf{A})$ Spectral radius of matrix $\mathbf{A}$

a Scalar

List of Abbreviations

3GPP 3rd Generation Partnership Project.

5G Fifth generation.

AmBC Ambient backscatter communication.

APs Access points.

BBU Baseband unit.

BC Backscatter communication.

BD Backscatter device.

BER Bit error rate.

BPSK Binary phase shift keying.

BS Base station.

CDF Cumulative distribution function.

CF Cell-free.

CoMP Coordinated multipoint (transmission and reception).

CPU Central processing unit.

CRAN Cloud radio access network.

CSI Channel state information.

DL Downlink.

EE Energy efficiency.

EGC Equal gain combining.

ESPAR Electronically steerable parasitic array radiator.

FDD Frequency division duplex.

GS Gauss-Seidel.

HCRAN Heterogeneous cloud radio access network.

HetNet Heterogeneous cellular network.

HP Hyper-power.

ICT Information and communication technology.

IoT Internet of things.

JC Jacobi.

KKT Karush-Kuhn-Tucker.

LTE-A Long Term Evolution - Advanced.

MIMO Multiple-input multiple-output.

mMIMO Massive MIMO.

MMSE Minimum mean square error.

mMTC Massive machine-type communications.

MR Maximum ratio.

MSE Mean square error.

MU-MIMO Multi-user MIMO.

NLoS Non-line-of-sight.

NS Newton-Schultz.

NSE Neumann series expansion.

OFDMA Orthogonal frequency-division multiple access.

PR Primary receiver.

PS Power-splitting.

PT Primary transmitter.

P-ZF Partial ZF.

P-RZF Partial regularized ZF.

PA Power amplifier.

PPP Poisson point process.

QoS Quality of service.

RB Resource block.

RF Radio-frequency.

RFID Radio frequency identification.

RRH Remote radio head.

RZF Regularized ZF.

SC Small cell.

SE Spectral efficiency.

SIC Successive interference cancellation.

SINR Signal-to-interference-plus-noise ratio.

SNR Signal-to-noise-ratio.

SR Symbiotic radio.

SWIPT Simultaneous wireless information and power transmission.

TDD Time division duplex.

TPS Transmission point selection.

TS Time-splitting.

UE User equipment.

UL Uplink.

URLLC Ultra-reliable low-latency communication.

WSN Wireless sensor networks.

ZF Zero-forcing.

Chapter 1

Introduction

1.1 Future Generation of Wireless Networks

The wireless industry is transitioning to be integrated into every aspect of our daily life. The industry forecasts (Fig. 1.1) global mobile data traffic to grow by a factor of around 4.2 to reach from 67 Exabytes per month in 2021 to 282 Exabytes per month in 2027, and this trend is expected to continue in the future [1]. Increasing numbers of connected devices, which will be more than three times the global population by 2023, and expected dramatic growth of applications such as the Internet of things (IoT), which is continuing to grow from 6.1 billion in 2018 to 14.7 billion by 2023, are the primary contributors to global mobile data traffic growth [2]. Technologies such as IoT are very beneficial in facilitating our lives in various areas such as health care, safety, education, manufacturing, and transportation. Hence, next-generation cellular systems are expected to answer mobile users' increasing capacity demands and quality of service (QoS) requirements.

Beside upsurge in wireless network traffic, there is a sharp increase in energy consumption which necessitates the enhancement of spectral efficiency (SE) while taking power consumption into account. To this end, fifth generation (5G) and beyond 5G networks must increase energy efficiency (EE) commensurate with their improvements to SE [3]. Unfortunately, resources such as spectrum, power, and fronthaul capacity are fundamentally limited, which makes meeting the demands of 5G and beyond 5G

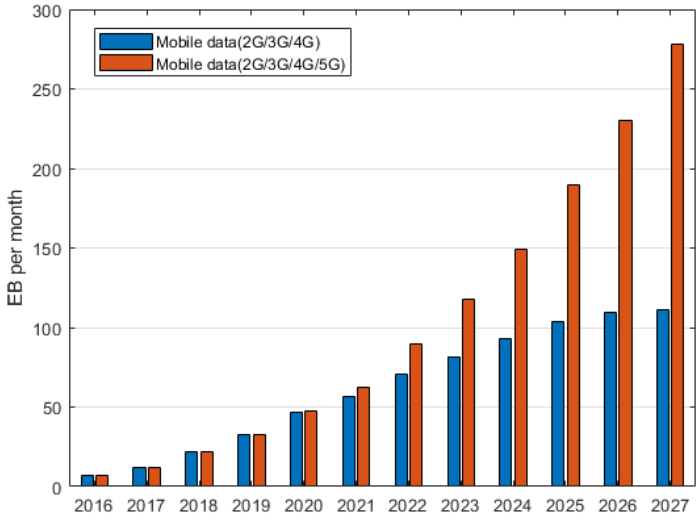

Figure 1.1: Forecast of Ericsson for global mobile data traffic [1]

networks challenging.

One of the foremost ways to accomplish energy and spectrum efficient networks using limited resources is network densification. This broadly refers to increasing the number of antennas per site and deploying smaller cells [4]. This trend is associated with multiple-input multiple-output (MIMO) transceiver structures, small cell (SC) deployment, and advanced interference mitigation techniques.

Efficient deployment of technologies, such as IoT, is also essential for future networks. IoT devices can be powered with energy harvesting, which is of significant research interest due to its potential to provide a ubiquitous energy source [5]. Due to the sensitivity of energy harvesting to propagation loss, beamforming using multi-antenna techniques is a great asset in its efficient use. Finally, while designing spectrum- and energy-efficient future communication networks that satisfy all the requirements is a challenging task, the combination of the technologies and techniques discussed above paves the way forward.

1.1.1 MIMO Wireless Communications

Deploying MIMO significantly improves the capacity and reliability of wireless systems without the need for additional power or spectrum in a rich scattering environment [6]. MIMO offers two fundamental improvements compared to the single-antenna structure - namely array gain and spatial multiplexing gain. Having multiple transmit antennas enables the base station (BS) to steer the signal towards the user via directional beamforming and improves the signal-to-interference-plus-noise (SINR) of every user, which is the array gain. The transmitter can also simultaneously send multiple signals with different directional beamforming vectors, which increases the data rate, which is the spatial multiplexing gain. MIMO can also offer spatial diversity gain, which protects the system against outage by sending redundant streams of information in parallel along multiple spatial paths, which is highly desirable, for instance, in ultra-reliable low-latency communication (URLLC). In particular, large-scale antenna arrays, also known as massive multiple-input multiple-output (mMIMO), are of interest for 5G and beyond systems because of several beneficial features that arise from having many antenna elements. These include increased SE and EE for no additional transmitted power, near-optimal performance of simple linear precoders and detectors [7], and robustness to fading and interference [8]. mMIMO transceivers are supported in the 3rd Generation Partnership Project (3GPP) standards in Release 15 and above [9, 10], and have been commercialized and implemented in practical cellular systems [9].

Like other digital communication systems, mMIMO systems can use two duplex transmission modes; frequency division duplex (FDD), where the uplink (UL) and downlink (DL) transmissions operate at the same time but on significantly separated carrier frequencies and time division duplex (TDD). The UL and DL transmissions use the same frequency band but operate in different time slots. In the FDD mode, the users measure the DL channel and feed back this information to the BSs. In TDD

mode, the BS estimates the UL channel state information (CSI) and then, relying on the radio channel reciprocity in the same frequency band, uses it for the DL precoding [11]. Since this limits the channel estimation overhead, almost all mMIMO systems use TDD. In the mMIMO FDD mode relying on the DL CSI feedback from users, the volume of UL signaling (which is proportional to the number of BS antennas) may become overwhelming [12]. In comparison, since TDD exploits radio channel reciprocity, channel estimation overhead is only proportional to the number of users [13]. However, even with TDD, the number of available orthogonal pilot sequences is limited. In a system where a set of pilot sequences is allocated among L cells having K users per cell and a frequency reuse factor of one, orthogonal pilots need a length of least $K \times L$ symbols. Unfortunately, short channel coherence times because of the mobility of users do not allow for such long pilot sequences and limit the maximum number of mutually orthogonal pilots for large L [14]. Thus, either non-orthogonal pilot sequences must be employed, or sequences must be reused in nearby cells (or a combination of the two). This causes pilot contamination [15], a major performance impairment in mMIMO systems. Numerous works such as [16–18] have studied different techniques to mitigate the interference caused by pilot contamination.

1.1.2 Small-Cell and Heterogeneous Networks

The traditional macrocell networks have approached their limits with ever-increasing demands for higher data rates. While further improvement in SE is possible by increasing the density of macro BSs, it is not viable due to its cost and the lack of available sites [19]. SC deployment is another technique in which by splitting large cells into smaller cells, each with its low power BS and a reduced coverage area, capacity per coverage area increases significantly. Cell splitting increases the capacity of a cellular system since it increases the spectrum reuse per unit area. Also, the link to the end user becomes shorter, which results in reduced path loss and thus higher SE and EE [20].

Underlying macro cellular networks with low-power BSs in a more dense manner leads to the heterogeneous cellular network (HetNet). Thus, a HetNet includes a mix of macrocells, remote radio heads (RRHs), and low power nodes such as picocells, femtocells, and relays, operating within the same frequency band and bringing the access points (APs) closer to end-users. Each cell type may have different specifications, such as transmit power, coverage, backhaul, and responsibilities. For example, macro cells are designed to provide coverage for up to a few kilometers while guaranteeing minimum data rate under maximum tolerable delay for thousands of users. Their transmission power ranges from 5 W to 40 W with a dedicated backhaul, and they can support high mobility users. Picocells serving tens of users within a radio range of 100 m to 250 m are mainly utilized for boosting in-building cellular coverage in environments with low macro penetration and have a typical transmit power range from 0.2 W to 1 W [21]. In general, deploying any SCs helps offload the traffic from macrocells.

Combining the concept of cell splitting by adding more BSs to the designated coverage area and increasing spatial multiplexing by adding more antennas to each BS will satisfy the area throughput requirements of next-generation cellular networks. While macro BS can be equipped with mMIMO, only a few antenna elements are usually sufficient at an AP within each SC covering a smaller area.

While HetNets improve the performance of SCs, their deployment entails many challenges in terms of backhauling, power consumption, and interference management. SC backhaul connections are used to: 1) Forward/receive the SC user data to/from the core network, 2) Exchange mutual information among different SCs. As deployment becomes denser, the aggregated data rate of the SCs is approaching the same data rate level supported by the backhaul links, especially for the cooperative scenarios. These scenarios include coordination of transmission and/or reception at multiple BSs while serving each user, referred to as coordinated multipoint (CoMP) transmission and reception, that enhances the QoS of the users. A comprehensive

overview of the existing wireless backhaul solutions has been provided by [22], where the benefits and challenges of each solution have been discussed. Amongst proposed solutions, using sub-6 GHz spectrum has the benefit of not requiring additional spectrum, new hardware, or antenna alignment, but having a high licensing cost and high vulnerability to interference. Aside from using different spectral regions such as microwave and millimeter-wave, proposing new user association criteria based on the backhaul capacity limitation and utilizing mMIMO for wireless backhauling are other possible solutions that have the potential to improve the performance of wireless backhauling for SCs. On the other hand, while the power consumption of a single SC is smaller than that of a macrocell, the massive deployment of SCs in the 5G cellular network makes the total power consumption of SCs no longer insignificant and even larger than that of an exclusive macrocell network. To reduce the total power consumption of HetNets, transmission power optimization [23], dynamic change of the operating states (SC switch on/off) [24, 25], and antenna selection for SCs have been considered. By nature of the design of HetNet, the system performance is inherently interference-limited, meaning inter-cell interference is the main performance bottleneck. The challenge of interference management and possible solutions will be discussed in more detail next.

1.1.3 Interference Management

The combination of MIMO and SCs overlaying larger cells forms a two-tier MIMO HetNet, which can increase both SE and EE significantly and meet 5G requirements, but also brings new challenges. In practice, the densification of cells may cause severe inter-cell interference, which limits the performance gains. To mitigate interference, increase the cell-edge throughput, and enable the potential gains of HetNets, it is crucial to utilize advanced signal processing techniques; CoMP transmission and reception is a potential solution [26]. This technique has been introduced for Long Term Evolution - Advanced (LTE-A) and standardized by the 3GPP since Release

11 [27]. In DL CoMP, two transmission schemes mainly depend on the information exchanged among the BSs: joint transmission and coordinated beamforming. Joint transmission can be broadly described as the simultaneous transmission of data from multiple coordinated BSs associated with a user. Both data and DL CSI need to be available to all involved BSs. By contrast, coordinated beamforming designs the individual BS precoding to avoid interference to users served by other BSs. Thus, only DL CSI needs to be available to all involved BSs, and data packets that are supposed to be sent to a given user are only available at one BS. Another less common CoMP transmission scheme is called transmission point selection (TPS). In this, while the data packets are available in coordinated BSs, only one of them serves the user at each time instance. Since sharing CSI requires much lower overhead than sharing data, coordinated beamforming needs much lower backhaul capacity than joint transmission [28]. While the amount of shared CSI also depends on the number of antennas in each BS, coordinated beamforming can still occupy less backhaul capacity for a HetNet, primarily including SCs with few antennas.

Deploying CoMP in HetNets adds complexity and signaling overhead and heavily depends on the backhaul constraints and density of SCs. A cloud radio access network (CRAN) or heterogeneous cloud radio access network (HCRAN) design is a potential solution to handle these issues [29]. CRAN is an innovative architecture consisting of baseband units (BBUs) that are in charge of baseband processing, connected to RRHs that act as distributed transceivers and perform radio functions, including frequency conversion, amplification, and analog-to-digital and digital-to-analog conversion. CRAN aggregates numerous BBUs in a central physical pool called a central cloud, so digitalized signals collected by geographically distributed RRHs are transmitted to the cloud via (typically) optical fiber for processing [30]. With this promising architecture, the power consumed in BSs, which is almost 60% of the total power consumed in a typical mobile network [31], will decrease significantly, which is desirable in terms of EE. The more efficient centralized cooling system in the BBU

pool, decreased number of BBUs in comparison to a traditional RAN, and the ability to adapt to nonuniform traffic and utilize the RRHs more efficiently are among the reasons leading to a significant reduction in the total energy consumption [32]. In CRAN, radio resource allocation can be performed jointly for the connected RRHs at the pool. At the same time, coordinated DL transmission in a cluster of SCs can mitigate inter-cell interference within the cluster. In contrast, precoding/beamforming of signals can mitigate intra-cell interference between users.

Although CRANs are commonly envisioned under the assumption of a fiber-based backhaul and/or fronthaul, some network operators have also considered using a wireless backhaul/fronthaul instead. A fiber-based fronthaul is more reliable and has a much larger capacity, but it is impossible to deploy in some environments. The deployment of fiber may also incur substantial costs for installation or leasing, which smaller operators may be unwilling or unable to contend with. In comparison, a wireless fronthaul is cheaper and more flexibly deployed (which also aids cell densification), but has a much smaller and variable capacity. Hence, when optimizing the performance of a network, a limited fronthaul capacity should be accounted for. In [29] and [33], the challenges of mMIMO-enabled H-CRANs are surveyed, and the issues of system architecture, SE and EE performance, and promising key techniques are discussed.

1.2 Cell-Free Massive MIMO Networks

The idea behind designing a cellular network was to make efficient use of the limited spectrum by enabling simultaneous transmissions in the area covered by the network. However, the cell boundaries created as a result of splitting the coverage area into small cells lead to inter-cell interference, which is one of the main causes of the poor cell-edge throughput [34]. One innovative approach is to design a new network architecture that omits these boundaries and makes the implementation of CoMP scalable through coherent user-centric transmission [35]. Cell-free (CF) mMIMO is a form

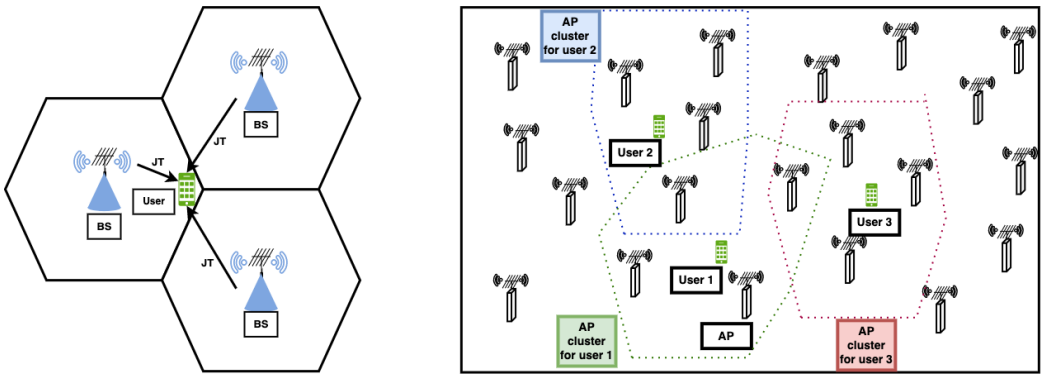

Figure 1.2: Structure of traditional cell-centric CoMP (left figure) vs. user-centric CF mMIMO (right figure)

of distributed mMIMO, in which a large number of geographically distributed low-power access points (APs) are used to jointly serve a set of users that is substantially smaller than the number of APs. In UL, APs transmit the received data from users to the central processing unit (CPU) through the fronthaul link, where various resources can be allocated via centralized processing to improve QoS. In DL, the CPU use backhaul links to send the data and the power control coefficients to APs to perform joint transmission. CF mMIMO is in some regard a "rebranding" of earlier methods also known as distributed antenna systems [36], network MIMO [37], and coordinated multipoint [38] (as discussed in the previous section) to the large-scale antenna array regime. CF mMIMO is at the intersection of mMIMO, CoMP, and ultra-dense networks and benefits from these three technologies' gains. As shown in Fig. 1.2, while traditional CoMP had been performed between adjacent cells and was cell-centric, in CF mMIMO there is no cell boundaries and each user is being served jointly by a cluster of APs that is defined based on channel state of users. Moreover, Clusters of different users can share some APs that overlap. The most significant benefits of cell-free mMIMO compared to conventional cellular networks are smaller signal-to-noise-ratio (SNR) variation, better interference management, and increased SNR due to coherent transmission [34]. Owing to its ability to exploit macro-diversity more efficiently, this distributed architecture can offer a higher probability of coverage

and better SE and EE compared with conventional mMIMO [39, 40]. Moreover, since the cell boundaries are eliminated, there are no cell-edge users in the system, so the system is fairer, and all users will receive uniformly good QoS.

1.3 Internet of Things

IoT is an important paradigm to bridge diverse technologies and enable many connected, intelligent devices to share information and coordinate decisions. The revolutionary applications of IoT include a wide range of domains, such as transportation, healthcare, industrial automation, and so on [41]. Although IoT is expected to be a key part of future 6G networks, massive deployment of IoT devices faces practical challenges caused by their high operational costs, power consumption, and the shortage of spectrum resources [42]. Hence, designing energy- and spectrally-efficient communication techniques for future IoT systems is critical [43].

A promising solution to overcome the hurdle of high power consumption and limited battery lifetime in an IoT device is energy harvesting. It is a simple and effective solution to scavenge energy from sources such as light (solar or man-made), wind, vibrational, thermal, and hydroelectric, and wireless radio frequency (RF) signals resources. Thanks to stability and the availability of ambient wireless signals (TV broadcasting, mobile BS, etc.) and due to uncertainty of the natural resources and their dependence on location, climate, and time, RF powering is considered the most reliable energy harvesting scheme for wireless networks. In RF energy harvesting/scavenging, which performs on-demand gathering of energy from RF signals, energy can be radiated from external sources such as TV towers, BS, or WiFi access points to radio frequency identification (RFID) tags, sensors, actuators, mobile phones, etc. The harvested energy then can be used by IoT devices to charge the battery, process the information, and also for data transmission.

Simultaneous wireless information and power transmission (SWIPT) [44], and backscatter communication (BC) [45] are two major approaches that have integrated

RF-based energy harvesting into wireless communications. While the SWIPT technique is extensively investigated as a viable solution to power energy-constrained user devices (smartphones, tablets, etc.) when transmitting data, BC is used as an enabling solution to pave the way toward efficient deployment of IoT. BC, initially proposed in [46] and later commercially applied in passive RFID systems [47], uses passive reflection and modulation of an incident RF wave while harvesting energy from it [48]. BC systems can be classified into three major types based on their architectures: monostatic BC systems, bistatic BC systems, AmBC systems.

As seen in Fig. 1.3(a), monostatic BC systems include two main components: a backscatter transmitter, e.g., an RFID tag, and an interrogator that consists of both the RF source that emits the wave needed for communication and the receiver that decodes the tag-modulated signals [49]. First, the RF source generates RF signals to activate the tag. Once activated, the backscatter transmitter modulates and reflects the RF signals sent from the RF source to transmit the data to the backscatter receiver. Finally, the transmitted signal is captured by an interrogator, which acts as a backscatter receiver. Since the RF source and the backscatter receiver are placed on the same device, the modulated signals may suffer from a round-trip path loss [50]. Hence, monostatic BC systems coverage is limited, and they are mainly adopted for short-range RFID applications.

Bistatic BC differs from monostatic BC in that the RF source and the backscatter receiver are separated (Fig. 1.3(b)). As a result, in this structure, a doubly near-far effect happens due to the signal loss from the RF source to the backscatter transmitter and also when a backscatter transmitter is located far from the backscatter reader which leads to lower modulated backscatter signal strength [51], can be mitigated by placing several carrier emitters, and the coverage can be expanded [50]. Additionally, the performance of the system can be further improved by placing carrier emitters at optimal locations [52]. Finally, even though carrier emitters are bulky and their deployment is expensive, the fabrication cost of the carrier emitter and backscatter

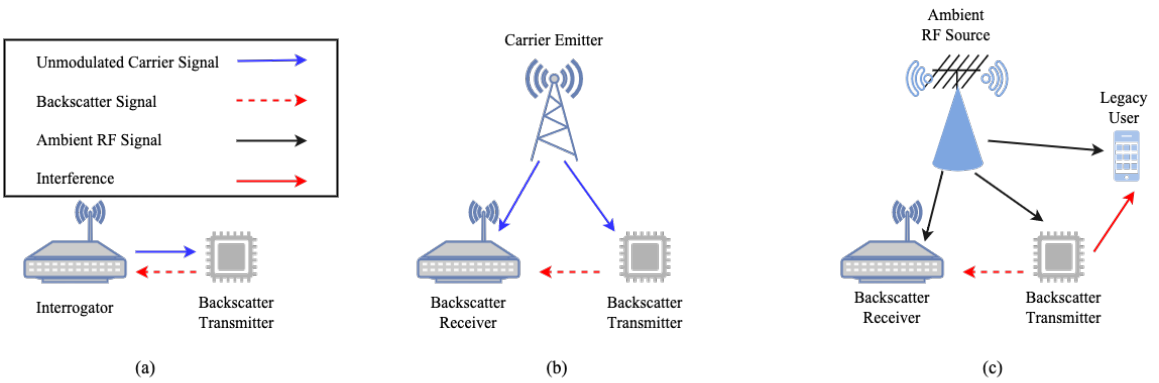

Figure 1.3: Paradigms for different BC configurations. (a)monostatic BC. (b) Bistatic BC. (c) AmBC [49]

receiver in the bistatic configuration is cheaper compared to monostatic configuration due to less complex design [49].

Both above-mentioned backscatter systems use a dedicated RF source supplying the energy and backscattered signal while having different receiver structures. In contrast, AmBC allows passive BDs to modulate their information symbols on top of ambient RF carriers of so-called "legacy" systems (e.g., WiFi, TV, or cellular network signals), while harvesting energy from the legacy signals to power the BD circuitry [53–55]. Power consumption in AmBC is low compared to traditional BC because of having no need for active components, e.g., oscillators, analog-to-digital/digital-to-analog converters, etc. Furthermore, in AmBC, the BD shares the same radio spectrum with the legacy users; thus, no dedicated spectrum is needed. As a result, AmBC offers significant energy and spectrum utilization improvements and is a promising solution for energy-efficient Internet of things [51, 56]. Since the energy transfer is so sensitive to propagation loss and fading, multi-antenna techniques such as beamforming are great candidates as transmission schemes for energy harvesting networks [57].

1.4 Thesis Objectives and Organization

1.4.1 Motivation and Problem Statement

The focus of the thesis is to design communication networks with higher EE, characterized by reduced complexity and lower cost and power consumption. To achieve this goal, we will consider two essential classes of network optimization problems. The first one will involve designing a network architecture that satisfies the requirement of energy-efficient 5G and beyond 5G networks. The second part is system-level optimization, in which developing reduced-complexity, cost and energy-efficient interference management, resource allocation, and user association techniques are of interest.

mMIMO as a key enabler for enhanced SE and EE, is already a part of the 5G standards. To further improve SE and EE, the combination of mMIMO and small cell deployment leads to either a MIMO-enabled HetNet or a CF homogeneous network that both show improved gains in SE and EE. While HetNets are commonly considered for improving the network performance and reflecting modern cellular network layouts, the CF MIMO network may be a key architecture option for a 6G network. The Cellular IoT concept has been introduced in the 5G standard (as the mMTC use case) and IoT devices are currently using 5G access networks, however the advantages offered by CF mMIMO architecture will likely make the deployment of cellular IoT (mMTC) in 6G networks even more effective.

While the previous literature considers the EEmax problem in several scenarios, in this thesis, we combine the factors of massive and small-scale MIMO in a two-tier HetNet, orthogonal frequency-division multiple access (OFDMA), coordinated beamforming, user-centric clustering, antenna selection, and resource block (RB) assignment, transmit power constraints and allocation, minimum data rate constraints, and fronthaul capacity constraints, all together simultaneously. To our knowledge, the examination of a system combining all these factors simultaneously has not been

well investigated before. Our use of the single-RF-chain transceiver structure for the massive MIMO macro BS is also relatively novel, especially in the EEmax context. We formulate a power consumption model for this type of transceiver and examine the EE both of the macro cell and the overall network compared to a traditional transceiver structure with one RF chain per antenna element.

Utilizing the vast number of antennas increases SE and EE thanks to the beneficial features of increased spatial diversity; however, it also creates new implementation issues. One of which is the need for a computationally efficient precoding algorithm. Since iterative methods require less storage and have higher computational time efficiency compared to direct inversion methods such as singular value decomposition and Cholesky factorization, they are good candidates for use in mMIMO systems. Nevertheless, to the best of our knowledge, no prior work has investigated iterative matrix inversion methods for precoding in the context of CF mMIMO. As we shall show, the distributed nature of the antennas and their effect on the channel matrices significantly impact the convergence of some of these methods. In some cases, they may no longer converge for CF mMIMO, despite converging in a conventional co-located mMIMO scenario. Moreover, in contrast to most of the related papers that have only considered small-scale fading, we also include large-scale fading and spatial correlation for a more realistic model of the cellular environment and the channel matrices to be inverted.

While AmBC has received rekindled interest as a cutting-edge technique to provide spectrally- and energy-efficient communications in low-power networks, the obstacle of severe path loss between the transmitters and receivers makes its implementation in wireless networks challenging. The lower average distance to the nearest AP and higher area density of APs makes CF mMIMO a good candidate to implement energy-harvesting-based technologies. While both AmBC and CF mMIMO have the potential to be integrated into future generation wireless standards [58–60], their compatibility with existing technologies needs to be carefully examined. One potential solution to

the complication arising from merging these technologies, due to having numerous antennas and coherent beamforming in mMIMO, is symbiotic radio (SR), which has been proposed based on cooperative AmBC systems [61–63]. In SR, the primary transmitter (PT) of the legacy system designs its transmit beamforming to assist both primary and backscatter device (BD) transmissions, while the primary receiver (PR) decodes information from the BD and the PT. Hence, SR is a promising solution to achieve spectrum-, power- and cost-efficient communications by sharing the spectrum, energy, and infrastructure of the primary system [63]. This thus motivates our current work to consider the amalgamation of CF mMIMO and SR systems.

1.4.2 Thesis Outline and Contributions

This section discusses the organization of the thesis and outlines the contributions of each chapter.

- Chapter 2 reviews the necessary theoretical background for the thesis on mMIMO, CF mMIMO, and BC.

- In Chapter 3, the energy-efficient deployment of MIMO in HCRAN has been considered. To achieve high EE, MIMO and SC deployments need to be integrated with well-designed interference mitigation and resource allocation methods. To this end, we have proposed and investigated the use of user-centric clustering and coordinated beamforming with null-space projection and zero-forcing (ZF) precoding to mitigate interference in a HetNet. A single-RF-chain mMIMO transceiver design for the macrocell and antenna selection for the SCs have been proposed to reduce hardware complexity and power consumption. We have furthermore designed a joint antenna selection and RB allocation algorithm, followed by a power optimization algorithm, to maximize the system EE.

- In Chapter 4, we address matrix inversion associated with precoding in CF

mMIMO systems [34] to tackle the problem of computational complexity. While there are various generic methods for matrix inversion, e.g., Gauss-Jordan elimination, via QR decomposition using Gram-Schmidt and/or Givens rotations methods, etc., the particular Hermitian structure of the matrices inverted in mMIMO precoding leads us to exploit iterative methods to reduce the complexity and make the system more cost- and hardware-efficient. To do so, we examine several iterative methods to calculate the precoding matrix in a CF mMIMO system and investigate their computational complexity and convergence rate in the presence of small- and large-scale fading and spatial correlation between antennas.

- In Chapter 5, we investigate the performance of CF mMIMO in facilitating the implementation of energy-harvesting techniques, where our focus is on symbiotic backscatter communication [63]. To do so, by considering the effects of pilot contamination and spatial correlation between antennas, a two-phase UL pilot training method is proposed. Then, we derive the closed-form expressions for the average SINR ratios for both primary and backscattering transmission under the assumption of correlated Rayleigh fading channel, channel estimation error, pilot contamination and channel hardening. The average power harvested in the BDs is also derived.

- Finally, Chapter 6 summarizes the contributions of the thesis and gives directions for future research.

Chapter 2

Background

2.1 Key Aspects of Massive MIMO Systems

Massive MIMO (mMIMO) systems with hundreds of antennas are seen as one of the critical enablers of the next generation of cellular networks to meet the ever-increasing QoS demands of users and potentially allow for orders of magnitude improvement in SE and EE using relatively simple processing. While initially the focus of MIMO systems was point-to-point communications, where two terminals with multiple antennas communicate with each other (like as shown in Fig. 2.1(a)), further evolution of MIMO systems led to multi-user MIMO (MU-MIMO) systems that are more tolerant of the propagation limitation such as channel rank loss, antenna correlation and LoS propagation environment [64]. As shown in Fig. 2.1(b), a BS with multiple antennas simultaneously serves a set of users in MU-MIMO. Since it offers spatial multiplexing, the spectral efficiency of these systems is much higher than in the point-to-point MIMO case. Finally, to achieve even more dramatic gains and simplify the required signal processing, mMIMO systems have been proposed in [65], where each BS is equipped with hundreds or more antenna elements. mMIMO offers advantages such as: 1) High SE because of significant multiplexing gain and antenna array gain, 2) High reliability because of significant diversity gain, 3) High EE because of the concentration of radiated energy on specific users in DL, and 4) Weak inter-user interference because of orthogonality of users channels and also extremely narrower beam.

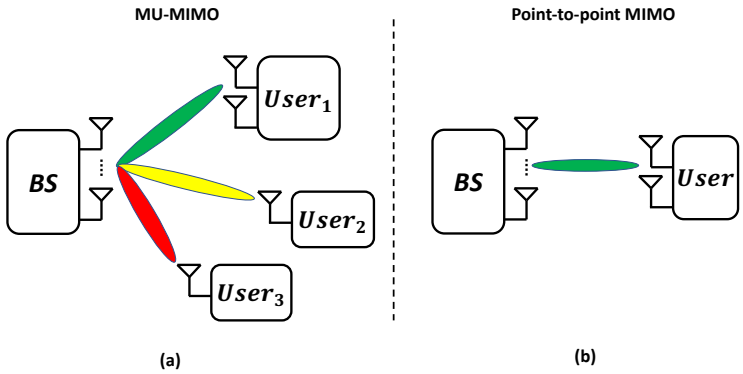

Figure 2.1: Point-to-point MIMO systems vs. MU-MIMO systems

Aside from the advantages of the mMIMO structure, some properties and challenges arise from having many antennas that we define and explain more closely in this chapter.

2.1.1 Favorable Propagation and Channel Hardening

Favorable propagation and channel hardening are concepts that arise from having a large number of antennas and have the merit of simplifying signal processing in an mMIMO network [8]. mMIMO exploits these two properties to multiplex many users in the same time-frequency resource with little inter-user interference. Thus, it can offer a vast spectral efficiency with simple signal processing. The channel hardening and favorable propagation phenomena make the communication performance almost independent of the small-scale fading realizations; it mainly depends on the first and second-order moments of the channels, which represent the large-scale fading [66]. Both phenomena, which are consequences of the law of large numbers, make the utilization of simple signal processing sufficient for the mMIMO system. First, effective channels after combining/precoding become almost immune to small-scale fading, which eases the burden on resource allocation and scheduling [8]. Second, since the users' channel vectors become almost orthogonal, there is no need to design high complexity receive combining and transmit precoding for the MIMO system to manage

the interference and simple linear techniques guarantee near-optimal performances [67].

As the number of BS antennas grows large, the ratio between the number of BS antennas and the number of served users becomes higher, which leads to a set of user channels whose directions are nearly mutually orthogonal that accelerate spatial interference cancellation [68]. Let us consider an mMIMO system with a M-antenna BS and K single antenna receivers with $M >> K$. $\mathbf{h}_i, \mathbf{h}_j \in \mathbb{C}^M$ are the (UL) channel vectors between multi-antenna BS and user i and j, then we have [8]

$$\frac{\mathbf{h}_i^H \mathbf{h}_j}{\sqrt{\mathbb{E}\{||\mathbf{h}_i||^2\}\mathbb{E}\{||\mathbf{h}_j||^2\}}} \to 0 \qquad \text{when} \qquad M \to \infty \tag{2.1}$$

This property is known as favorable propagation and results in the near-optimal performance of linear processing. More precisely, a simple linear detector such as matched filter is sufficient to suppress the noise and interference on the UL. Meanwhile, on the DL, linear beamforming techniques, such as maximum ratio or ZF, allow BS to simultaneously beamform multiple data streams to multiple users without causing mutual interference. In practice, the propagation channels may not offer favorable propagation. However, it is shown in [69] that an approximate form of favorable propagation can be achieved, like in non-line-of-sight scenarios with rich scattering and line-of-sight scenarios with distinct user angles.

Channel hardening is attributed to the high spatial diversity provided by a having multiple antennas [70]. With this phenomenon, the channel behaves almost deterministically and the instantaneous channel gain is well approximated with the average gain. In other words, we have [8]

$$\frac{||\mathbf{h_k}||^2}{\mathbb{E}\{||\mathbf{h_k}||^2\}} \to 1 \qquad \text{when} \qquad M \to \infty \tag{2.2}$$

As a result of this property, the need for adapting the system scheduling, power allocation, and interference management to small-scale fading variations is alleviated. It leaves only the large-scale fading to handle. However, each user still needs its DL

reference signal to estimate its DL CSI if it is expected to perform coherent reception of its data signal. Nevertheless, because of radio channel reciprocity, in propagation environments that channel hardens, the use of pilots for channel estimation on the DL can be avoided, and each user can approximate its instantaneous channel gain by its mean. On the other hand, in propagation environments like a keyhole channel without hardening, DL pilots can still be avoided by utilizing blind channel estimation algorithms like the algorithm proposed by [11].

2.1.2 Spatial Channel Correlation

Let us consider the channel response between BS L with M antennas and user K with one antenna is denoted by $\mathbf{h}_{lk} \in \mathbb{C}^M$. Then the fading channel $\mathbf{h}_{lk}$ is called spatially uncorrelated if the channel gain and the channel direction are independent random variables and the channel direction is uniformly distributed over the unit sphere in $\mathbb{C}^M$ [8]. In other words, there is no correlation in the channel responses between user k and any two different antennas at the BS. In practice, the assumption of uncorrelated channels for mMIMO systems is unrealistic. Whether due to the lack of sufficient scattering in the local environment around the APs, non-uniform radiation patterns of antennas or insufficiently separated antennas, some spatial directions become more probable to carry strong signals from the transmitter to the receiver than other directions and the small-scale fading channel gain vector for any given user will exhibit spatial correlation.

Let us assume we have a non-line-of-sight (NLoS) channel between BS l equipped with M antennas and user k where the small-scale channel fading is modeled as Rayleigh fading. Then, a spatially correlated Rayleigh fading channel vector is

$$\mathbf{h}_{lk} \sim \mathcal{CN}(\mathbf{0}, \mathbf{R}_{lk}), \tag{2.3}$$

where $\mathbf{R}_{lk}$ is the correlation matrix and covariance matrix. $\mathbf{R}_{lk}$ is characterized by its eigenstructure in which large eigenvalue variations indicate the spatial directions

that are more likely to contain strong signal components. For the special case of uncorrelated channels, the correlation matrix simplifies as $\mathbf{R}_{lk} = \mathbf{I}_M$.

Modeling spatial correlation, as an important property of a mMIMO system, is the first step in capturing its impact on the performance of the system. Here we explain a rather simple model where the idea is to parameterize the subspaces of the correlation matrices by the azimuth angles to the UEs to determine if two UEs are spatially separable by comparing their respective angles. By assuming macro BS antennas to be higher up, such that scatterers are located only near the users (i.e., localized scattering), we can model $\mathbf{R}_{lk}$ as proposed by [8, Eq. (2.22)]:

$$\begin{aligned}\mathbf{R}_{lk} &= \sum_{n=1}^{N} \mathbb{E}\{|b_n|^2\}\mathbb{E}\{\exp\left[2\pi j d_H(m-1)\sin(\bar{\phi}_n) - 2\pi j d_H(m'-1)\sin(\bar{\phi}_n)\right]\} \\ &= \int \exp\left[2\pi j d_H(m-m')\sin(\bar{\phi})\right] f(\bar{\phi}) d\bar{\phi}\end{aligned} \tag{2.4}$$

where b_n accounts for the gain and phase rotation on path n, m and m' are indices of two different antenna elements at BS l, d_H is the antenna spacing (in number of wavelengths), and $\bar{\phi}_n$ is the angle of the nth multipath component. Since we assumed BS antennas to be located on the top of a tall tower, it is reasonable to assume further that all the multipath components originate from a scattering cluster around the UE as shown in Fig. 2.2. Then $\bar{\phi}$ can be defined as $\bar{\phi} = \varphi + \delta$, where φ is a deterministic nominal angle (in radians) between the user and the antenna array and δ is a random deviation from the nominal angle with standard deviation σ_φ. By assuming $\delta \sim \mathcal{N}(0, \sigma_\varphi^2)$, (5.38) can be simplified as

$$\begin{aligned}\mathbf{R}_{lk} &= \int \exp\left[2\pi j d_H(m-m')\sin(\varphi+\delta)\right] \frac{1}{\sqrt{2\pi}\sigma_\varphi} \exp\left[\frac{-\delta^2}{2\sigma_\varphi^2}\right] d\delta \\ &= \exp\left[2\pi j d_H(m-m')\sin(\varphi) - \frac{\sigma_\varphi^2}{2}\left(2\pi d_H(m-m')\cos(\varphi)\right)^2\right]\end{aligned} \tag{2.5}$$

that is valid when σ_φ is small, e.g., below $\frac{\pi}{12}$ radians (15°). It is worth mentioning that both (5.38) and (2.5) are derived by using some simplifying assumptions

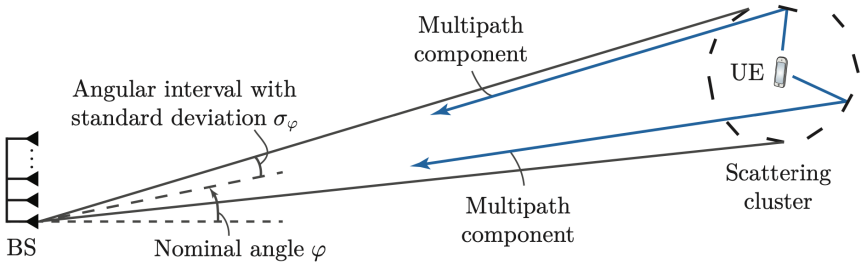

Figure 2.2: Illustration of NLoS propagation under the local scattering model, where the scattering is localized around the UE (cf. [8])

such as uniform linear array at the BS to enable comparison between correlated and uncorrelated cases.

2.1.3 Computational Complexity

Utilizing the vast number of antennas (or APs) mitigates many problems thanks to increased diversity benefits; however, it also creates some new implementation issues, one of which is a computationally efficient precoding algorithm. In the mMIMO regime, the channel directions to any two users will typically become asymptotically orthogonal as the antenna array size becomes large. For this reason, linear precoders such as ZF and minimum mean square error (MMSE) are sufficient to achieve near-optimal performance [71], but involve matrix inversion with high complexity. The issue becomes especially complicated since the dimension of mMIMO systems is large; direct inversion of an $N \times N$ matrix generally has an order of complexity of $\mathcal{O}(N^3)$ [72]. Several approaches exist to reduce the computational complexity of matrix inversion while indirectly obtaining an approximate solution in mMIMO systems. These approaches can be classified as series expansion, gradient-type and iteration-type [73]. Since iteration-type has less complexity than gradient-type methods, such as steepest descent and offers better performance than series expansion like Neumann series expansion (NSE), they are good candidates for use in practical mMIMO systems. Amongst the well-known iteration-type methods to find the inverse of a matrix,

we can mention Jacobi (JC), Gauss-Seidel (GS), Newton-Schultz (NS).

The authors of [74] have proposed an NSE method to approximate ZF precoding for an mMIMO system. In this method, inverting matrix $\mathbf{M}$ starts from a preconditioned initial matrix; this initial matrix can be a scaled identity matrix [74] but is more typically found by inverting a sparse matrix consisting of only a few elements from $\mathbf{M}$. Examples include the main diagonal elements [74], the tridiagonal elements [75], and the main diagonal plus first column [76]. Nevertheless, NSE has a significant downside of its special bit error rate (BER) performance loss. Better performance requires using more terms in the Neumann series and/or more complicated preconditioning; either would increase the complexity. A symbol detection algorithm for the mMIMO UL based on the JC method has been proposed in [77]. It has been demonstrated in [78] that the JC method outperforms NSE when used for precoding. However, JC converges linearly with the number of iterations [79], which leads to slow convergence. To speed up the convergence, several related methods, such as a joint steepest descent and JC algorithm [80], a joint conjugate gradient and JC algorithm [73], and a damped JC method [81] have been proposed for DL and UL of mMIMO systems. The authors of [82] have proposed a near-optimal signal detection algorithm for mMIMO systems based on the GS method, along with a diagonal-approximate initialization point. Although this method offers fast convergence with low computational complexity, the GS method's internal sequential iteration structure makes parallel implementation difficult, if not impossible. An NS algorithm for ZF detection in mMIMO systems has been introduced for faster convergence in [83]. The convergence time of this method is strongly dependent on the initialization point for the matrix inversion solution, so [83] has also proposed an initialization point using a Chebyshev polynomial. The authors of [84] have proposed a diagonal band Newton iteration matrix inversion method for signal detection, which reduces the complexity to $\mathcal{O}(N^2)$. An improved Schultz-type iterative method has also been proposed in [85], wherein its convergence and computational complexity have been investigated. Based

on the HP method, a generalized form of the NS algorithm has been proposed in [86] for mMIMO detection to avoid direct matrix inversion. While examining these methods' convergence, dependency on preconditioning, sensitivity to spatial correlation, and compatibility with parallel implementation need to be investigated. It is worth mentioning that while most of the related works have only considered small-scale fading, it is necessary to include large-scale fading and spatial correlation for a more realistic model of the cellular environment and the channel matrices to be inverted.

2.1.4 Hardware Complexity

In a traditional digital transceiver structure, an RF chain is connected to each transmit antenna element. Thus, dynamic circuit power, which refers to the power consumed in the RF chains connected to the antenna elements, is proportional to the number of transmit antenna elements. Our goal is to develop strategies to decrease consumed power and potentially increase the EE of the network. For SC BSs, as they have relatively few transmit antennas compared to the macro BS, the optimal transmit antenna selection can decrease the number of antennas, and higher EE is achievable. However, for mMIMO, antenna selection is not as viable of an option. Since the mMIMO system needs to have a large number of active antenna elements (this number is typically assumed to be around an order of magnitude larger than the number of served users) to obtain its benefits (e.g., very narrow spatial beams, near-orthogonal channel directions, etc. [8]), dynamic power consumption increases drastically and affects the EE performance of the system. Hence, hybrid analog-digital transceivers have been proposed to reduce hardware complexity, cost, and energy consumption in mMIMO systems by reducing the number of RF chains [87]. However, although hardware cost and complexity may be reduced, the analog portion of the structure requires power for its operation. It further introduces power losses, dependent on the number of transceiver antennas and RF chains, that must be considered while calculating power consumption. Thus, the reduction in the power consumption

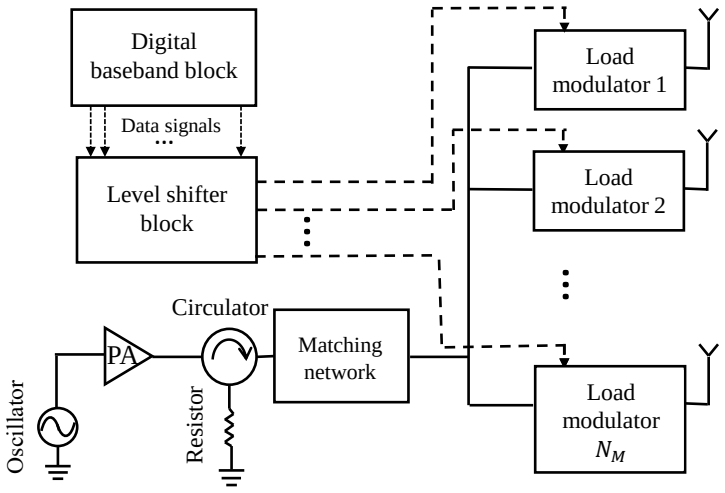

Figure 2.3: Single-RF-chain load-modulated mMIMO transceiver (cf. [90],[91],[92]).

is usually much less than initially expected, and generally, the fully digital structure outperforms the hybrid solution from both SE and EE perspectives [88]. Therefore, a new transceiver structure with a limited number of RF chains needs to be designed to facilitate the practical implementation of an mMIMO system. To this end, an alternative structure called a single-RF-chain load-modulated transceiver has been introduced in [89, 90], that has the potential for addressing the issues of hardware complexity and EE of mMIMO transmitters.

In the load-modulated transceiver structure, as shown in Fig. 2.3, each antenna element is connected to a single common power amplifier (PA) via a load modulator. Each load modulator is a lossless, reciprocal, two-port network with adjustable complex impedance parameters. Adjusting these parameters changes the complex-valued current that flows to each antenna and thus determines the complex-valued symbol sent from that antenna. Since the load modulator parameters can be set independently for each antenna, this allows the transceiver to support any arbitrary modulation type and achieve the array's full spatial multiplexing gain. The PA outputs a constant-amplitude sinusoid. The transceiver can use a Class F PA, reaching an efficiency of about 80% [93]. In order to protect the PA against reflected power,

a circulator and matching network are added between the PA and load modulators. Some slight variations in the design are presented in [91] and [92]. The authors of [94] have compared a load-modulated transmitter with another single-RF structure implemented using electronically steerable parasitic array radiator (ESPAR) antennas. It was shown that the load-modulated design reduced the power consumption by $50-81\%$ and yielded $5-42\%$ lower bit error rates than the ESPAR-based scheme. A physical implementation of a load-modulated transmitter with four antennas was demonstrated in [95]. The authors of [96] have proposed novel multiuser precoding techniques for a BS equipped with load-modulated arrays, such that both distortion and bit error performance of the system have improved. A novel multiantenna transmitter architecture has been proposed in [97], in which load-modulated arrays and channel modulation have been utilized to realize high data rates. Moreover, this work also proposed a message-passing detector on the UL that offers the advantage of RF hardware simplicity at the user equipment and the need for fewer receive antennas at BSs to achieve desired BER performance. Overall, the single-RF-chain transceiver can potentially address the issues of hardware complexity and EE of mMIMO transmitters.

2.2 Cell-Free Massive MIMO System

CF mMIMO systems are an alternative topology for mMIMO deployment, wherein many APs are distributed over the coverage area to serve users jointly. As a homogeneous network with its roots at the intersection of MIMO, CoMP, and ultra-dense networks and has CRAN as its foundation, CF mMIMO has been demonstrated to be more energy efficient than its cellular counterpart if a proper power control strategy is employed [39]. In this architecture, the cell boundaries are omitted, so there is no inter-cell interference in the traditional sense, and the service quality is more uniform over the coverage area.

Let us consider a conventional CF mMIMO system in TDD operation with a large

number (L) of geographically-distributed low-power APs having a total of M antennas jointly serving a set of K users, where $M \gg K$. All the L APs are connected to the CPU via fonthaul links, where necessary computations for AP cooperation, such as synchronization, are performed. The CPUs are then interconnected directly or connected to the core network via backhaul links.

The DL channel gain vector $\mathbf{g}_{lk}$ between user k and AP l can be expanded as

$$\mathbf{g}_{lk} = \sqrt{\beta_{lk}}\mathbf{h}_{lk}, \tag{2.6}$$

where β_{lk} is the large-scale fading channel gain that accounts for path loss and shadow fading, and $\mathbf{h}_{lk} \in \mathbb{C}^{1\times N}$ is the small-scale fading channel gain vector. Since the values of $\beta_{lk}, \forall(l,k)$ are constant over multiple coherence time intervals, we assume they are estimated *a priori* and known whenever required. By writing the complete channel gain as a matrix, we have

$$\mathbf{G} = \mathbf{B}^{\circ 1/2} \odot \mathbf{H} = \begin{bmatrix} \sqrt{\beta_{11}} & \dots & \sqrt{\beta_{1M}} \\ \sqrt{\beta_{21}} & \dots & \sqrt{\beta_{2M}} \\ \vdots & \dots & \vdots \\ \sqrt{\beta_{K1}} & \dots & \sqrt{\beta_{KM}} \end{bmatrix} \odot \begin{bmatrix} h_{11} & \dots & h_{1M} \\ h_{21} & \dots & h_{2M} \\ \vdots & \dots & \vdots \\ h_{K1} & \dots & h_{KM} \end{bmatrix}. \tag{2.7}$$

We also denote the kth row of $\mathbf{H}$, i.e., the small-scale fading channel gain (row) vector for user k from all APs, as $\mathbf{h}_k \in \mathbb{C}^{1\times M}$. Under the assumption of correlated Rayleigh fading, $\mathbf{h}_k$ is distributed $\sim \mathcal{CN}(\mathbf{0}, \mathbf{R}_k)$, where $\mathbf{R}_k = \mathbb{E}\{\mathbf{h}_k^H \mathbf{h}_k\} \in \mathbb{C}^{M\times M}$. In the case of completely distributed CF mMIMO (single-antenna APs), all APs can be assumed to be far enough apart that there is no correlation between their antennas. Hence, the correlation matrix, in this case, would be $\mathbf{R}_k = \mathbf{I}_M$. For partially-distributed CF mMIMO (multi-antenna APs), we assume that channel gains are uncorrelated between APs, but there is a correlation between the antennas co-located at each AP. Hence, if each AP has N antenna elements, the correlation matrix in this scenario can be expressed as

$$\mathbf{R}_k = \begin{bmatrix} \mathbf{R}_{1k} & \mathbf{0}_N & \dots & \mathbf{0}_N \\ \mathbf{0}_N & \mathbf{R}_{2k} & \dots & \mathbf{0}_N \\ \vdots & \vdots & \ddots & \vdots \\ \mathbf{0}_N & \mathbf{0}_N & \dots & \mathbf{R}_{Lk} \end{bmatrix}, \tag{2.8}$$

where $\mathbf{R}_{lk} = \mathbb{E}\{\mathbf{h}_{lk}^H \mathbf{h}_{lk}\} \in \mathbb{C}^{N \times N}$.

2.2.1 Channel Estimation

The performance of mMIMO systems heavily depends on the acquisition of CSI, so that the first step would be channel estimation. We assume that the CF mMIMO system uses TDD transmission mode. Thus, it can be assumed that UL/DL radio channel reciprocity holds, and the DL channel matrix is the Hermitian transpose of the UL channel matrix. Accurate estimation of these channels at the APs is necessary to benefit from mMIMO; the channels are estimated via pilot signals sent from the users. Unfortunately, orthogonal pilot sequences may not be enough to assign a unique one to every user in the system. This leads to errors in channel estimation, known as pilot contamination. While exhaustive search methods usually get the best pilot assignment, they have exponential computational complexity. There are simple schemes in the literature, such as the one described in [34, Ch. 4.4] to assign pilots and determine which APs serve which users. This scheme mitigates pilot contamination by ensuring that users who share pilot sequences are distant from each other. Any given AP only serves one of the users out of however many share that sequence.

With pilots assigned, the UL channels can be estimated. First, all users simultaneously and synchronously transmit their pilot sequences, which all APs receive. Let $\boldsymbol{\psi}_k \in \mathbb{C}^{\tau \times 1}$ be the pilot sequence sent by user k, with length τ and $||\boldsymbol{\psi}_k||^2 = \tau, \forall k$. The received pilot signal $\mathbf{Y}_n \in \mathbb{C}^{N \times \tau}$ at AP l is

$$\mathbf{Y}_l = \sum_{k=1}^{K} \sqrt{\rho_k}\, \mathbf{g}_{lk} \boldsymbol{\psi}_k^T + \mathbf{N}_l, \tag{2.9}$$

where ρ_k is the pilot transmit power for user k and $\mathbf{N}_l \in \mathbb{C}^{N\times\tau}$ is an additive noise matrix, whose elements are independent and identically distributed (i.i.d.) $\sim \mathcal{CN}(0, \sigma_l^2)$.

To estimate $\mathbf{g}_{lk}$ of user k, AP l correlates $\mathbf{Y}_l$ with the pilot sequence $\boldsymbol{\psi}_k$, which cancels the interference from all other pilot sequences. Let $\mathcal{S}_k$ denote the set of all users sharing the same pilot sequence as user k (including k). Then, the correlated pilot signal $\mathbf{y}_{lk} \in \mathbb{C}^{N\times 1}$ can be written as [34]

$$\mathbf{y}_{lk} = \mathbf{Y}_l \frac{\boldsymbol{\psi}_k^*}{\sqrt{\tau}} = \sum_{k'\in\mathcal{S}_k} \sqrt{\rho_{k'}\tau}\, \mathbf{g}_{lk'} + \mathbf{n}_{lk}, \tag{2.10}$$

where $\mathbf{n}_{lk} \sim \mathcal{CN}(0, \sigma_l^2 \mathbf{I}_N)$.

Then, the minimum mean square error (MMSE) estimate of $\mathbf{g}_{lk}$ can be calculated as [8]

$$\hat{\mathbf{g}}_{lk} = \sqrt{\rho_k \tau}\, \mathbf{R}_{lk} \boldsymbol{\Theta}_{lk}^{-1} \mathbf{y}_{lk}, \tag{2.11}$$

where

$$\boldsymbol{\Theta}_{lk} = \sum_{k'\in\mathcal{S}_k} \rho_{k'} \tau \mathbf{R}_{lk'} + \sigma_l^2 \mathbf{I}_N \tag{2.12}$$

is the covariance matrix of $\mathbf{y}_{lk}$, and $\mathbf{R}_{lk'}$ denotes the covariance matrix of $\mathbf{g}_{lk'}$. As can be seen in (5.4) and (2.12), the coherent interference caused by users sharing the same pilot makes the channel estimates statistically dependent, which hinders the BS's ability to separate them.

Let $\tilde{\mathbf{g}}_{lk} = \mathbf{g}_{lk} - \hat{\mathbf{g}}_{lk}$ denote the channel estimation error. Based on a property of MMSE estimation, $\hat{\mathbf{g}}_{lk} \sim \mathcal{CN}(\mathbf{0}, \hat{\mathbf{R}}_{lk})$ and $\tilde{\mathbf{g}}_{lk} \sim \mathcal{CN}(\mathbf{0}, \tilde{\mathbf{R}}_{lk})$ are independent random variables, and their covariance matrices are respectively given by [8]

$$\hat{\mathbf{R}}_{lk} = \rho_k \tau \mathbf{R}_{lk} \boldsymbol{\Theta}_{lk}^{-1} \mathbf{R}_{lk}, \tag{2.13}$$

$$\tilde{\mathbf{R}}_{lk} = \mathbf{R}_{lk} - \hat{\mathbf{R}}_{lk}. \tag{2.14}$$

2.2.2 Precoding

Now that APs have obtained instantaneous CSI from UL pilot signals, the next step would be utilizing them to construct the precoding vectors. Precoding is performed

to direct the signal spatially toward the desired user by sending each data signal from all antennas, but with different amplitude and phase. It is essential to the operation of MIMO, especially for mMIMO either co-located or distributed like CF mMIMO. By assuming the DL of a CF mMIMO system consisting of L APs, each equipped with N antennas serving K single-antenna users, the received signal $y_k \in \mathbb{C}$ at user k is

$$y_k = \sum_{l=1}^{L} \mathbf{g}_{lk} \mathbf{x}_l + n_k, \tag{2.15}$$

where $\mathbf{g}_{lk} \in \mathbb{C}^{1\times N}$ is the complex channel gain vector between user k and AP l, $\mathbf{x}_l \in \mathbb{C}^{N\times 1}$ is the complex-valued transmitted signal from AP l, and $n_k \sim \mathcal{CN}(0,1)$ is additive white Gaussian noise. The signal transmitted by AP l is

$$\mathbf{x}_l = \sqrt{p_t} \sum_{k=1}^{K} \sqrt{\eta_{lk}} \mathbf{w}_{lk} s_k, \tag{2.16}$$

where p_t is the total normalized transmit power (normalized relative to the noise power) of each AP, η_{lk} is a power coefficient, representing the fraction of its maximum transmit power that AP l allocates to the data for user k, s_k is the data symbol intended for user k, with $\mathbb{E}\{|s_k|^2\} = 1$, and $\mathbf{w}_{lk} \in \mathbb{C}^{N\times 1}$ is the precoding vector at AP l for user k. While designing the precoding vectors, we must consider that in contrast to co-located mMIMO, the power constraint is per BS; in CF mMIMO, the power constraint is per AP. In other words,

$$\mathbb{E}\{||\mathbf{x}_l||^2\} \leq p_t \qquad l = 1, ..., L \tag{2.17}$$

There are two types of precoding in CF mMIMO: centralized precoding and distributed precoding. As shown in Fig. 2.4, in the centralized precoding, the CPU has the CSI of all APs, so it designs the precoding vectors such that the APs suppress each other's interference at undesired users. In a distributed precoding, the CSI is available locally in each AP, and the only way to mitigate interference is to make each AP's interference on undesired users small.

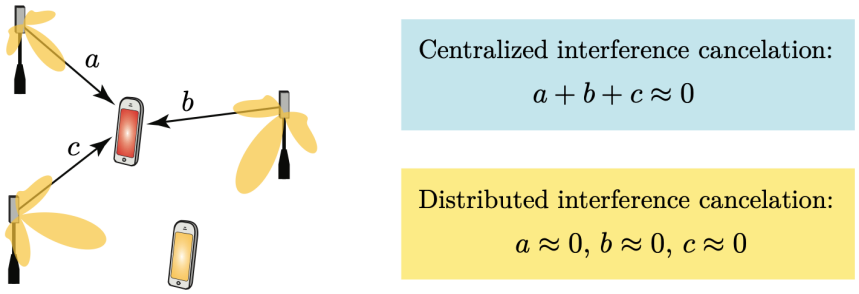

Figure 2.4: Centralized precoding vs. distributed precoding in a CF mMIMO. The yellow beams are intended for the yellow user while causing interference to the red user (cf. [34]).

Centralize Precoding: In the centralized operation, the CPU utilizes the channel estimates obtained from UL pilot signals to design the precoding vectors and compute the signals to be transmitted for all the K users in the network. In other words, the CPU performs all the signal processing for channel estimation and precoding, while the APs are only responsible for transmitting the signals. As a result, the signals transmitted from multiple APs can be coherently received at each UE, and the APs can mitigate out each others' interference.

- **ZF:** ZF precoding is one of the most popular precoding methods in the context of mMIMO systems. ZF precoding aims at preventing a signal sent to a given user from causing interference on any of the other users simultaneously served jointly by the APs. To implement ZF precoding, we set $\mathbf{W}$ as [71]:

$$\mathbf{W} = \mathbf{G}^{\dagger} = \mathbf{G}^{H}(\mathbf{G}\mathbf{G}^{H})^{-1}. \tag{2.18}$$

  As can be seen, the ZF precoding matrix is proportional to the pseudo-inverse of the estimated channel matrix. This scheme fully nullifies the multi-user interference and is especially beneficial in a high SNR regime.

- **RZF:** The idea behind regularized zero-forcing (RZF) precoding is to keep a balance between transmitting a strong signal to the desired user and limiting the interference caused to other users by minimizing the mean-squared error

(MSE) of the desired signals. To implement RZF precoding, we set

$$\mathbf{W} = \mathbf{G}^{\dagger} = \mathbf{G}^{H}(\mathbf{G}\mathbf{G}^{H} + \sigma^{2}\mathbf{I}_{K})^{-1}. \tag{2.19}$$

While the centralized precoding schemes show near-optimal performance and preserve the channel hardening property in a CF mMIMO system, one of the main obstacles in implementing these schemes is the fronthaul signaling load caused by the CPU being responsible for all computations. As discussed above, in centralized operation the APs compute the estimates of the channels and/or send the received pilot signals to the CPU in the UL and, in the DL, receive the superposition of the precoded data signals from the CPU, which leads to huge signaling load [34].

Distributed Precoding: In the distributed operation, each AP receives from the CPU via fronthaul link encoded signals to be transmitted on the DL and utilizes locally available channel estimates to design precoding vectors by itself. While the signals transmitted from all APs are coherently received at each user, the inter-user interference suppression capability is limited since using distributed precoding each AP can only suppress the interference that it is generating itself, because it does not know of others' channels. Since the CPU does not have access to CSI in the UL, each AP applies combining methods locally and sends its data estimates via the fronthaul to the CPU to make the final decoding.

- **Conjugate beamforming:** The simplest distributed precoding scheme is called conjugate beamforming/ MR precoder. This scheme maximizes the transmitted power from AP l to user k, but ignores the interference that the AP is causing to other serving users. MR precoding vector is proportional to the conjugate of the estimated channel matrix, so we have

$$\mathbf{w}_{lk}^{MR} = \mathbf{g}_{lk}^{H} \tag{2.20}$$

While this scheme is less complex compared with centralized precoding and puts

less burden on the fronthaul link, in CF mMIMO, a conjugate/ MR precoder is insufficient to achieve satisfactory performance [34]. It poorly contributes to hardening the effective channel at the users [98].

- **Enhanced normalized conjugate beamforming (ENCB):**

  As discussed earlier, because of having a large number of antennas, the channels undergo channel hardening in an mMIMO system [8, 34], such that the fluctuations in the channel gains around the mean become small. Unfortunately, [67] shows that the degree of channel hardening in CF mMIMO systems can be considerably smaller than in co-located mMIMO systems. To this end, the authors of [98] have proposed a variant of conjugate beamforming dubbed ENCB, in which the conjugate beamforming vector is normalized by the squared norm of the channel as

$$\mathbf{w}_{lk}^{ENCB} = \frac{\mathbf{g}_{lk}^{H}}{||\mathbf{g}_{lk}||^2} \tag{2.21}$$

  This normalization enhances the effect of channel hardening, which improves the reliability of decoding data relying only on statistical CSI.

2.2.3 Scalable Cell-Free Massive MIMO

Up to this point, we have assumed that APs have the CSI of all the users in the network and also CSI of all APs are available for each user, and that all APs transmit to all users simultaneously. Even though these assumptions are convenient for analysis, in practice, for a given user, there are many APs that are far away and do not contribute significantly to its overall received signal. Moreover, these assumptions lead to immense fronthaul signaling, enormous computational complexity, and power consumption [99]. Consequently, the network could not be scaled to an arbitrarily large size. For these reasons, not all APs need to participate in serving each user, and each user can be served only by an AP subset. It is shown in [100] that AP selection in the CF mMIMO can

also improve the EE of the system by reducing the power consumption caused by the backhaul links. By proposing two metrics to measure the channel quality of users and the effective channel gain between users and APs, an effective channel gain-based AP selection algorithm has been developed in [101]. This algorithm outperforms other algorithms when the number of users to the number of APs is high, which is the case for CF mMIMO systems deployed in a crowded area. Authors in [102] have proposed a novel AP selection algorithm for CF mMIMO, which aims at reducing the computation workload and pilot contamination by introducing a machine-learning algorithm. A graph neural network-based access AP selection algorithm has also been proposed in [103], which has been shown to offer more accurately predicting of the potential APs compared to the proximity-based AP selection algorithms. Here, we explain a simple AP selection method called Largest-Large-Scale-Fading-Based (LLSFB) selection as proposed in [104].

In the LLSFB selection method, the kth user is associated with only L_k APs that are chosen based on

$$\sum_{l'=1}^{L_k} \hat{\beta}_{l'k} \geq \delta \sum_{l=1}^{L} \beta_{lk}, \tag{2.22}$$

where $\left\{\hat{\beta}_{1k}, ..., \hat{\beta}_{Lk}\right\}$ is the sorted (in descending order) set of large-scale fading coefficients from all APs for user k , and δ is the minimum proportion of the total received power from all APs that the chosen APs contribute to the desired signal at each user. First denoting $\mathcal{L}_k \subseteq \{1, ..., L\}$ as the subset of APs that serve user k, the block-diagonal binary $M \times M$ clustering matrix $\mathbf{D}_k$ for user k is then defined as

$$\mathbf{D}_k = \text{diag}(\mathbf{D}_{1k}, \ldots, \mathbf{D}_{Lk}), \tag{2.23}$$

where

$$\mathbf{D}_{lk} = \begin{cases} \mathbf{I}_N & \text{if } l \in \mathcal{L}_k, \\ \mathbf{0}_N & \text{if } l \notin \mathcal{L}_k. \end{cases} \tag{2.24}$$

In other words, the lth $N \times N$ diagonal block of $\mathbf{D}_k$ is $\mathbf{I}_N$ if AP l serves user k and $\mathbf{0}_N$ otherwise. By applying AP selection in CF mMIMO system for an unlimited number of users, the complexity of precoding and signaling at each AP would still be limited. Scalability makes implementing this method feasible in future networks.

By applying AP selection, the full channel matrices that are used to design precoding vectors are now replaced by effective channel matrices $\mathbf{D}_k\mathbf{G}_{\mathcal{S}_k} \in \mathbb{C}^{|\mathcal{S}_k| \times M}$. Two common partial precoding methods, that are categorized under distributed precoding are:

- **Partial zero-forcing (P-ZF):**

$$\mathbf{w}_k^{\text{P-ZF}} = \left[\mathbf{D}_k\mathbf{G}_{\mathcal{S}_k}^H(\mathbf{G}_{\mathcal{S}_k}\mathbf{D}_k\mathbf{G}_{\mathcal{S}_k}^H)^{-1}\right]_{:,1} \tag{2.25}$$

where $\mathcal{S}_k$ is the set of users served at least in part by the same APs as user k, including user k itself.

- **Partial regularized zero-forcing (P-RZF):**

While P-ZF forces the interference between served users to be zero, the UEs with similar channels will suffer from large losses in the desired signal power. To this end, another precoding technique called P-RZF is defined as

$$\mathbf{w}_k^{\text{P-ZF}} = \left[\mathbf{D}_k\mathbf{G}_{\mathcal{S}_k}^H(\mathbf{G}_{\mathcal{S}_k}\mathbf{D}_k\mathbf{G}_{\mathcal{S}_k}^H + \sigma^2\mathbf{P}_{\mathcal{S}_k}^{-1})^{-1}\right]_{:,1} \tag{2.26}$$

where $\mathbf{P}_{\mathcal{S}_k}$ is a diagonal matrix including the transmit power for $i \in \mathcal{S}_k$. P-RZF provides a trade-off between interference cancellation and boosting of the desired signal.

2.3 Symbiotic Backscatter Communication

Wirelessly powered BC [45] is a promising technology that integrates RF-based energy harvesting into wireless communications and can facilitate a practical realization of

sustainable IoT.

Although monostatic BC systems, bistatic BC systems, and AmBC have different configurations, they all share the same fundamentals. Specifically, none of them have their own RF source in the transmitter as conventional wireless systems do. However, a backscatter transmitter can send data to a backscatter receiver by tuning its antenna impedance to reflect the received RF signals. To do so, the backscatter transmitter must first be activated by harvesting the energy from the received RF signal. While Monostatic and bistatic backscatter systems use a dedicated RF source supplying the energy and backscattered signal, AmBC shares the same spectrum resource with the legacy users while harvesting. As a result, besides enhancing EE, significant improvement in spectrum utilization is also achievable. Due to providing high SE and EE, the thesis will focus on optimizing the performance of AmBC.

One of the main obstacles in implementing energy harvesting in wireless networks such as AmBC is the severe path loss between the transmitters and receivers [105]. Because of this, CF mMIMO may be considered to improve the energy transfer efficiency and mitigate the interference to unintended communication devices. Due to the high degree of macro-diversity, the reduced correlation of channels to different APs, reduced effects of shadowing, and the significantly lower average distance to the nearest AP, CF mMIMO has been shown to improve both SE and EE of the network [39, 100]. Specifically, the higher area density of APs in a CF mMIMO system makes it a good candidate to facilitate the implementation of energy-harvesting-based wireless networks.

The main complication in merging AmBC and CF mMIMO is that the numerous antennas and coherent beamforming in mMIMO typically lead to high directivity of signal power towards specific locations. Therefore, there is a significant chance that a BD transmitter would be at a location seeing low power levels from the APs, or possibly even having a beamforming null directed towards it. Furthermore, direct-link interference at the BD receiver from signals intended for legacy users will become even

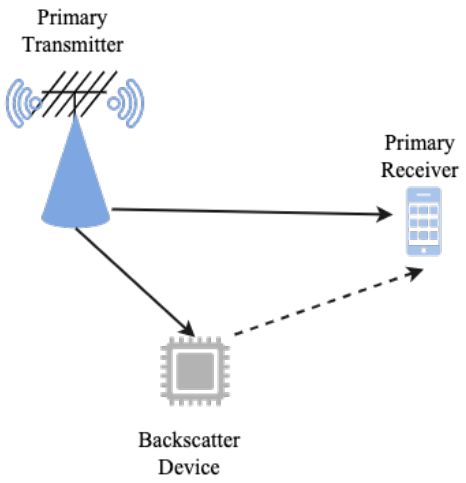

Figure 2.5: System model of symbiotic radio communication [62]

stronger than in conventional AmBC with a single-antenna RF source, limiting the AmBC transmission rate even further. One potential solution to these two challenges is SR, which has been proposed based on cooperative AmBC systems [61–63]. The BD still transmits its information in SR by reflecting ambient legacy signals. However, now the PT of the legacy system designs its transmit beamforming to assist both primary and BD transmissions. In contrast, the PR decodes information from the BD and the PT. The BD can help the primary transmission by providing additional multipath components to the channel. At the same time, the PT offers transmission opportunities to the BDs. Hence, SR is a promising solution to achieve spectrum-, power- and cost-efficient communications by sharing the spectrum, energy, and infrastructure of the primary system [63].

2.4 Summary

In this chapter, we have given an introduction to the topics of this thesis: mMIMO, CF mMIMO and BC. First, we have reviewed some of the main properties and challenges of mMIMO. Then, the necessary details on CF mMIMO including channel estimation, precoding design and scalability have been provided. At last, the main concepts on

backscatter communication have been discussed. We have also discussed some existing works related to our contributions to provide the necessary background to follow this thesis.

Chapter 3

Energy-Efficient Resource Allocation for the DL of Single-RF Chain Load-Modulated mMIMO HetNets

In this chapter, we focus on the design of a highly energy-efficient cellular HetNet by taking advantage of MIMO structure. First of all, we consider a MIMO-enabled H-CRAN, as a candidate architecture for 5G and beyond 5G systems [106]. In an H-CRAN, we need to consider two factors to achieve an acceptable and energy-efficient system performance. First, due to the potential capacity constraint of the fronthaul, to manage the interference CoMP should be limited to the BSs near a given user. Hence, we consider energy-efficient user-centric clustering and CoMP precoding performed at both the macro cell and SCs. Second, radio resources (i.e., RBs and power) should be optimally allocated to maximize EE. Therefore, a joint RB allocation and antenna selection algorithm is proposed and power allocation optimization is performed. To further reduce power consumption, in addition to antenna selection at the SCs, a load modulated single-RF-chain structure is also considered for the mMIMO macro BS. To our knowledge, the examination of a system combining all these factors simultaneously has not been well investigated in the literature. For example, [107–110] do not consider antenna selection, [110–115] consider single-carrier systems, while [113] and [114] consider only single-tier networks. A constrained-capacity fronthaul

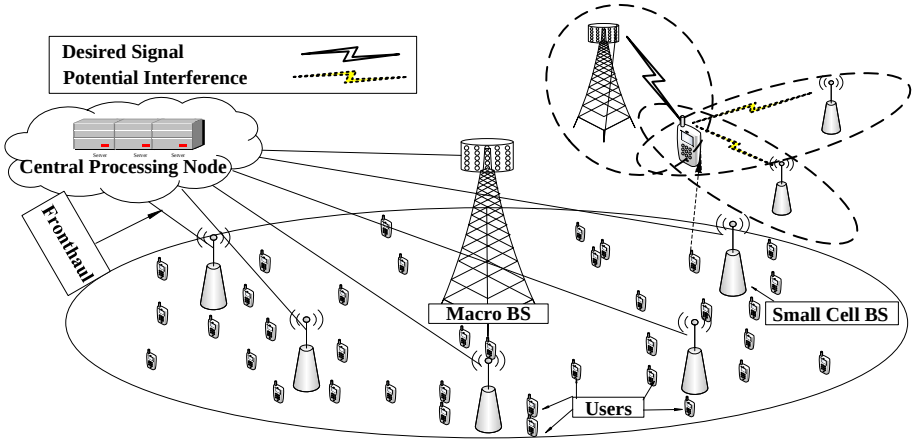

Figure 3.1: System layout of coordinated HetNet with clustered MIMO transceivers

have not been considered in the context of EEmax problems; none of the above papers considers it. (While [115] does ensure sufficient data rates are allocated to the backhaul for the SCs, it does not set an explicit maximum limit on those rates.)

3.1 System Model

We consider the DL of a HetNet where a macro cell containing a mMIMO enabled macro BS with N_M antennas is densely overlaid with S SC BSs each equipped with N_S antennas. The total number of single-antenna users served by all cells is N_U. For simplicity, we assign $s = 0$ to the macro BS; then, the set of all BSs can be denoted as $\mathcal{S} = \{0, ..., S\}$.

OFDMA is utilized in the network in order to convert frequency-selective MIMO channels into a series of RBs on parallel frequency-flat fading subchannels. Each subchannel is assumed to be quasi-static in time, meaning that the channel gains stay constant during each transmission, then change independently for the next transmission. The total bandwidth of the system is W and B RBs each with a bandwidth of $W_0 = W/B$ are available in each scheduling interval.

To address the interference problem of our dense HetNet, a structure similar to a CRAN is deployed, with a centralized processing structure that is inherently suited to

mitigate interference through the use of CoMP. Specifically, we consider coordinated beamforming, as it requires less overhead data transfer on the capacity-constrained fronthaul. In CoMP, a set of BSs that coordinate transmissions is often called a cluster. Clusters can be fixed or dynamically changing over time, but in both cases, they can potentially end up shifting the interference problem from the cell edge to the cluster edge (i.e., they cause users near the cluster edge to experience the worst interference). To avoid this, we form user-centric clusters; that is, the set of BSs that coordinate for each user is customized for that user. Only nearby SCs coordinate for any given user; it is unnecessary to cluster distant ones, since they cause little interference, and doing so would contribute needlessly to the overhead on the fronthaul. The macro BS may also be part of the cluster.

In problems like ours in which many parameters need to be optimized while satisfying several constraints, the non-convex joint optimization problem will become so complicated that the optimal solution can only be obtained by exhaustive search with an infeasibly large computational load [116]. Thus, we instead decompose the mixed-integer nonlinear programming problem into a series of subproblems [117].

3.2 Cell Association and User-Centric Clustering

In this work, we adopt a biased cell association policy along with user-centric clustering. Let the average received signal strength or channel quality (in dB) received from BS s by user n be denoted by $\gamma_{s,n}$. $\gamma_{s,n}$ is proportional to the maximum transmit power available at BS s, and accounts for path loss and shadowing, but not small-scale fading. We then define a bias Υ_s in dB in favor of BS s for load balancing purposes [118]. User n then associates with and is served by cell s_n^* for which

$$s_n^* = \arg\max_s \{\gamma_{s,n} + \Upsilon_s\} \tag{3.1}$$

For our user-centric clustering, each user will be served by one BS in its cluster, while the remaining BSs in the cluster perform coordinated beamforming for that user. We follow a similar approach as in [119] to select BSs for the cluster of each

user. The cluster is based on the difference of the average received signal strength. BSs whose signal strength is within ζ_c dB of the signal strength of the serving BS s_n^* for user n are selected for the cluster $\mathcal{S}_n$ for user n:

$$\mathcal{S}_n = \{l \in \mathcal{S} | \gamma_{s_n^*,n} - \gamma_{l,n} \leq \zeta_c\} \tag{3.2}$$

The value of the clustering threshold ζ_c should be chosen such that the interference from BSs that are not included in the cluster for user n is negligible. Let $\mathcal{K}_s$ (with cardinality K_s) denote the set of users that are associated with and receive information from BS s, and let $\mathcal{I}_s$ (with cardinality I_s) denote the users that are associated with other BSs, but that have BS s as a member of their cluster. From eq. (3.2) it is clear that in general cell-center users will have fewer BSs in their clusters than cell-edge users. There is some similarity between our work and [110], in which an "interference zone" around each SC is considered when forming clusters, to determine whether the BS should be in a given cluster. The difference is that the clusters in [110] are therefore BS-centric, whereas we perform user-centric clustering. Both the association bias and the clustering threshold can potentially also be used for load balancing, to offload users to lightly-loaded cells and/or avoid overloading in other cells. However, this aspect is outside the scope of this work.

3.3 Performance Metrics

The complex-valued baseband signal $y_{s,n,b}$ received by user n served by BS s in RB b is expressed as

$$\begin{aligned} y_{s,n,b} =& \sqrt{\Gamma_{s,n}}\mathbf{h}_{s,n,b}\mathbf{f}_{s,n,b}x_{s,n,b} + \sum_{i \in \mathcal{K}_s \setminus \{n\}} \sqrt{\Gamma_{s,n}}\mathbf{h}_{s,n,b}\mathbf{f}_{s,i,b}x_{s,i,b} \\ &+ \sum_{r \in \mathcal{S} \setminus \{s\}} \sum_{j \in \mathcal{K}_r} \sqrt{\Gamma_{r,n}}\mathbf{h}_{r,n,b}\mathbf{f}_{r,j,b}x_{r,j,b} + n_{s,n,b}, \end{aligned} \tag{3.3}$$

where $\mathbf{f}_{s,n,b} \in \mathbb{C}^{N_s \times 1}$ and $x_{s,n,b}$ are the complex-valued beamforming vector and data symbol from BS s to user n in RB b, respectively (cf. [8]). We also define $\mathbf{t}_{s,b} = \sum_n \mathbf{f}_{s,n,b}x_{s,n,b}$ as the transmitted signal vector from BS s on RB b. $\Gamma_{s,n}$ is the large-

scale signal power gain/attenuation between BS s and user n, which includes path loss and log-normal shadowing. $n_{s,n,b} \sim \mathcal{CN}(0, \sigma^2)$ is the additive white Gaussian noise (AWGN) at user n on RB b.

$\mathbf{h}_{s,n,b} \in \mathbb{C}^{1\times N_s}$ denotes the small-scale fading of the MIMO channel vector between user n and the BS s for RB b. $\mathbf{h}_{s,n,b}$ is modeled as $\sim \mathcal{CN}(0, \mathbf{R}_{s,n})$, which represents frequency-flat spatially-correlated Rayleigh fading on each subchannel, where $\mathbf{R}_{s,n}$ is the spatial correlation matrix between BS s and user n. The channel gains are independent between users and for each RB b, though we assume each RB has the same spatial correlation matrix for a given s and n. For SCs, the antennas are assumed to be located closer to the ground, so that SC channels experience a rich scattering environment. As such, there is assumed to be no spatial correlation between antennas, so $\mathbf{R}_{s,n} = \mathbf{I}_{N_s}$ for SCs. In contrast, the macro BS antennas are assumed to be higher up, such that scatterers are located only near the users (i.e., localized scattering). In this case, we model $\mathbf{R}_{0,n}$ by the equation given in [8, Eq. (2.24)].

In eq. (3.3), the summation in the second term is intra-cell interference between users served by BS s, whereas the double summation in the third term represents inter-cell interference from BSs other than the one sending data to user n. The goal of clustering is to reduce the magnitude of the third term as much as possible, ideally such that it becomes negligible.

The total sum data rate (in bits/s) is calculated as

$$C = \sum_{s=0}^{S} \sum_{n=1}^{N_U} \sum_{b=1}^{B} \delta_{s,n,b} W_0 \log_2(1 + \sigma_{s,n,b}), \tag{3.4}$$

$\delta_{s,n,b}$ is a binary user-BS association and RB assignment indicator, which is equal to 1 if user n receives data from BS s on RB b, and 0 otherwise. $\sigma_{s,n,b}$ is the SINR and $p_{s,n,b}$ is the power allocated to the nth user from the sth BS on the bth RB. We also denote N_0 as the spectral density of the AWGN. Then, the SINR is expressed as:

$$\sigma_{s,n,b} = \frac{\Gamma_{s,n} p_{s,n,b} |\mathbf{h}_{s,n,b} \mathbf{f}_{s,n,b}|^2}{W_0 N_0 + \sum\limits_{i \in \mathcal{K}_s \setminus \{n\}} \Gamma_{s,n} p_{s,i,b} |\mathbf{h}_{s,n,b} \mathbf{f}_{s,i,b}|^2 + \sum\limits_{r \in \mathcal{S}_n \setminus \{s\}} \sum\limits_{j \in \mathcal{K}_r} \Gamma_{r,n} p_{r,j,b} |\mathbf{h}_{r,n,b} \mathbf{f}_{r,j,b}|^2} \tag{3.5}$$

Since our goal is to maximize EE, it is necessary to define an accurate power model. The power consumed by each transmission node s includes (radiated) transmit power, dynamic circuit power, and static circuit power [120]:

$$P_s = \frac{1}{\eta_s} \sum_{n \in \mathcal{K}_s} \sum_{b=1}^{B} \delta_{s,n,b} p_{s,n,b} + N_s P_s^{dyn} + P_s^{sta} \tag{3.6}$$

η_s is the efficiency of the PA, P_s^{dyn} is dynamic circuit power, and P_s^{sta} is static circuit power. Dynamic power includes the power consumption of circuitry such as mixers, digital-to-analog converters, filters, etc. Static circuit power is a constant term that includes power consumption by other transceiver circuitry, e.g., baseband processing, etc.

To decrease the number of RF-chains, in this work we utilize the load-modulated transceiver structure. With a slight adjustment to the definition in eq. (3.6), the consumed power for DL transmission of the single-RF-chain mMIMO macro BS transmitter can be expressed as

$$P_0 = \frac{1}{\eta_0} \sum_{n \in \mathcal{K}_0} \sum_{b=1}^{B} p_{0,n,b} + N_M P_0^{dyn} + P_0^{sta} \tag{3.7}$$

It is worth mentioning that P_0^{dyn} is the average consumed non-radiated power per antenna that is dependent on N_M rather than a constant. By using [89, Fig. 8], a table can be derived to determine the dynamic consumed power of the macro BS. We assume any calculations required to adjust the load modulator impedance parameters are included in P_0^{sta}. We also note again that η_0 in eq. (3.7) will be better in general than η_s in eq. (3.6) due to the use of a Class F PA. Despite having only one RF chain, the load-modulated transceiver can support an arbitrary number of users or streams.[1] All digital processing, such as channel coding and precoding, is done at baseband.

Finally, the total EE for our proposed scenario can be written as

[1]Restrictions on the number of supported users/streams therefore come from the number of antennas and/or the precoding method, rather than the number of RF chains.

$$\varepsilon \triangleq \frac{C}{\sum_{s=0}^{S} P_s}, \tag{3.8}$$

where C is given in eq. (3.4) and P_s is given in eq. (3.6) and eq. (3.7) for the SC BSs and macro BS, respectively.

3.4 Resource Block Assignment and Antenna Selection for Small Cells

The optimal RB assignment and antenna selection approach is by exhaustive search, that to reduce the computational complexity, we propose a suboptimal low-complexity RB and antenna selection strategy. The main idea is to decouple the RB and antenna selection into a two-part selection approach. First, we investigate the transmit antenna selection strategy in our MIMO-OFDMA system. Since different antennas may be selected for different RBs, causing all antennas to be activated, the selection cannot be conducted in a per-subchannel manner. Moreover, if any given antenna is selected, it should be used for all RBs as it will result in higher rates with no additional dynamic circuit power consumption. Hence, transmit antenna selection should be performed for all RBs together. RB assignment can then be conducted for each user for the selected antenna set. First we define $\arg\operatorname{sort}_{\downarrow_j}\{X_j\}$ to return the sorted arguments/indices $\{j\}$ corresponding to when the values $\{X_j\}$ are sorted in descending order. Then, the antennas are sorted according to

$$\underset{j\in\{1,2,\ldots,N_S\}}{\arg\operatorname{sort}_{\downarrow}} \left\{||\mathbf{g}_{s,j}||_F^2\right\}, \tag{3.9}$$

where $\mathbf{g}_{s,j}$ is the jth column of a $K_sB \times N_s$ channel matrix, which represents the channel gain (including small-scale fading, shadowing, and path loss) of the jth transmit antenna for all users served by SC s across all RBs. A similar approach has been used in [113], in which acceptable performance has been shown at lower complexity in comparison to an exhaustive search.

After sorting the antennas in descending order using the F-norm-based method, the active transmit antenna set $\mathcal{N}_s^{sel}$ for cell s is selected from the first $N_s^{sel} = \lceil L_s \hat{B}/B \rceil$ antennas, where $\hat{B}$ is the maximum number of RBs that can be allocated to a user and L_s is the number of users Bs s supports (either to serve data or to mitigate interference for). The reasoning behind this value of N_s^{sel} is that N_s^{sel} is also the number of degrees of freedom for spatial multiplexing per RB. Thus, the maximum number of single-antenna users that can be supported per RB by linear precoding is N_s^{sel}, or at most $N_s^{sel} B$ users in total.

With the transmit antenna set selected for each SC, now RB allocation can be done jointly for all BSs in light of coordinated beamfoming — if user n is allocated an RB at its serving cell, user n must also be accounted for on that RB at the other BSs in cluster $\mathcal{S}_n$ for interference mitigation. Let the subset of users from $\mathcal{L}_s$ that are allocated to RB b (either to receive data from BS s or to mitigate interference for other cells) be denoted $\mathcal{L}_{s,b}$, with cardinality $L_{s,b}$. We can similarly define subsets of $\mathcal{K}_s$ and $\mathcal{I}_s$ as $\mathcal{K}_{s,b}$ and $\mathcal{I}_{s,b}$ respectively, with cardinality $K_{s,b}$ and $I_{s,b}$. Similar to the antenna selection, we use an F-norm-based approach. First, we sort the BS-user-RB index triplets according to

$$\underset{(s,n,b),\ \forall s\in\mathcal{S},\ \forall n\in\mathcal{K}_s,\ \forall b\in\{1,\ldots,B\}}{\arg\operatorname{sort}_{\downarrow}} \left\{ \frac{\left|\left|\tilde{\mathbf{h}}_{s,n,b}\right|\right|_F^2}{N_s^{sel}} \right\}, \tag{3.10}$$

where $\tilde{\mathbf{h}}_{s,n,b} \in \mathbb{C}^{1\times N_s^{sel}}$ is the small-scale fading channel vector to user n on RB b from the selected set of antennas at its serving BS s. In the case of the macro BS, which does not perform antenna selection, $\tilde{\mathbf{h}}_{0,n,b} = \mathbf{h}_{0,n,b}$ and $N_s^{sel} = N_M$. We emphasize that the channel vector in eq. (3.10) includes only the small-scale fading component of the channel gains, i.e., the path loss and shadowing are normalized out. This is to provide fairness[2] to all users in an effort to meet the minimum data rate constraints, so that users near BSs are not allocated a disproportionately large number of RBs to

[2]This has similarities to proportionally fair user scheduling [121],[122], in that both give highest priority to users who have the best channel relative to their average channel.

the detriment of cell-edge users. Each RB potentially can be selected to serve data to any user, as long as the total number of users $L_{s,b}$ sharing any given RB b at any SC s is at most $\hat{U}_s^{alc} = N_s^{sel}$, and the number of RBs $N_{RB,n}$ allocated to user n is at most $\hat{B}$. For the macro BS, however, we pose an additional constraint. Due to the abundance of transmit antennas for mMIMO, with $N_M \gg K_0$, there is essentially no limit to the number of users that can be served on any one RB. However, allocating too many users to one RB could put pressure on the resources for interference mitigation at the SCs on that RB. Hence, at the macro BS, we shall attempt to divide users among the RBs as evenly as possible, with no more than $\hat{U}_0^{srv} = \lceil (K_0 \hat{B}/B) \rceil$ users served on any given RB. After antenna selection, RBs are allocated in the order given by eq. (3.10), but first ensuring that each user is given at least one RB from its serving BS in phase 1. Then, if $\hat{B} > 1$ and sufficient resources remain, additional RBs will be allocated to the users in phase 2, in the order given by eq. (3.10).

Occasionally, the algorithm may run into corner cases when assigning users to RBs. Users with large clusters require the resource allocation at numerous BSs to be sufficiently coordinated in order to avoid turning on antennas at SC BSs. Specifically, an allocation spot must be available at all BSs in the cluster on the same RB. In other words, each user must be a member of $\mathcal{L}_{s,b}$ for some same value of b for all BSs s in its cluster. If these large-cluster users end up being allocated RBs near the end of the process, there may be insufficient remaining resources at all BSs in the user's cluster on any one RB to allow for coordination in the cluster. To deal with such corner cases if they occur, we restart the allocation process with these users at the start of the allocation order. The remaining users are ordered as normal afterwards; since they require fewer resources to be coordinated, they are easier to slot into the remaining positions.

Obviously, there is a trade-off between the achievable sum rate and power usage. As we have discussed, switching off antennas will affect the spatial degrees of freedom in the users' channels (and thus the degrees available to the precoder), as well as the

maximum number of users that can be served simultaneously per RB, which will lead to a reduction in the achievable sum rate of the system. However, activating fewer antennas will lead to less power consumption, which is beneficial in terms of EE.

3.5 Precoding Vector Design

The design of the precoding scheme used for transmission in a MU-MIMO system is an important factor in the resulting EE of the system. The objective of precoding in general is to mitigate intra-cell interference between users of that cell. When coordinated beamforming is used, it can also mitigate intra-tier and inter-tier interference between BSs of a cluster. To begin, we look at mitigating the interference caused by SCs. For lower computational complexity, we use linear precoding. Specifically, we consider the same type of null-space projection precoding as is used in BD precoding [123]. The same null-space projection technique has also been used in [110, 124] in the context of single-antenna users, as it is with our work herein.[3] We have chosen null-space projection since it has been shown (e.g., in [110]) that, while null-space projection and the channel inversion technique used in "classical" ZF precoding perform identically when maximizing the sum rate of a MU-MIMO HetNet, when considering EE instead, using channel inversion for SCs results in smaller EE in various cases.

The precoding is performed on a per-RB basis. With null-space projection precoding, the transmit precoding vector of each user is designed to lie in the null space of the channels of all $L_{s,b} - 1$ other users in $\mathcal{L}_{s,b}$. This means the precoding vectors must satisfy [123]:

$$\tilde{\mathbf{h}}_{s,n,b}\mathbf{f}_{s,i,b} = 0, \forall (n,i) \in \mathcal{L}_{s,b} \text{ such that } n \neq i, \forall (b,s) \tag{3.11}$$

[3] As mentioned, BD has been defined for multiple-antenna users. The technique is still valid for single-antenna users, although in such a case, it is not particularly "block" diagonalization anymore, as the "block" ends up being a scalar (i.e., of size 1×1). For the single-antenna case, we shall therefore refer to it as null-space projection, to differentiate the technique from "classical" ZF precoding, which instead uses channel inversion.

Let $\tilde{\mathbf{H}}_{s,n,b} \in \mathbb{C}^{(L_{s,b}-1)\times N_s^{sel}}$ be a matrix that vertically concatenates the channel vectors for RB b of all users in $\mathcal{L}_{s,b}$ except for user n:

$$\tilde{\mathbf{H}}_{s,n,b} = \left[\tilde{\mathbf{h}}_{s,1,b}^T \dots \tilde{\mathbf{h}}_{s,n-1,b}^T \;\; \tilde{\mathbf{h}}_{s,n+1,b}^T \dots \tilde{\mathbf{h}}_{s,L_{s,b},b}^T\right]^T \tag{3.12}$$

We denote $\tilde{r}_{s,n,b}$ as the rank of that aggregate null space and $\tilde{\mathbf{V}}_{s,n,b}^0 \in \mathbb{C}^{N_s^{sel}\times(N_s^{sel}-\tilde{r}_{s,n,b})}$ as a set of orthonormal basis vectors for that null space [123] (and thus the basis for $\mathbf{f}_{s,n,b}$). The equivalent channel $\ddot{\mathbf{h}}_{s,n,b} \in \mathbb{C}^{1\times(N_s^{sel}-\tilde{r}_{s,n,b})}$ for user n is $\ddot{\mathbf{h}}_{s,n,b} = \tilde{\mathbf{h}}_{s,n,b}\tilde{\mathbf{V}}_{s,n,b}^0$, with $\lambda_{s,n,b} = ||\ddot{\mathbf{h}}_{s,n,b}||$ being its channel gain. Hence, the signal received by user n from SC s on RB b can be expressed as

$$y_{s,n,b} = \sqrt{\Gamma_{s,n}p_{s,n,b}}\lambda_{s,n,b}x_{s,n,b} + n_{s,n,b} \tag{3.13}$$

To summarize, through the use of null-space projection precoding, the precoding vectors are designed such that intra-cell and intra-cluster interference is completely canceled, and the MU-MIMO channels are decomposed into several equivalent non-interfering single-user MIMO channels. Under the assumption of no significant interference after precoding, the SINR in eq. (3.5) reduces to

$$\sigma_{s,n,b} = \frac{\Gamma_{s,n}\lambda_{s,n,b}^2}{W_0N_0}p_{s,n,b} = \chi_{s,n,b}p_{s,n,b}, \tag{3.14}$$

where we define $\chi_{s,n,b}$ as the ratio of the equivalent subchannel power gain to its noise power.

At the macro BS, "classical" ZF precoding is performed to mitigate interference both between macro users and to users of SCs; the precoding is again done per RB. The relatively simpler precoding (compared to null-space projection) is sufficient for the mMIMO BS, since the law of large numbers makes channel vectors to different users near-orthogonal even without precoding [8]. First, we define $\breve{\mathbf{H}}_{0,b} \in C^{L_{0,b}\times N_M}$ as the channel matrix that vertically concatenates the small-scale fading portion of the channel vectors for the users in $\mathcal{K}_{0,b}$, followed by the users in $\mathcal{I}_{0,b}$:

$$\breve{\mathbf{H}}_{0,b} = \left[\mathbf{h}_{0,\mathcal{K}_{0,b}(1),b}^T \; \mathbf{h}_{0,\mathcal{K}_{0,b}(2),b}^T \dots \quad \mathbf{h}_{0,\mathcal{K}_{0,b}(K_{0,b}),b}^T \;\; \mathbf{h}_{0,\mathcal{I}_{0,b}(1),b}^T \dots \mathbf{h}_{0,\mathcal{I}_{0,b}(I_{0,b}),b}^T\right]^T \tag{3.15}$$

Then the ZF precoding vector can be found from [110]

$$\breve{\mathbf{F}}_{0,b} = \breve{\mathbf{H}}_{0,b}^{\dagger} = \breve{\mathbf{H}}_{0,b}^{H}(\breve{\mathbf{H}}_{0,b}\breve{\mathbf{H}}_{0,b}^{H})^{-1} \tag{3.16}$$

Consider the first $K_{0,b}$ columns of $\breve{\mathbf{F}}_{0,b}$, and let the nth column of $\breve{\mathbf{F}}_{0,b}$ be denoted $\breve{\mathbf{f}}_{0,n,b}$. The precoding vector $\mathbf{f}_{0,n,b}$ for user $\mathcal{K}_{0,b}(n)$ (i.e., the nth user served by the macro BS on RB b) is

$$\mathbf{f}_{0,n,b} = \frac{\breve{\mathbf{f}}_{0,n,b}}{||\breve{\mathbf{f}}_{0,n,b}||} \tag{3.17}$$

In this way, the interference from the macro BS has been mitigated. Assuming as we did for the SCs that all remaining interference is negligible, then the SINR for macro users reduces to

$$\sigma_{0,n,b} = \frac{\Gamma_{0,n}|\mathbf{h}_{0,n,b}\mathbf{f}_{0,n,b}|^2}{W_0 N_0} p_{0,n,b} = \chi_{0,n,b} p_{0,n,b} \tag{3.18}$$

3.6 Power Allocation

For compactness of notation, let $\mathbf{p}$ be a vector containing all the power allocation variables $\{p_{s,n,b}\}, \forall s, n, b$. Then, the EEmax problem under minimum-rate constraints, maximum fronthaul capacity limitations, and total transmit power constraints is formulated as

$$\max_{\mathbf{p}} \quad \frac{W_0 \sum_{s=0}^{S}\sum_{n=1}^{N_U}\sum_{b=1}^{B} \delta_{s,n,b}\log_2(1+\chi_{s,n,b}p_{s,n,b})}{\sum_{s=0}^{S}\sum_{n=1}^{N_U}\sum_{b=1}^{B}\frac{1}{\eta_s}\delta_{s,n,b}p_{s,n,b} + \sum_{s=0}^{S} N_s^{sel}P_s^{dyn} + \sum_{s=0}^{S} P_s^{sta}} \tag{3.19a}$$

$$\text{s.t.} \quad \sum_{b=1}^{B} c_{s,n,b} \geq \kappa_{min}, \quad \forall s \in \mathcal{S}, \forall n \in \mathcal{K}_s \tag{3.19b}$$

$$\sum_{n=1}^{N_U}\sum_{b=1}^{B} \delta_{s,n,b} c_{s,n,b} \leq c_{s,limit}, \quad \forall s \in \mathcal{S} \tag{3.19c}$$

$$\sum_{n=1}^{N_U}\sum_{b=1}^{B} \delta_{s,n,b} p_{s,n,b} \leq P_s^{\max}, \quad \forall s \in \mathcal{S} \tag{3.19d}$$

$$p_{s,n,b} \geq 0 \qquad \forall s, n, b \tag{3.19e}$$

where $c_{s,n,b} = W_0\log_2(1+\sigma_{s,n,b})$. P_s^{max} is the maximum transmit power of BS s. κ_{min} is the minimum data rate guaranteed for users and $c_{s,limit}$ is the maximum data rate

that can be transferred over the fronthaul links. Like in eq. (3.10), $N_s^{sel} = N_M$ for the macro BS. The constraints given by eq. (3.19b) characterize the minimum rate guaranteed for each user and the constraints given by eq. (3.19d) and eq. (3.19e) represent the maximum transmit power available at each BS. As one of the performance limiting factors of the network, limited fronthaul capacity has been included in our problem as the constraints given by eq. (3.19c).

Since the optimization problem defined in eq. (3.19) is classified as nonlinear fractional programming, which results in a nonconvex problem, there is no one standard method for solving it. Our first step is to simplify the objective function using techniques from nonlinear fractional programming. Following [125], we can formulate an equivalent problem as follows:

$$\max_{\mathbf{p}} \ \{C(\mathbf{p}) - \varepsilon^* P(\mathbf{p})\} = C(\mathbf{p}^*) - \varepsilon^* P(\mathbf{p}^*) = 0 \tag{3.20}$$

where ε^* is the maximum EE of the overall network, $\mathbf{p}^*$ is the optimal power allocation vector, and $\mathbf{p}$ is any feasible solution of the problem in eq. (3.19) that satisfies the constraints given by eq. (3.19b)-eq. (3.19e).

It has been proven in [119] that for any optimization problem with an objective function in fractional form, there is an equivalent optimization problem with an objective function in subtractive form that leads to the same solution. Hence, we can concentrate on the equivalent problem in the rest of this chapter. The equivalent problem can be formulated as

$$\begin{aligned} &\max_{\mathbf{p}} \ \{C(\mathbf{p}) - \varepsilon P(\mathbf{p})\} \\ &\text{s.t.} \quad \text{eq. (3.19b)–eq. (3.19e)} \end{aligned} \tag{3.21}$$

Now we must find the optimal value of ε. Since ε^* cannot be obtained directly, an iterative algorithm (based on what is known as the Dinkelbach method [125], which is commonly used for EEmax problems [126]) is proposed, in which the obtained solution ensures eq. (3.20) is satisfied. Pseudocode for the proposed algorithm is described in algorithm 1.

Algorithm 1 Dinkelbach method for EE maximization

1: Initialize the convergence threshold λ_{th};
2: Set $i = 1$ and $\varepsilon^{(1)} = 0$;
3: For initial $\varepsilon^{(1)}$, obtain $C(\mathbf{p}^{(1)})$ and $P(\mathbf{p}^{(1)})$ by solving the problem in eq. (3.21) using eq. (3.23) and eq. (3.24);
4: **while** $[C(\mathbf{p}^{(i)}) - \varepsilon^{(i)} P(\mathbf{p}^{(i)}) < \lambda_{th}]$ **do**
5: $\quad i = i + 1$;
6: $\quad$ (Inner Loop): Solve the resource allocation problem in eq. (3.21) using eq. (3.23) and eq. (3.24) with $\varepsilon^{(i-1)}$ to obtain the optimal solution $\mathbf{p}^{*(i)}$;
7: $\quad \varepsilon^{(i)} = \frac{C(\mathbf{p}^{*(i)})}{P(\mathbf{p}^{*(i)})}$;
8: **end while**
9: Output: $\mathbf{p}^*, \varepsilon^*$, C, P.

The algorithm consists of an outer loop, which updates the value of ε, and an inner loop, which updates $C(\mathbf{p})$ and $P(\mathbf{p})$. Convergence to the optimal solution is guaranteed if one is able to solve the inner problem. As $\varepsilon^{(i+1)}$ is updated in each iteration i in the outer loop with $C(\mathbf{p}^{(i)})$ and $P(\mathbf{p}^{(i)})$ obtained in the last iteration, the value of ε converges towards its maximum. Meanwhile, by solving the inner loop for a given $\varepsilon^{(i)}$, the optimal power policy needed for the next loop would be obtained, with the whole algorithm iterating until all the values converge or some other stopping criterion (e.g., a maximum number of iterations) is reached.

The transformed problem can be expressed as in eq. (3.21), with ε replaced now by $\varepsilon^{(i)}$. The problem is now concave with respect to optimization variable $\mathbf{p}$. We derive the Lagrangian function [127] of the problem as follows:

$$
\begin{aligned}
L(\mathbf{p}, \boldsymbol{\alpha}, \boldsymbol{\beta}, \boldsymbol{\mu}) = & \sum_{s=0}^{S} \sum_{n=1}^{N_U} \sum_{b=1}^{B} \delta_{s,n,b} c_{s,n,b} - \varepsilon^{(i)} \left(\sum_{s=0}^{S} \sum_{n=1}^{N_U} \sum_{b=1}^{B} \frac{1}{\eta_s} \delta_{s,n,b} p_{s,n,b} \sum_{s=0}^{S} N_s^{sel} P_s^{dyn} + \sum_{s=0}^{S} P_s^{sta} \right) \\
& + \sum_{s=0}^{S} \sum_{n \in \mathcal{K}_s} \alpha_{s,n} \left(\sum_{b=1}^{B} c_{s,n,b} - \kappa_{min} \right) + \sum_{s=0}^{S} \beta_s \left(c_{s,limit} - \sum_{n=1}^{N_U} \sum_{b=1}^{B} W_0 \delta_{s,n,b} \log_2(1 + \chi_{s,n,b} p_{s,n,b}) \right) \\
& + \sum_{s=0}^{S} \mu_s \left(P_s^{\max} - \sum_{n=1}^{N_U} \sum_{b=1}^{B} \delta_{s,n,b} p_{s,n,b} \right)
\end{aligned}
\tag{3.22}
$$

The vector $\boldsymbol{\mu}$ contains the Lagrangian multipliers μ_s corresponding to the maximum

transmit power limit for BS s in eq. (3.19d). $\boldsymbol{\alpha}$ contains the Lagrangian multipliers $\alpha_{s,n}$ associated with the minimum rate constraints in eq. (3.19b). Finally, $\boldsymbol{\beta}$ contains the Lagrangian multipliers β_s accounting for the fronthaul capacity constraint for BS s in eq. (3.19c).

For fixed $\boldsymbol{\alpha}$, $\boldsymbol{\beta}$, $\boldsymbol{\mu}$, and ε, the problem can be solved utilizing the Karush-Kuhn-Tucker (KKT) conditions [127, 128]. The optimal value of $p_{s,n,b}$ is then obtained by making the partial derivatives of L with respect to $p_{s,n,b}$ equal to zero, which yields a "water-filling" type of solution. We derive the optimal power as:

$$p^*_{s,n,b} = \max\left(w^*_{s,n} - \frac{1}{\chi_{s,n,b}}, 0\right), \tag{3.23}$$

where

$$w^*_{s,n} = \frac{W_0(1 + \alpha_{s,n} - \beta_s)}{\ln 2\,(\mu_s + \varepsilon^{(i)}/\eta_s)}, \tag{3.24}$$

and $\chi_{s,n,b}$ is given in eq. (3.14) and eq. (3.18). The values of $p^*_{s,n,b}$ are used to update the value of $\varepsilon^{(i)}$. Then, the subgradient method can be used for updating the values of the Lagrange multipliers in the outer loop; this method is guaranteed to converge to the optimal Lagrange multipliers, as long as the step size values are chosen to be sufficiently small [129].

3.7 Analytical Results

In this subsection, we analytically approximate the gains in EE that are possible by some of the methods used in our system. Due to all the various methods combined in the system, it is unfortunately infeasible to analytically characterize the system as a whole. We therefore focus on the effect of antenna selection at the SCs on the EE. In this case, we assume that the macro BS is either part of the cluster for the SC users so that it provides no interference to those users, or its interference power is below the clustering threshold, and so its interference may be neglected when considered in aggregate with the other interfering SC BSs.

For the analysis, we will draw on the some of the results using stochastic geometry modeling of cellular networks (e.g., [130–133]). For simplicity and tractability, we assume that the SC BS layout can be modeled by a homogeneous Poisson point process (PPP) Φ_s having intensity λ_s, wherein the BS locations are distributed uniformly over the plane. The users are located according to an independent homogeneous PPP Φ_u with intensity λ_u. We further assume a) that every served user at every BS is assigned the same power p, with $K_s p \leq P_s^{\max}$, b) that supported users are distributed approximately evenly across the RBs, so $K_{s,b}$, $I_{s,b}$, and $L_{s,b}$ are the same for every cell and RB, and c) that the system is interference-limited, so that the noise power is negligible. This provides a lower bound on the performance; naturally, the performance would be better by optimizing the power allocation and by better assigning users to RBs. The inclusion of log-normal shadowing with zero mean and standard deviation σ_{shadow} has the effect of scaling the intensity λ_s by a factor of $\exp(2(\frac{\sigma_{shadow}\ln(10)}{10\alpha_s})^2)$ [131], where α_s is the path loss exponent.

Under the above conditions, the SINR for one user n served on a given RB b by BS s from (3.5), when null-space projection precoding is used at the BSs, can be expressed as:

$$\begin{aligned}\sigma_{s,n,b} &= \frac{\Gamma_{s,n} p |\mathbf{h}_{s,n,b}\mathbf{f}_{s,n,b}|^2}{\sum_{r\in\mathcal{S}_n\setminus\{s\}}\sum_{j\in\mathcal{K}_r}\Gamma_{r,n} p |\mathbf{h}_{r,n,b}\mathbf{f}_{r,j,b}|^2} \\ &= \frac{d_{s,n}^{-\alpha_s} g_{s,n}}{\sum_{r\in\Phi_s\setminus\{s\}} d_{r,n}^{-\alpha_s} g_{r,n}},\end{aligned} \tag{3.25}$$

where $d_{s,n}$ ($d_{r,n}$) denotes the distance between BS s (r) and user n, α_s is the path loss exponent, and $g_{s,n} = |\mathbf{h}_{s,n,b}\mathbf{f}_{s,n,b}|^2$ and $g_{r,n} = \sum_{j\in\mathcal{K}_r} |\mathbf{h}_{r,n,b}\mathbf{f}_{r,j,b}|^2$ represent the precoded channel power gain for user n from the serving BS s and an interfering BS r, respectively. As seen, the specific value of p cancels out.

It is known that if a BS has N_s^{sel} active antennas, the elements of $\mathbf{h}_{s,n,b}$ are independent and distributed $\sim \mathcal{CN}(0,1)$ (i.e., Rayleigh fading), and the precoding vector $\mathbf{f}_{s,n,b}$ for user n is orthogonal to the channels of $L_{s,b}-1$ users supported on RB b at BS s

(such as with ZF or null-space projection precoding), then the precoded channel power gain is a Gamma-distributed random variable such that $g_{s,n} \sim \Gamma(N_s^{sel} - L_{s,b} + 1, 1)$ [132, 134]. Meanwhile, the precoding at other BSs that are not part of the cluster for user n is independent of the interfering channel to user n. As such, a single beam from the interfering BS r has a power gain distributed $\sim \Gamma(1, 1)$, and the sum of K_r beams from BS r, i.e., $g_{r,n}$, has a power gain distributed $\sim \Gamma(K_r, 1)$ [134].

Given the PPP model and the association scheme described by (3.1), it is straightforward to see that if a user associates with the SC tier, it will associate with the closest SC BS. Furthermore, from the clustering scheme described by (3.2), if a BS is part of a cluster for user n, its received reference signal strength will be within ζ_c dB of the received reference signal strength from the serving BS s, or numerically, $P_r^{ref} \geq 10^{-\zeta_c/10} P_s^{ref}$. As previously stated, the reference signal strength is assumed to be proportional to the maximum signal power available at the BS, which is the same for all SC BSs. Moreover, the path loss for BS r is given by $d_{r,n}^{-\alpha_s}$. Hence, if BS r is part of the cluster for user n, then $P_s^{\max} d_{r,n}^{-\alpha_s} \geq 10^{-\zeta_c/10} P_s^{\max} d_{s,n}^{-\alpha_s}$. Rearranging, we find that the cluster for a given user will consist of all BSs where

$$d_{r,n} \leq \Delta d_{s,n}, \text{ where } \Delta = 10^{\zeta_c/(10\alpha_s)} \tag{3.26}$$

Lemma 1: In the PPP model, the mean number of users supported by a BS (either served or part of their cluster) is

$$\mathbb{E}[L_s] = \Delta^2 \lambda_u / \lambda_s \tag{3.27}$$

Proof: See Appendix A.

The achievable rate of a user is given by $W_0 \log_2(1 + \sigma_{s,n,b})$. Since the signals precoded at a given BS do not interfere between the users served by that BS (due to null-space projection precoding), nor do the signals interfere between RBs, the sum rate of SC s is simply $\sum_{n,b} W_0 \log_2(1 + \sigma_{s,n,b})$. The mean SE of a user, i.e., $\mathbb{E}_{\sigma_{s,n,b}}[\log(1 + \sigma_{s,n,b})]$, can theoretically be found following the methodology found in

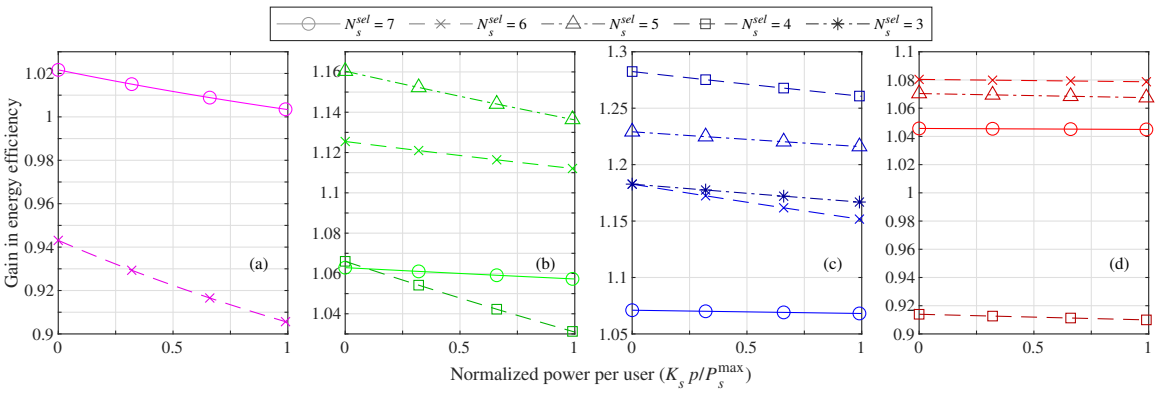

Figure 3.2: Gain in energy efficiency by antenna selection, relative to when all antennas are active, vs. normalized power allocated per user ($K_s p/P_s^{\max}$), with $N_s = 8$. (a) $K_s = 13, L_s = 300$. (b) $K_{s,b} = 1, L_{s,b} = 4$. (c) $K_{s,b} = 2, L_{s,b} = 3$. (d) $K_{s,b} = L_{s,b} = 4$.

[131] for fading that follows a κ-μ distribution. (A Gamma distribution $\Gamma(k, \theta)$ with shape parameter k and scale parameter θ is a special case of the κ-μ distribution in [131], where $\kappa = 0$, $m = \mu = k$, and $\theta_1 = \theta_2 = \theta$.) Unfortunately, we have found that for our proposed system, the final integral for $\mathbb{E}_z[\log(1 + z)]$ is non-convergent. Therefore, we will rely instead on a simulation of the PPP model.

For the PPP simulation, we simulate 200000 realizations of a PPP, within a square region containing on average 10000 points. In each realization, the distance of the points to the origin (center of the square) is measured. The closest point to the origin is set as the serving BS. Each point is assigned a Gamma-distributed value representing the precoded channel power gain for that BS. We consider a few different scenarios in terms of served and clustered user loads. Other relevant parameters are the same as in Table 3.1.

In Fig. 3.2, we examine the gain in EE that is possible due to antenna selection. The gain is the EE achieved when the specified number N_s^{sel} of SC antennas are activated per cell, relative to when all $N_s = 8$ antennas are active. As seen, significant gains are possible; Fig. 3.2(c) in particular displays gains of over 25%. As expected, the gain is the highest when the amount of power allocated to each user is the lowest. In this situation, changing the dynamic potion of the consumed power has the relatively largest effect on the overall reduction in the value of P_s, and thus the gain in

EE. We also note that there is in general an optimal number of antennas to activate to maximize the EE gain. If too few antennas are active, the loss of available spatial multiplexing gain can cause the drop in SE to become larger relative to the drop in consumed power. In some cases, the system can even see a loss in EE compared to when all antennas are active, as observed in Figs. 3.2(a) and 3.2(d). However, one cannot draw a specific conclusion on the exact optimal number of antennas to activate from these results. To start, the allocation of users to RBs also has a significant effect on how many antennas it is possible to turn off. Thus, the specific allocation of RBs to users would also impact the optimal number of active antennas. The relationship between the two factors is far from straightforward. Furthermore, these results are for the equivalent of activating N_s^{sel} antennas at random, whereas our scheme selects the best N_s^{sel} antennas out of N_s to activate.

3.8 Simulation Results

In this section, we evaluate the performance of the proposed algorithm through simulations. The default parameters are given in table 3.1 unless otherwise stated. Most of the parameters are based on the recommendations in [135]. The total number of users N_U is 200, from which $\lfloor \frac{2N_U}{3S} \rfloor$ are uniformly distributed over the area of each SC, while the remainder are uniformly distributed over the entire area of the macro cell. The path loss from the macro BS to a user is given by $128.1 + 37.6 \log_{10}(d)$ dB, and the path loss from the SC BSs to a user is determined by $140.7 + 36.7 \log_{10}(d)$ dB (with distance d in km) [135, Table A.2.1.1.2-3].

We show the impact of ζ_c on the EE and SE (normalized to the total system bandwidth) of our proposed scheme in Fig. 3.3. We also modify the scheme proposed in [136] and compare its resulting EE and SE with those of our user association method. Fig. 3.3 shows both the estimated EE and SE (calculated by the optimization algorithm assuming no interference) and the actual EE and SE (results from the true SINR in eq. (3.5), accounting for the residual interference) for our proposed method.

Table 3.1: Simulation Parameters

Parameter	Value	Parameter	Value
Number of small cells	10	Cell radius	40 m // 289 m
Position of SC BSs	On circle 249 m from macro BS, equally spaced in angle	Maximum transmit power	30 dBm // 46 dBm
Static power	0.1 W // 10 W	Dynamic power	0.1 W
PA efficiency	0.5 // 0.8	Fronthaul capacity	150 Mbits/s // 300 Mbits/s
Number of RBs	50	Maximum RBs allocated per user	1
Total bandwidth	10 MHz	Bandwidth per RB	200 KHz
Carrier frequency	2 GHz	Minimum QoS	128 kbits/s
Exclusion radius	10 m // 35 m	Shadowing std. dev.	10 dB
Noise power spectral density	-174 dBm/Hz	Number of antennas	8 // 100
Antenna spacing (multiple of wavelengths)	$\frac{1}{2}$	Macro BS spatial correlation ASD	$\frac{\pi}{18}$ radians (10°)
Macro BS distortion	10^{-6}	Total number of users	Variable, default 200
Association bias	3 dB // 0 dB (defaults)	Clustering threshold	Determined by simulation (see Fig. 5)
Optimization loop iterations	8 // 20	Monte Carlo	500 user drops // 1000 channel realizations

For the sake of brevity and legibility, only the actual EE and SE are depicted for the modified method from [136]. From the figure it is clear that by increasing ζ_c, the difference between the estimated and the actual curves decreases, since more BSs are included in each cluster and more interference is mitigated. For ζ_c greater than 25 dB, the actual EE decreases, meaning including more BSs per cluster degrades the EE. This is due to more antennas needing to be activated at the SC BSs to support BS coordination for the larger clusters. Thus, even though the estimated EE and SE become closer to the actual values for higher ζ_c, increasing ζ_c further has a detrimental

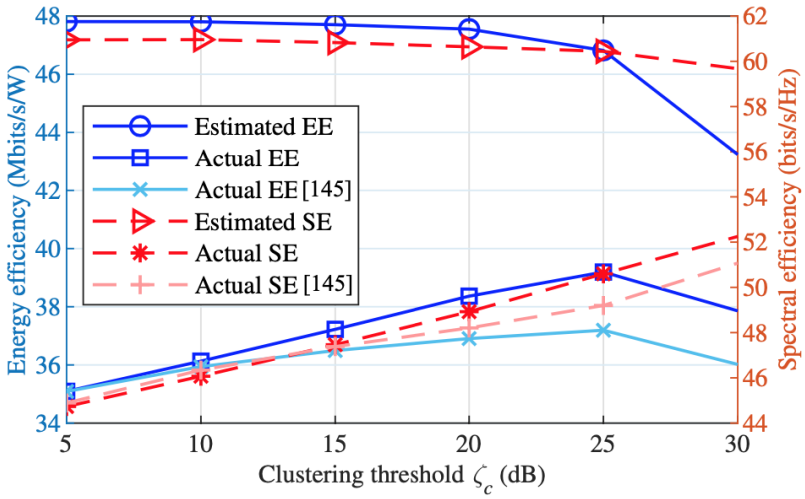

Figure 3.3: EE and SE (estimated and actual) of our proposed method vs. clustering threshold ζ_c, with $\Upsilon_s = 3$ dB.

effect on the actual performance. Hence, we use $\zeta_c = 25$ dB for the remainder of the chapter. As can be seen, our proposed method outperforms the method modified from [136] for both EE and SE. As our proposed method performs better while having less computational complexity, it is a better solution for user association. Finally, please note that the EE and SE values reported hereafter are the actual values.

Fig. 3.4 shows the comparison of the EE performance for the total HetNet, and for the macro and SC tiers separately, when the association bias Υ_s for the SCs changes. Υ_0, the association bias for the macro BS, stays constant at 0 dB, so increasing Υ_s means more emphasis is given to SCs and more users are served by SCs. As expected, by increasing Υ_s up to 3 dB, the EE of the SCs increases. The cause stems from the higher priority given to SCs that results in more users being served by them, while activating a minimal necessary number of antennas. However, with further increases to Υ_s, even more users are served by SCs, such that more antennas need to be activated. This leads to EE degradation. On the other hand, since larger Υ_s means fewer users are served by the macro BS, the macro cell EE decreases. Interestingly, changing Υ_s from -3 dB to +9 dB yields little change in the total EE; the EE changes by only about $\pm 2\%$ from its mean value of 38.3 Mbits/s/W over that range. This is due to the trade-off between the need to activate more antennas at the

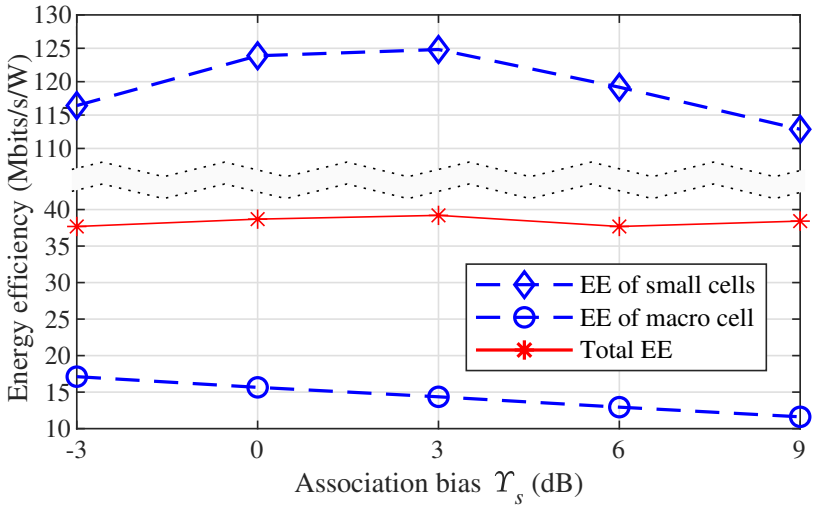

Figure 3.4: Total EE of HetNet and EE of macro and small cell HetNet tiers vs. association bias Υ_s for small cells for $\zeta_c = 25$ dB.

SCs, which leads to higher dynamic power consumption, versus serving users with lower total radiated transmit power, since in general the users will be closer to the SC BSs. Although serving more users by the macro BS seems more energy-efficient for the macro cell, using an association bias in favor of the SCs leads to transferring the traffic load to the comparatively lightly-loaded SCs. Offloading users to the SCs leaves more resources available for macro users, which is desirable for a scenario with higher mobility users, who would prefer to be served by the macro BS.

The convergence of the EE of our proposed scheme is illustrated in Fig. 3.5. Since there is no comparable scheme in the literature that combines all our considered factors and constraints, to evaluate the EE performance of our proposed scheme, an equal power allocation algorithm and a sequential RB assignment scheme are chosen as baseline algorithms for comparison. Furthermore, to compare with an algorithm similar to our own, we have also modified and combined the schemes proposed in [107] and [110]. This combined scheme follows a similar beamforming approach as in [110] (therein called EE ZF), while using the the power allocation and RB assignment algorithm from [107] modified to be applicable to multiple-antenna BSs. Just as in [107] and [110], no antenna selection is considered for the combined scheme, but for a fair comparison, the constraints have been modified to match ours and the single-

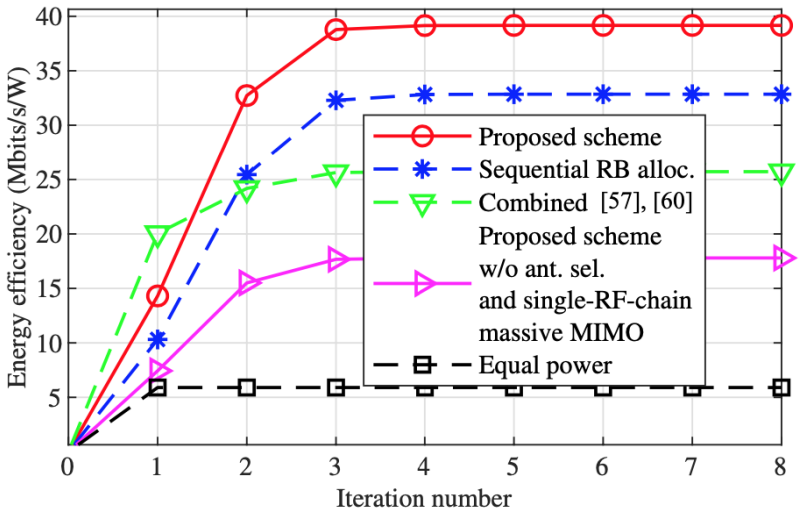

Figure 3.5: Comparison of convergence in (actual) EE between proposed scheme and other reference algorithms (shown in legend) vs. number of iterations.

RF-chain structure is assumed for mMIMO.

We also compare the EE performance of our scheme with no antenna selection for SCs and a conventional transceiver structure for the mMIMO macro BS.

As can be seen, even though the computational complexity is higher in our proposed algorithm, it converges within 3 iterations of the outer loop, and the convergence speed is acceptable when compared with the reference algorithms. As expected, our proposed scheme outperforms the other algorithms: the EE is about 12% higher than the second-best scheme of sequential RB allocation. This result shows the impact of an effective and efficient RB allocation method on the total EE of the system. The worst performance is for equal power allocation, in which even though antenna selection, the single-RF-chain structure, and RB assignment are considered, power is equally allocated between users regardless of their channel quality and minimum rate requirements.

Based on this figure, we can conclude that even though full power transmission increases the SE significantly, it performs the worst from the EE perspective. Moreover, our proposed scheme outperforms the combined schemes from [107] and [110], with about 37% higher EE. Without antenna selection, even though increasing the

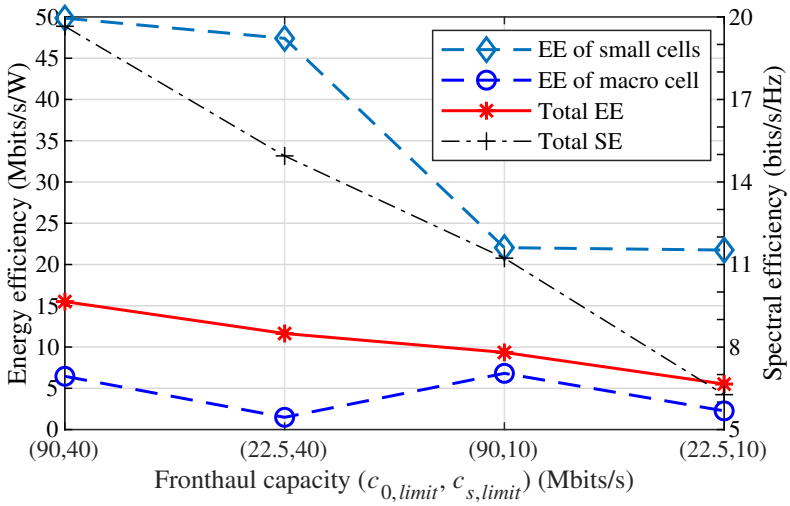

Figure 3.6: Impact of fronthaul capacity on total EE, on EE of small cell and macro tiers separately, and on SE

number of active antennas enhances the SE, since more power is consumed by each SC BS, the EE decreases. Moreover, deploying a conventional transceiver structure at the macro BS (with one RF chain per antenna) will lead to higher consumption of dynamic power. Thus, the EE of our proposed scheme but with a conventional macro BS transceiver structure and with all SC antennas active is only about twice that of the equal power case.

In previous figures, we have assumed there was enough fronthaul capacity to serve the users, but in Fig. 3.6 we limit fronthaul capacity to investigate the effect of the constraints in eq. (3.19c) in our EEmax problem. For this purpose, we change the number of users to $N_U = 60$ and κ_{min} to 1.28 Mbits/s.[4] In Fig. 3.6, EE is depicted vs. fronthaul capacity, where the pair of values on the x-axis indicate $(c_{0,limit}, c_{s,limit})$, i.e., the fronthaul capacity for the macro BS and for SC BSs, respectively. First, at the far left we assign sufficient fronthaul capacity for all BSs, such that all users can get their minimum required rate. Next, the fronthaul capacity for the macro BS is decreased. This leads to the macro BS becoming overloaded and it hence drops some of its users. All EE and SE values decrease as a result. Third, we keep the sufficient

[4]These values are simply examples intended to ensure the constraints in eq. (3.19b) are also active, so we can examine their interaction with the fronthaul capacity constraints.

fronthaul capacity for the macro BS and decrease the fronthaul capacity of the SC BSs. In this case, the total EE, SC EE, and SE all decrease even more, since the majority of users in the network are SC users, many of whom are now not receiving their minimum guaranteed rates. However, the EE of the macro BS remains about the same as it was initially. Finally, we decrease $c_{s,limit}$ for all BSs. As expected, the total EE and SE decreases even further with more users receiving even smaller rates. However, the EEs of the macro cell and SCs are about the same as for the (22.5,40) case and the (90,10) case, respectively. Hence, whether or not a tier is overloaded has little effect on the EE of the other tier.

Imperfect CSI can have a notable impact on the performance of cellular systems. Specifically, precoding techniques that null interference, like those we use in this chapter, are known to be somewhat sensitive to errors in CSI. Hence, herein we conduct a brief numerical examination of imperfect CSI and investigate the robustness of our proposed scheme to channel estimation error. The model we have adopted for imperfect CSI is given as [137]:

$$\mathbf{h}_{s,n,b}^{est} = \varsigma \mathbf{h}_{s,n,b} + \sqrt{1-\varsigma^2}\,\bar{\mathbf{h}}_{s,n,b}, \tag{3.28}$$

where $\mathbf{h}_{s,n,b}^{est} \in \mathbb{C}^{1\times N_s}$ is the estimated (small-scale fading) channel vector, $\mathbf{h}_{s,n,b} \in \mathbb{C}^{1\times N_s}$ is the actual channel vector (corresponding to perfect CSI), and $\bar{\mathbf{h}}_{s,n,b} \in \mathbb{C}^{1\times N_s} \sim \mathcal{CN}(0, \mathbf{I}_{N_s})$ is an independent error vector. The parameter ς, where $0 \leq \varsigma \leq 1$, represents the reliability of the channel estimate. When $\varsigma = 0$, there is a complete failure in the channel estimation, whereas for $\varsigma = 1$ the estimation is perfect and the error component in eq. (3.28) becomes zero.

The EE/SE performance vs. $(1-\varsigma)$ is depicted in Fig. 3.7. As can be seen, by decreasing ς both the EE and SE decrease, which is expected as the decreased CSI reliability/ increased channel estimation error naturally leads to the degradation of performance. The most significant decrease occurs for equal power allocation. Since the power allocation is not optimized, there is no opportunity in that regard

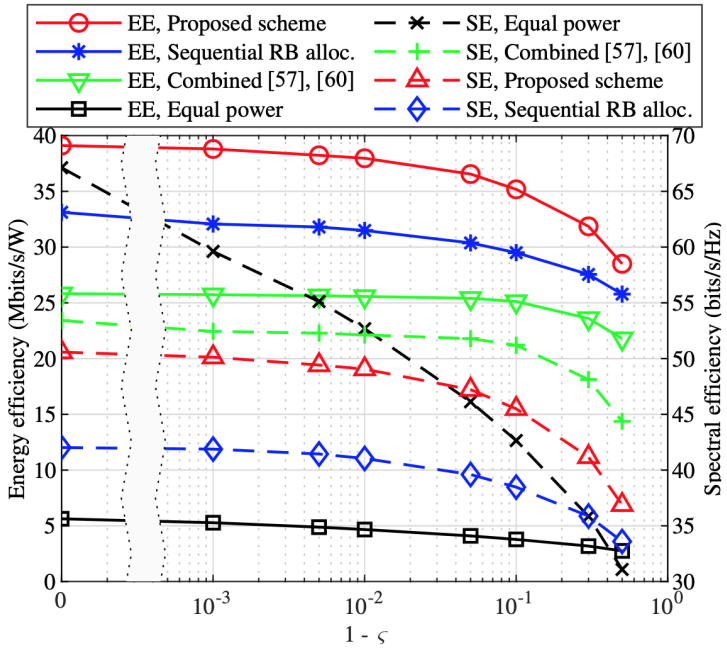

Figure 3.7: EE and SE of proposed scheme and other reference algorithms shown in legend vs. $1-\varsigma$, where ς represents the CSI reliability.

to mitigate interference by, for example, reducing the transmitted power by only allocating enough power to certain users such that they receive just their minimum guaranteed rates. Thus, the primary source of interference mitigation is due to the precoding, and as already mentioned, the precoding can be sensitive to CSI errors. Hence, for equal power allocation, both the EE and SE drop by over half when the CSI reliability drops from $\varsigma = 1$ (perfect CSI) to $\varsigma = 0.5$. The decrease in SE of our proposed method is sharper than for the remaining two reference schemes, indicating slightly less robustness in SE toward channel estimation error in our proposed method. However, the relative decrease in EE of our proposed scheme is less than that of sequential RB allocation for larger values of ς. Interestingly, the percentage drops in EE and SE for our proposed scheme as ς decreases are nearly identical, indicating a good trade-off between EE and SE. For sequential RB allocation, the relative drop in EE is faster than for SE, whereas for the combined schemes of [107] and [110], the reverse is true. Overall, if the reliability of channel estimation can be kept above $\varsigma = 0.9$, then the degradation in performance will also be fairly limited. In the case

of our proposed algorithm, when $\varsigma \geq 0.9$, both the EE and the SE lose no more than 10% in performance compared to having perfect CSI.

3.9 Summary

In this chapter, we have considered the DL of a two-tier HetNet, in which multiple-antenna SCs are coordinated to serve users. Even though the deployment of MIMO together with SCs improves the communication system's performance in terms of data rate and reliability, circuit energy consumption in such a network is a critical issue. To address this, an energy-efficient antenna selection and radio resource block assignment algorithm has been proposed for the SCs, and a single RF chain structure is considered for the mMIMO macro BS. Then, while coordinating transmissions between cells subject to user-centric clustering, an energy-efficient beamforming design and power allocation optimization problem with respect to the QoS requirement of users, transmit power budget of BSs, and fronthaul capacity has been formulated. The proposed optimization problem then has been solved using the Dinkelbach method. Finally, the simulation results have been provided to demonstrated the performance potential of our proposed algorithm in terms of energy efficiency and spectral efficiency.

Chapter 4

Iterative Matrix Inversion Methods for Precoding in Cell-Free Massive MIMO Systems

Linear precoding methods such as ZF are sufficient to achieve near-optimal performance in mMIMO systems. However, a key challenge in implementing these precoders can be a channel matrix inversion operation, which results in significant computational complexity in systems with large-scale antenna arrays. Several approaches have been proposed with the goal of reducing the computational complexity of matrix inversion associated with precoding in mMIMO systems based on the Jacobi (JC) method [73, 77, 78, 80, 81], Gauss-Seidel (GS) method [82], Newton-Schultz (NS) method [83, 85], and hyper-power (HP) method [86]. Nevertheless, to the best of our knowledge, there is no prior work investigating iterative matrix inversion methods for precoding in the context of CF mMIMO. In this chapter, we examine several iterative methods to calculate the precoding matrix in a CF mMIMO system. We also investigate their computational complexity and convergence rate in the presence of small- and large-scale fading and spatial correlation between antennas.

4.1 System model

We consider the downlink of a CF mMIMO system consisting of L APs each equipped with N antennas serving K single-antenna users. The received signal $y_k \in \mathbb{C}$ at user

k is

$$y_k = \sum_{l=1}^{L} \mathbf{g}_{lk}\mathbf{x}_l + n_k, \tag{4.1}$$

where $\mathbf{g}_{lk} \in \mathbb{C}^{1\times N}$ is the complex channel gain vector between user k and AP l, $\mathbf{x}_l \in \mathbb{C}^{N\times 1}$ is the complex-valued transmitted signal from AP l, and $n_k \sim \mathcal{CN}(0,1)$ is additive white Gaussian noise. The signal transmitted by AP l is

$$\mathbf{x}_l = \sqrt{\frac{P_t}{L}} \sum_{k=1}^{K} \sqrt{\upsilon_{lk}}\mathbf{w}_{lk}s_k, \tag{4.2}$$

where P_t is the total normalized transmit power (normalized relative to the noise power) of the system. This power is divided equally among the L APs, such that each AP has a transmit power limit of P_t/L. υ_{lk} is a power coefficient, representing the fraction of its maximum transmit power that AP l allocates to the data for user k. s_k is the data symbol intended for user k, with $\mathbb{E}\{|s_k|^2\} = 1$, and $\mathbf{w}_{lk} \in \mathbb{C}^{N\times 1}$ is the precoding vector at AP l for user k.

The channel gain vectors $\mathbf{g}_{lk}$ and precoding vectors $\mathbf{w}_{lk}$ can be collected together into system-wide matrices $\mathbf{G} \in \mathbb{C}^{K\times M}$ and $\mathbf{W} \in \mathbb{C}^{M\times K}$, respectively, where $M = LN$. We can similarly define other system-wide variables: the data vector $\mathbf{s} \in \mathbb{C}^{K\times 1}$, the power coefficient matrix $\boldsymbol{\Upsilon} \in \mathbb{R}_{\geq 0}^{M\times K}$, the transmitted signal vector $\mathbf{x} \in \mathbb{C}^{M\times 1}$, the noise vector $\mathbf{n} \in \mathbb{C}^{K\times 1}$, and the received signal vector $\mathbf{y} \in \mathbb{C}^{K\times 1}$. When considering the precoding method, we primarily focus on ZF precoding for this chapter. However, most of the matrix inversion techniques we examine can also be applied to matrices used in regularized ZF (RZF) and MMSE precoding.

Rewriting (4.1) and (4.2) in matrix form, we have

$$\mathbf{y} = \mathbf{G}\mathbf{x} + \mathbf{n} = \mathbf{G}\sqrt{\frac{P_t}{L}}(\boldsymbol{\Upsilon}^{\circ 1/2} \odot \mathbf{W})\mathbf{s} + \mathbf{n}, \tag{4.3}$$

We denote the Hadamard product in (4) as $\mathbf{W}_M$:

$$\mathbf{W}_M = \boldsymbol{\Upsilon}^{\circ 1/2} \odot \mathbf{W}. \tag{4.4}$$

To implement ZF precoding, we set $\mathbf{W}$ as [71]:

$$\mathbf{W} = \mathbf{G}^{\dagger} = \mathbf{G}^H(\mathbf{G}\mathbf{G}^H)^{-1}. \tag{4.5}$$

By further specifying that $\upsilon_{lk} = \upsilon_k$, i.e. the power coefficients are only dependent on the index k, it will guarantee that $\mathbf{G}\mathbf{W}_M$ is diagonal and there is no interference between users. If we define $\mathbf{\Upsilon}_M$ as

$$\mathbf{\Upsilon}_M = \begin{bmatrix} \sqrt{\upsilon_1} & 0 & \cdots & 0 \\ 0 & \sqrt{\upsilon_2} & \cdots & 0 \\ \vdots & \vdots & \ddots & \vdots \\ 0 & 0 & \cdots & \sqrt{\upsilon_K} \end{bmatrix} \in \mathbb{R}_{\geq 0}^{K \times K}, \tag{4.6}$$

we have $\mathbf{W}_M = \mathbf{W}\mathbf{\Upsilon}_M = \mathbf{G}^H(\mathbf{G}\mathbf{G}^H)^{-1}\mathbf{\Upsilon}_M$.

Finally, the received vector becomes

$$\mathbf{y} = \sqrt{\frac{P_t}{L}}\mathbf{G}\mathbf{G}^H(\mathbf{G}\mathbf{G}^H)^{-1}\mathbf{\Upsilon}_M\mathbf{s} + \mathbf{n} = \sqrt{\frac{P_t}{L}}\left[\sqrt{\upsilon_1}s_1,\ \sqrt{\upsilon_2}s_2,\ \ldots,\ \sqrt{\upsilon_K}s_K\right]^T + \mathbf{n}. \tag{4.7}$$

To satisfy the average power constraint per AP, we must have

$$\mathrm{tr}(\mathbb{E}\{\mathbf{x}_l\mathbf{x}_l^H\}) \leq P_t/L \tag{4.8a}$$

$$\mathrm{tr}(\mathbb{E}\{\mathbf{G}_l^H(\mathbf{G}\mathbf{G}^H)^{-1}\mathbf{\Upsilon}_M^2(\mathbf{G}\mathbf{G}^H)^{-1}\mathbf{G}_l\}) \leq 1, \tag{4.8b}$$

where $\mathbf{G}_l \in \mathbb{C}^{K \times N}$ denotes the N columns of $\mathbf{G}$ which correspond to AP l (i.e., columns $(l-1)N+1$ to lN). Unfortunately, (4.8b) is extremely difficult to calculate analytically. Since power allocation is not the focus of this chapter, we therefore have opted to instead satisfy *instantaneous* power constraints for the APs with respect to the precoding vectors. With this change, the expectation in (4.8a) becomes only over the data symbols s_k, and the expectation term in (4.8b) disappears.

For further simplicity, we follow a similar approach as in [138]. By assuming $\upsilon_1 = \upsilon_2 = \ldots = \upsilon_K$, (4.8b) can be written as

$$\upsilon^{(l)}\,\mathrm{tr}\left((\mathbf{G}\mathbf{G}^H)^{-1}\mathbf{G}_l\mathbf{G}_l^H(\mathbf{G}\mathbf{G}^H)^{-1}\right) \leq 1, \tag{4.9}$$

where $\upsilon^{(l)}$ is the power coefficient for AP l. The sub-optimal power coefficient becomes

$$\tilde{\upsilon} = \min_l \upsilon^{(l)} = \frac{1}{\max_l \mathrm{tr}(\mathbf{T}_l)}, \tag{4.10}$$

where $\mathbf{T}_l = (\mathbf{G}\mathbf{G}^H)^{-1}\mathbf{G}_l\mathbf{G}_l^H(\mathbf{G}\mathbf{G}^H)^{-1}$. It is shown in [138] that this solution has near-optimal performance while having smaller computational complexity. Then the transmitted signal $\mathbf{x}$ becomes

$$\mathbf{x} = \sqrt{\frac{P_t\tilde{\upsilon}}{L}}\mathbf{G}^H(\mathbf{G}\mathbf{G}^H)^{-1}\mathbf{s} = \sqrt{\frac{P_t\tilde{\upsilon}}{L}}\mathbf{G}^H\hat{\mathbf{s}}, \tag{4.11}$$

where we define $\hat{\mathbf{s}} = (\mathbf{G}\mathbf{G}^H)^{-1}\mathbf{s}$. To reduce the computational complexity of ZF precoding, we utilize iterative methods to find $(\mathbf{G}\mathbf{G}^H)^{-1}$ instead of direct methods.

In this chapter, we assume perfect channel state information (CSI) throughout, since the CSI accuracy generally does not affect the performance of the various methods relative to each other. Moreover, we assume spatially-correlated Rayleigh small-scale fading to make the system model more practical. We consider three different layouts for mMIMO systems: 1) standard (co-located) mMIMO; 2) completely distributed CF mMIMO, where each AP has only one antenna; 3) a partially-distributed CF system, in which a small number of antennas are co-located at each AP. For fair comparison, the total number of antennas M and the total system power P_t are set to the same value for all three cases.

4.2 Iterative Methods for Matrix Inversion

4.2.1 Jacobi and Gauss-Seidel Methods

We start with an examination of JC and GS, being two well-known methods for solving a set of linear equations. Between the two, GS has a better rate of convergence, since in each iteration, it sequentially updates each solution variable, using the most up-to-date value of the ones earlier in the sequence. However, JC is well suited for parallel and/or distributed computation which is desirable in many scenarios and useful for this work given the distributed nature of CF mMIMO. Both methods solve $\mathbf{A}\mathbf{x} = \mathbf{b}$ by iteratively calculating $\mathbf{x}_{n+1} = \mathbf{P}\mathbf{x}_n + \mathbf{q}$. The specifics of $\mathbf{P}$ and $\mathbf{q}$ for the two methods are given in Table 4.1. $\mathbf{D}$ contains the diagonal part of $\mathbf{A}$ and $\mathbf{L}$ and $\mathbf{U}$

Table 4.1: Update Variables for Jacobi and Gauss-Seidel Methods

Jacobi	Gauss-Seidel
$\mathbf{P} = -\mathbf{D}^{-1}(\mathbf{L}+\mathbf{U})$	$\mathbf{P} = -(\mathbf{D}+\mathbf{L})^{-1}(\mathbf{U})$
$\mathbf{q} = \mathbf{D}^{-1}\mathbf{b}$	$\mathbf{q} = (\mathbf{D}+\mathbf{L})^{-1}\mathbf{b}$

are the strictly lower and strictly upper triangular parts of $\mathbf{A}$ (i.e., not including the diagonal).

Before using JC and GS methods for matrix inversion in a mMIMO or CF mMIMO system, we first need to prove their convergence. We set $\mathbf{A} = \mathbf{G}\mathbf{G}^H$ and $\mathbf{b} = \mathbf{s}$; the methods will then solve for $\mathbf{x} = \hat{\mathbf{s}}$. It has been proven in [139] that the iterative scheme $\mathbf{x}_{n+1} = \mathbf{P}\mathbf{x}_n + \mathbf{q}$ is convergent if and only if every eigenvalue of $\mathbf{P}$ satisfies $|\lambda| < 1$, that is, the spectral radius $\rho(\mathbf{P}) < 1$. Furthermore, the methods converge faster the smaller the value $\rho(\mathbf{P})$ is [72].

To investigate the convergence, we examine the cumulative distribution function (CDF) of the spectral radius of $\mathbf{P}$ by Monte Carlo simulation, since an analytical determination of the eigenvalues when accounting for large-scale fading and spatial correlation is extremely difficult. We assume a total of $M = 128$ antennas and $K = 16$ users are present in the system. In the partially-distributed scenario, we assume that each AP has $N = 4$ antennas, so there are a total of $L = 32$ APs. All APs and users are uniformly distributed in a square area of 1×1 km^2. The distances measured between the users and APs are wrapped around to avoid boundary effects. For large-scale fading we use the propagation model suggested by [140], which is based on the 3GPP Urban Microcell model [135, Table B.1.2.1-1]. The spatial correlation matrix $\mathbf{R}_{lk}$ of the small-scale channel vector from multi-antenna AP l to user k is modeled based on the local scattering model described in [71, Ch. 2], which assumes all scatterers are near the users. More specifically, we assume a Gaussian distribution to the angles of arrival/departure of multipath components around the nominal central angle at the AP.

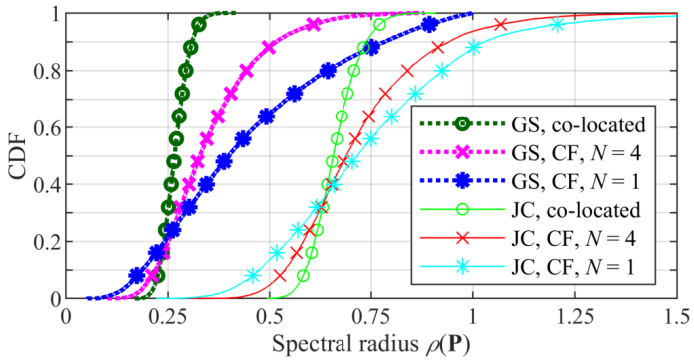

(a) CDFs of spectral radius $\rho(\mathbf{P})$ with small- and large-scale fading, without spatial correlation

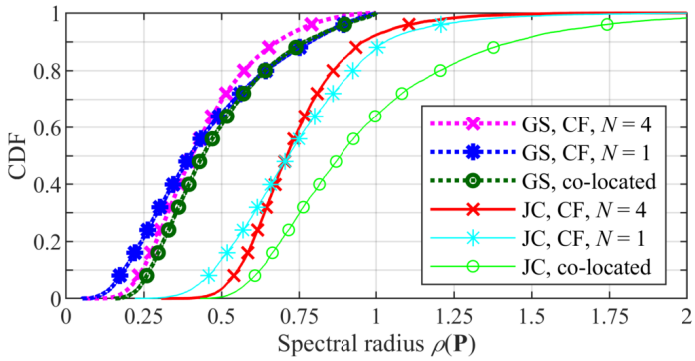

(b) CDFs of spectral radius $\rho(\mathbf{P})$ when considering small- and large-scale fading and spatial correlation

Figure 4.1: CDFs of spectral radius $\rho(\mathbf{P})$ for JC and GS methods when considering small-scale fading, large-scale fading, and spatial correlation in mMIMO and CF mMIMO systems

The simulated CDFs of the spectral radius for the three mMIMO layouts are presented in Fig. 4.1. In Fig. 4.1a, we have assumed no correlation between antennas (i.e., $\mathbf{R}_k = \mathbf{I}_M$) and only the effects of small- and large-scale fading on the spectral radius for the JC and GS methods are considered. Previous work such as [78, 80–82] has only considered small-scale fading for co-located mMIMO. As can be seen, by including large-scale fading, $\rho(\mathbf{P})$ is still always less than one for co-located mMIMO for this set of simulation parameters, so both the JC and GS methods converge and can be used for inverse matrix calculation. The CDF of the spectral radius of GS has smaller values than for JC, which matches expectations given it is known that GS converges faster than JC.

It can also be observed that the spectral radius of the JC method becomes larger

than one for CF mMIMO for both $N = 1$ and $N = 4$, and thus this method will not always converge for the specified simulation parameters. Hence, rather importantly, we can conclude that the JC method cannot be reliably used for matrix inversion in ZF precoding in CF mMIMO systems. In all scenarios the spectral radius of the GS method remains below 1, meaning it will converge. However, $\rho(\mathbf{P})$ is larger for the CF cases than for co-located mMIMO, so the convergence rate will be slower. In particular, we note that in the completely distributed case ($N = 1$), the spectral radius for GS can become very close to 1. Consequently, while it will still converge, it could do so very slowly, significantly hindering its use in practice. Overall, the results demonstrate the significant effects that the large-scale fading coefficients β_{mk} can have on the JC and GS convergence.

In Fig. 4.1b, along with small- and large-scale fading, spatial correlation has also been included. As noted earlier, for $N = 1$ the APs are sufficiently separated such that no spatial correlation exists between them. Thus, those curves are the same as in Fig. 4.1a. For co-located mMIMO, with the inclusion of spatial correlation, JC no longer always converges and the convergence rate of GS decreases significantly. Meanwhile, for partially- and fully-distributed CF mMIMO, the spectral radius CDFs for both JC and GS now lie to the left of those for co-located mMIMO, though the JC method still does not always converge. Thus, in conclusion, in our considered scenario with spatial correlation, JC can not be reliably used for matrix inversion, and using the GS method with CF mMIMO results in faster convergence than for co-located mMIMO.

We have demonstrated that the GS method converges for our simulation parameters. However, it is actually known that if $\mathbf{A}$ is Hermitian and positive definite, the GS method will converge regardless of its initialization point; [72, Thm. 10.1.2] has a proof[1] of this. Since we set $\mathbf{A} = \mathbf{G}\mathbf{G}^H$, it must be Hermitian and at least positive semi-definite, and will be positive definite if $\mathbf{G}$ is full rank. (If not, and $\mathbf{A}$ is only

[1]Technically, this proof is for a real-valued symmetric positive definite matrix, but for a complex-valued matrix, being Hermitian positive definite is the equivalent case.

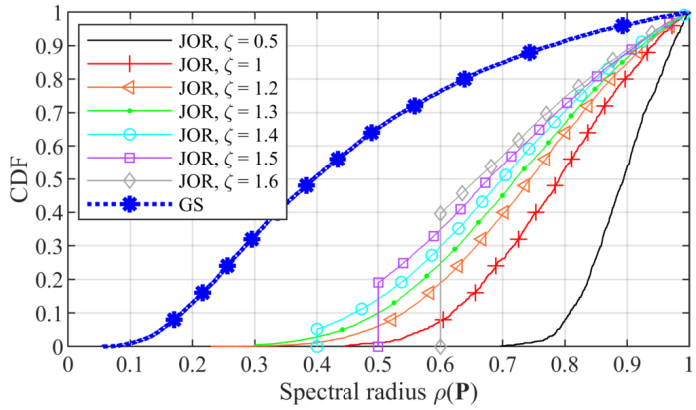

(a) $N = 1$

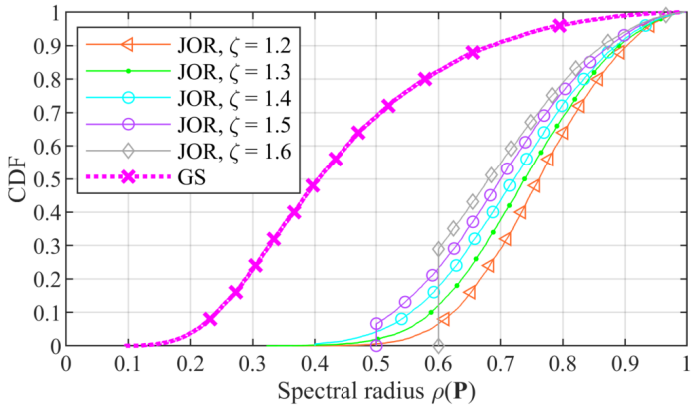

(b) $N = 4$

Figure 4.2: CDFs of spectral radius $\rho(\mathbf{P})$ of JOR method for different values of $\omega = \zeta/\rho(\mathbf{D}^{-1}\mathbf{A})$, with $\rho(\mathbf{P})$ of GS method for comparison.

positive semi-definite, it will not have an inverse anyway.) Our assumptions for the small-scale fading and the spatial correlation matrices result in $\mathbf{G}$ being full rank almost surely.

Although the JC method could converge under some other propagation model, these results demonstrate that convergence in general cannot be guaranteed for CF mMIMO. Therefore, the ordinary JC method should not be used in the context of CF mMIMO. In an attempt to find a modification to guarantee the convergence of the JC method, we investigate the impact of generalization through over-relaxation.

Generalization through over-relaxation

A generalization of the JC method is called the Jacobi over-relaxation (JOR) method [141, Ch. 4], in which a relaxation parameter ω is introduced such that the update of vector $\mathbf{x}_n$ is modified to

$$\begin{aligned}\mathbf{x}_{n+1} &= ((1-\omega)\mathbf{I}_K - \omega\mathbf{D}^{-1}(\mathbf{L}+\mathbf{U}))\mathbf{x}_n + \omega\mathbf{D}^{-1}\mathbf{b} \\ &= (\mathbf{I}_K - \omega\mathbf{D}^{-1}\mathbf{A})\mathbf{x}_n + \omega\mathbf{D}^{-1}\mathbf{b}.\end{aligned} \tag{4.12}$$

This method reduces to the regular JC method for $\omega = 1$. While the GS method will converge if $\mathbf{A}$ is Hermitian positive definite, the JC method requires that both $\mathbf{A}$ and $2\mathbf{D} - \mathbf{A}$ be Hermitian positive definite for convergence. Whether or not this condition is satisfied can be difficult to prove. However, for the JOR method, the latter requirement on $2\mathbf{D} - \mathbf{A}$ drops, and by putting a constraint on ω, proving the convergence of the method simplifies. It is proven in [141, Ch. 4] that for the JOR method, if $\mathbf{A}$ is Hermitian positive definite, then the method is convergent if $0 < \omega < \frac{2}{\rho(\mathbf{D}^{-1}\mathbf{A})}$.

Examination of (4.12) shows that the JOR method still follows the same update method of $\mathbf{x}_{n+1} = \mathbf{P}\mathbf{x}_n + \mathbf{q}$, where $\mathbf{P} = \mathbf{I}_K - \omega\mathbf{D}^{-1}\mathbf{A}$ and $\mathbf{q} = \omega\mathbf{D}^{-1}\mathbf{b}$. As such, it too will converge provided that $\rho(\mathbf{P}) < 1$. Fig. 4.2 shows the CDF of the spectral radius of $\mathbf{P}$ for the JOR method for different values of ω, along with $\rho(\mathbf{P})$ for the GS method for comparison. As expected, this method is convergent for any $0 < \omega < \frac{2}{\rho(\mathbf{D}^{-1}\mathbf{A})}$, however the GS method still displays a smaller spectral radius, and thus a faster convergence rate.

As can be seen, the spectral radius of JOR has a lower bound (e.g., with $\omega = 1.6/\rho(\mathbf{D}^{-1}\mathbf{A})$, the lower bound is 0.6). To explain this, we first note from the definition of eigenvectors and eigenvalues $\mathbf{M}\mathbf{v}_m = \lambda_m\mathbf{v}_m$, it follows that for any non-zero real constant c, the eigenvalues of $c\mathbf{M}$ are $c\lambda_m$, and the eigenvalues of $\mathbf{M}+c\mathbf{I}$ are λ_m+c. Let $\mathbf{M} = \mathbf{D}^{-1}\mathbf{A}$. Then,

$$\rho(\mathbf{I}_K - \omega\mathbf{M}) = \rho(\omega\mathbf{M} - \mathbf{I}_K) = \max_m \ |\omega\lambda_m - 1|. \tag{4.13}$$

By setting $\omega = \frac{\zeta}{\rho(\mathbf{D}^{-1}\mathbf{A})} = \frac{\zeta}{\max_m |\lambda_m|}$ and noting $|\omega\lambda_m - 1| = |1 - \omega\lambda_m|$, the smallest possible value of (4.13) will occur for the largest magnitude eigenvalue $|\lambda_m|$ if λ_m is positive, since the largest possible value is subtracted from 1. In this event $|\omega\lambda_m - 1| = \zeta - 1$, and thus we can conclude that for the JOR method, $\rho(\mathbf{P}) \geq \zeta - 1$.

The advantage of the JOR method is its compatibility with parallel implementation, however, the dependence of its performance on the value of ω and the extra complexity of finding $\rho(\mathbf{D}^{-1}\mathbf{A}) < 1$ to determine the maximum permissible value of ω need to be taken into consideration.

4.2.2 Hyper-Power Method (including Newton-Schultz)

While the JC and GS methods are computationally efficient for matrix inversion, as we have shown, JC is not reliably applicable to CF mMIMO, nor to co-located mMIMO in the presence of spatial correlation. Meanwhile, although the GS method is guaranteed to converge as long as the matrix being inverted is Hermitian positive definite, due to its computational structure[2], parallel implementation is not possible.

Amongst methods to find the inverse of a matrix by solving $\mathbf{AX} = \mathbf{I}$, the Neumann series expansion and the NS method are fairly well-known. Due to the significant performance deficiency of the NSE method reported in [142], the NS method and its generalization, the HP method, are investigated in this work.

In the NS method, the inverse of $\mathbf{A}$ can be obtained by following the below procedure:

$$\mathbf{X}_{n+1} = \mathbf{X}_n + \mathbf{X}_n(\mathbf{I}_K - \mathbf{A}\mathbf{X}_n) = \mathbf{X}_n(2\mathbf{I}_K - \mathbf{A}\mathbf{X}_n), \tag{4.14}$$

where n is the iteration number.

A generalized form of NS called the hyper-power method has been introduced in [143]. It is defined as

$$\mathbf{X}_{n+1} = \mathbf{X}_n \, \mathrm{p}_{r-1}(\mathbf{I}_K - \mathbf{A}\mathbf{X}_n), \tag{4.15}$$

[2]In the GS method, the update of the ith element of $\mathbf{x}_{n+1}$ uses the updated elements j for $j < i$ [72, Eq. (11.2.3)]. Consequently, the elements in $\mathbf{x}_{n+1}$ must be computed successively rather than in parallel.

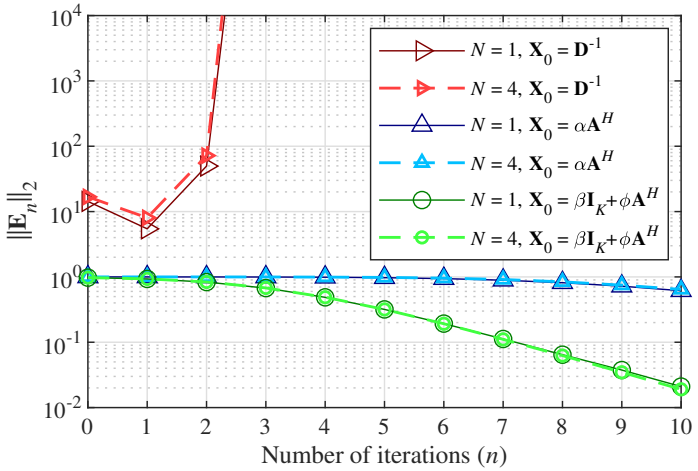

Figure 4.3: Average 2-norm of error matrix $\|\mathbf{E}_n\|_2$ vs. number of iterations n for different initialization points for HP-based methods in CF mMIMO systems when considering small- and large-scale fading and spatial correlation in channel vectors

where $\mathrm{p}_j(\mathbf{Z}) = 1 + \mathbf{Z} + ... + \mathbf{Z}^j$ $(j \in \mathbb{Z}^+)$. For $r = 2$, this method reduces to NS.

To prove that the HP method converges as the iterations progress, we need to prove that the norm of the error matrix $\|\mathbf{E}_0\| = \|\mathbf{I}_K - \mathbf{A}\mathbf{X}_0\| < 1$.

Proof: We start by expanding (4.15) as

$$\mathbf{X}_n = \mathbf{X}_{n-1}[\mathbf{I}_K + (\mathbf{I}_K - \mathbf{A}\mathbf{X}_{n-1}) + (\mathbf{I}_K - \mathbf{A}\mathbf{X}_{n-1})^2 + \cdots + (\mathbf{I}_K - \mathbf{A}\mathbf{X}_{n-1})^{r-1}]. \tag{4.16}$$

By substituting $\mathbf{E}_n = \mathbf{I}_K - \mathbf{A}\mathbf{X}_n$ we have

$$\mathbf{X}_n = \mathbf{X}_{n-1}(\mathbf{I}_K + \mathbf{E}_{n-1} + \mathbf{E}_{n-1}^2 + \cdots + \mathbf{E}_{n-1}^{r-1}). \tag{4.17}$$

Thus, the error matrix in iteration n can be calculated as

$$\begin{aligned}\mathbf{E}_n &= \mathbf{I}_K - \mathbf{A}\mathbf{X}_{n-1}(\mathbf{I}_K + \mathbf{E}_{n-1} + \mathbf{E}_{n-1}^2 + \cdots + \mathbf{E}_{n-1}^{r-1}) \\ &= \mathbf{I}_K - (\mathbf{I}_K - \mathbf{E}_{n-1})(\mathbf{I}_K + \mathbf{E}_{n-1} + \mathbf{E}_{n-1}^2 + \cdots + \mathbf{E}_{n-1}^{r-1}) \\ &= \mathbf{E}_{n-1}^r = \mathbf{E}_0^{r^n},\end{aligned} \tag{4.18}$$

where the last equality follows by induction. From the property $\|\mathbf{Y}\mathbf{Z}\| \leq \|\mathbf{Y}\|\,\|\mathbf{Z}\|$, by induction we also have $\left\|\mathbf{E}_0^{r^n}\right\| \leq \|\mathbf{E}_0\|^{r^n}$. Thus if $\|\mathbf{E}_0\| < 1$, subsequently $\|\mathbf{E}_l\| \to 0$ as $l \to \infty$ and convergence is guaranteed.

Consequently, in this method the most crucial parameter to ensure convergence and also determine the convergence rate is the initialization point $\mathbf{X}_0$, which will be discussed in more detail later. The next important parameter is r; to find its optimum value, its effect on both the convergence rate and computational complexity needs to be considered.

As just discussed, the convergence is dependent on the error in each iteration. Thus, for $\|\mathbf{E}_0\| < 1$, the HP method is convergent with an order of convergence of r. Based on (4.18), to decrease the overall error we have three options: choose an initialization point for which $\|\mathbf{E}_0\|$ is feasibly small, increase the number of iterations, and increase the value of r. Increasing the number of iterations is not practical since it leads to higher computational complexity and convergence time. In considering r, we note that a typical method of calculating (4.17) is by following a Horner scheme fashion [144] as:

$$\mathbf{X}_{n+1} = \mathbf{X}_n(\mathbf{I}_K + \mathbf{E}_n(\mathbf{I}_K + \dots \mathbf{E}_n(\mathbf{I}_K + \mathbf{E}_n)\dots)), \tag{4.19}$$

which performs r matrix multiplications per iteration. The computational efficiency of this scheme, as introduced by [145], is defined as $E_c = r^{1/\theta}$, where r denotes the local convergence rate and $\theta = r$ is the number of matrix multiplications per iteration.

It is shown in [144] that $r = 3$ leads to the optimum value for the computational efficiency. Then, (4.19) can be simplified as

$$\mathbf{X}_{n+1} = \mathbf{X}_n(\mathbf{I}_K + \mathbf{E}_n(\mathbf{I}_K + \mathbf{E}_n)) = \mathbf{X}_n(\mathbf{I}_K + \mathbf{E}_n + \mathbf{E}_n^2). \tag{4.20}$$

Figure 4.3 shows $\|\mathbf{E}_n\|_2$ for CF mMIMO in the presence of spatial correlation. As expected, the channel of our CF system is no longer diagonally dominant (after including large-scale fading and correlation), so choosing $\mathbf{X}_0 = \mathbf{D}^{-1}$ again leads to non-convergence. Since there are several matrix inversion initialization points considered in the related literature, we investigate the performance of one of the most well-known ones in our system. The proposed initialization point in [146], which is

widely used, is given by

$$\mathbf{X}_0 = \alpha \mathbf{A}^H \tag{4.21}$$

such that the positive real coefficient α satisfies $\|\mathbf{E}_0\| < 1$.

To find a proper value for the coefficient α for CF mMIMO systems, we utilize [146, Thm. 2], which states convergence will occur if

$$0 < \alpha < \frac{2}{\lambda_1(\mathbf{A}\mathbf{A}^H)}, \tag{4.22}$$

where $\lambda_1(\mathbf{A}\mathbf{A}^H)$ is the largest eigenvalue of $\mathbf{A}\mathbf{A}^H$. Knowing the convergence interval for α, to boost the performance we need its optimal value that minimizes $\|\mathbf{I}_K - \mathbf{A}\mathbf{X}_0\|$. By following a similar approach as in [147], the optimal α is

$$\alpha = \frac{2}{\lambda_1(\mathbf{A}\mathbf{A}^H) + \lambda_k(\mathbf{A}\mathbf{A}^H)}, \tag{4.23}$$

where $\lambda_k(\mathbf{A}\mathbf{A}^H)$ is the smallest non-zero eigenvalue of $\mathbf{A}\mathbf{A}^H$. Note also since $\mathbf{A}$=$\mathbf{A}^H$, $[\lambda_m(\mathbf{A}\mathbf{A}^H)]\mathbf{v}_m = \mathbf{A}\mathbf{A}\mathbf{v}_m = \mathbf{A}[\lambda_m(\mathbf{A})]\mathbf{v}_m = [\lambda_m(\mathbf{A})]^2\mathbf{v}_m$. Thus, the eigenvalues of $\mathbf{A}\mathbf{A}^H$ are the squares of the eigenvalues of $\mathbf{A}$.

Based on the simulation results in Fig. 4.3, even though this choice of initialization point leads to convergence, the convergence rate is quite slow, and neither increasing the number of iterations nor choosing a higher value of r leads to faster convergence. By taking advantage of matrix $\mathbf{A}$ being Hermitian positive definite, a better initialization point has been proposed in [148] to accelerate the convergence:

$$\mathbf{X}_0 = \beta \mathbf{I}_K + \phi \mathbf{A}^H, \tag{4.24}$$

where

$$\beta = \frac{8(\lambda_1(\mathbf{A}) + \lambda_k(\mathbf{A}))}{\lambda_1^2(\mathbf{A}) + \lambda_k^2(\mathbf{A}) + 6\lambda_1(\mathbf{A})\lambda_k(\mathbf{A})}, \tag{4.25}$$

$$\phi = \frac{-8}{\lambda_1^2(\mathbf{A}) + \lambda_k^2(\mathbf{A}) + 6\lambda_1(\mathbf{A})\lambda_k(\mathbf{A})}. \tag{4.26}$$

As can be seen in Fig. 4.3, this initialization point results in faster convergence. However, a bottleneck in terms of complexity is finding the largest and smallest non-zero eigenvalues of matrix $\mathbf{A}$.

In practice, it is computationally complex to calculate the eigenvalues of a matrix directly. To reduce the complexity, we instead use bounds from the literature for the maximum and minimum eigenvalues of a matrix. Specifically, we first consider two well-known bounds proposed in [149]:

$$m + s/\sqrt{K-1} \leq \lambda_1(\mathbf{A}) \leq m + s\sqrt{K-1}\,, \tag{4.27}$$

$$m - s\sqrt{K-1} \leq \lambda_k(\mathbf{A}) \leq m - s/\sqrt{K-1}\,, \tag{4.28}$$

where

$$m = \frac{\mathrm{tr}(\mathbf{A})}{K}, \tag{4.29}$$

$$s = \sqrt{\frac{\mathrm{tr}(\mathbf{A}^2)}{K} - m^2}\,. \tag{4.30}$$

To get the values of β and ϕ, we take the upper bounds in (4.27) and (4.28), since they provide better eigenvalue estimates. Tighter bounds have been derived in [150], which are given as

$$\frac{\mathrm{tr}(\mathbf{A})}{K} + \frac{\mathrm{tr}(\mathbf{C}^2)}{K}\left(\frac{1+(K-1)^{2a-1}}{(K-1)^{2a-1}\,\mathrm{tr}(\mathbf{C}^{2a})}\right)^{\frac{1}{2a}} \leq \lambda_1(\mathbf{A}) \leq \frac{\mathrm{tr}(\mathbf{A})}{K} + \left(\frac{1+(K-1)^{2a-1}}{(K-1)^{2a-1}\,\mathrm{tr}(\mathbf{C}^{2a})}\right)^{-\frac{1}{2a}} \tag{4.31}$$

$$\lambda_k(\mathbf{A}) \leq \frac{\mathrm{tr}(\mathbf{A})}{K} - \frac{\mathrm{tr}(\mathbf{C}^2)}{K}\left(\frac{1+(K-1)^{2a-1}}{(K-1)^{2a-1}\,\mathrm{tr}(\mathbf{C}^{2a})}\right)^{\frac{1}{2a}} \tag{4.32}$$

where $\mathbf{C} = \mathbf{A} - \frac{\mathrm{tr}(\mathbf{A})}{K}\mathbf{I}_K$ and $a \in \mathbb{Z}^+$. If a is set to 1, the bounds reduce to those given in (4.27) and (4.28).

4.2.3 The Matrix Pseudoinverse and Factorized HP Methods

Thus far, our goal has been to calculate $(\mathbf{G}\mathbf{G}^H)^{-1}$ for CF and co-located mMIMO systems. However, by finding Moore-Penrose pseudoinverse $\mathbf{G}^\dagger$, both the power coefficients given in (4.10) and the precoding matrix can be obtained. The pseudoinverse of $\mathbf{G}$ is given earlier in (4.5).

The HP method for finding the pseudoinverse is given by replacing $\mathbf{A}$ with $\mathbf{G}$ in (4.15) [144]:

$$\hat{\mathbf{X}}_{n+1} = \hat{\mathbf{X}}_n \, \mathrm{p}_{r-1}(\mathbf{I}_K - \mathbf{G}\hat{\mathbf{X}}_n). \tag{4.33}$$

Proving that the HP method for the pseudoinverse converges follows straightforwardly by replacing $\mathbf{A}$ with $\mathbf{G}$ in (4.16)–(4.18). Consequently, convergence will occur if $\left\|\hat{\mathbf{E}}_0\right\| = \left\|\mathbf{I}_K - \mathbf{G}\hat{\mathbf{X}}_0\right\| < 1$. It is proven in [151] that the optimal initialization point that minimizes $\left\|\hat{\mathbf{E}}_0\right\|$ for computing the pseudoinverse is

$$\hat{\mathbf{X}}_0 = \alpha \mathbf{G}^H, \tag{4.34}$$

where

$$\alpha = \frac{2}{\lambda_1(\mathbf{G}\mathbf{G}^H) + \lambda_k(\mathbf{G}\mathbf{G}^H)}. \tag{4.35}$$

To decrease the computational complexity of finding the initialization point, a similar initialization point with $\alpha = 2/\mathrm{tr}(\mathbf{G}\mathbf{G}^H)$ [148] can be considered, which we will show has acceptable performance.

Fig. 4.4a shows the normalized[3] (to account for the different number of matrix elements) 2-norm of the error matrix $\frac{\|\mathbf{E}_n\|_2}{K}$ or $\frac{\|\hat{\mathbf{E}}_n\|_2}{\sqrt{MK}}$ vs. the number of iterations of the HP method for both the inverse of $\mathbf{A}$ and the pseudoinverse of $\mathbf{G}$. As can be seen, the pseudoinverse with initialization point given by (4.35) converges much faster than the inverse with the similar initialization point given by (4.23). However, the pseudoinverse also has a higher computational complexity per iteration, since its calculation of $\hat{\mathbf{E}}_n$ involves multiplication of a $K \times M$ matrix $\mathbf{G}$ by an $M \times K$ matrix $\hat{\mathbf{X}}_n$, compared to multiplying two $K \times K$ matrices $\mathbf{A}$ and $\mathbf{X}_n$ in $\mathbf{E}_n$ for the inverse. By using the better initialization point for the inverse given by (4.24), it ends up converging similarly to the pseudoinverse. We also note that the pseudoinverse using $\hat{\mathbf{X}}_0 = 2\mathbf{G}^H/\mathrm{tr}(\mathbf{G}\mathbf{G}^H)$ performs and converges similarly to using the optimal value of α. The slopes of the lower three curves are almost identical.

[3]The normalization also makes the metric similar in nature to the normalized root mean square error (NRMSE) of the solution. The metric would equal the NRMSE if the Frobenius norm was used instead of the 2-norm.

Unfortunately, the convergence is still rather slow (needing numerous iterations) even when considering better initialization points. Another parameter that has a great impact on the convergence is r. As discussed before, increasing r above its optimal value of 3 will normally decrease the computational efficiency of calculating the matrix inverse[4] using the HP method. However, by utilizing improved HP methods such as those proposed in [144, 153–157], one can further increase the computational efficiency while increasing r by decreasing the number of required matrix multiplications each iteration. This is accomplished by proper factorization of the matrix polynomial $\mathrm{p}_{r-1}(\mathbf{Z})$, defined earlier as part of (4.15).

The authors of [144] have proposed a factorization method that results in only 5 matrix multiplications being required for $r = 9$. This was later improved upon in [156], which has provided a method for $r = 15$ that requires 6 matrix multiplications. The polynomial $p_{14}(\mathbf{Z})$ can be factored as:

$$\mathrm{p}_{14}(\mathbf{Z}) = c\,\mathrm{u}_5(\mathbf{Z}); \tag{4.36a}$$

$$\begin{aligned}\mathrm{u}_5(\mathbf{Z}) = \mathrm{u}_4(\mathbf{Z})\left(\mathrm{u}_4(\mathbf{Z}) + a_{5,3}\,\mathrm{u}_3(\mathbf{Z}) + a_{5,2}\mathbf{Z}^2 + a_{5,1}\mathbf{Z} + a_{5,0}\right) + b_{5,3}\,\mathrm{u}_3(\mathbf{Z}) + b_{5,2}\mathbf{Z}^2 \\ + b_{5,1}\mathbf{Z} + b_{5,0};\end{aligned} \tag{4.36b}$$

$$\mathrm{u}_4(\mathbf{Z}) = \mathrm{u}_3(\mathbf{Z})\left(\mathrm{u}_3(\mathbf{Z}) + a_{4,2}\mathbf{Z}^2 + a_{4,1}\mathbf{Z} + a_{4,0}\right) + b_{4,2}\mathbf{Z}^2 + b_{4,1}\mathbf{Z} + b_{4,0}; \tag{4.36c}$$

$$\mathrm{u}_3(\mathbf{Z}) = \mathbf{Z}^2\left(\mathbf{Z}^2 + a_{3,1}\mathbf{Z} + a_{3,0}\right) + b_{3,1}\mathbf{Z} + b_{3,0}, \tag{4.36d}$$

where $a_{i,j}, b_{i,j}$, and c are real-valued constants. There are several possible solutions for the values of these constants; [156, Eq. (3.6)] gives one of them.

Recall that the computational efficiency is defined as $E_c = r^{1/\theta}$ for the HP method, where θ is the number of matrix multiplications. The factorization in [144] for $r = 9$

[4]Much the same situation also holds for the pseudoinverse; Exercise 23 in [152, Ch. 7.7] covers the optimal r value in that case, and shows it depends on the ratio n/m for the $n \times m$ matrix being pseudo-inverted.

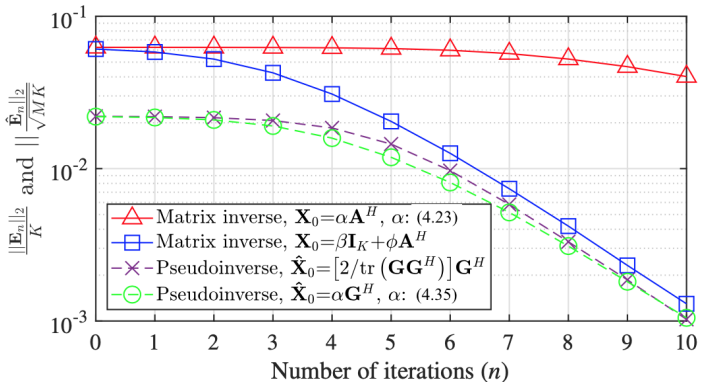

(a) Normalized error matrix 2-norms vs. number of iterations when using HP method with $r = 3$

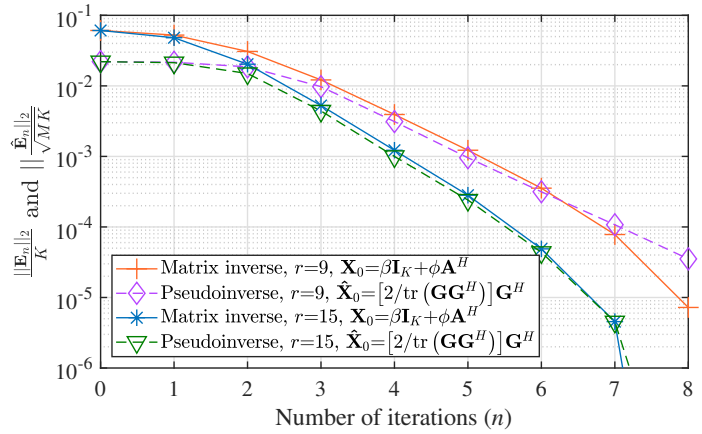

(b) Normalized error matrix 2-norms vs. number of iterations when using HP method with larger values of r

Figure 4.4: Comparison of $\frac{\|\mathbf{E}_n\|_2}{K}$ for matrix inverse and $\frac{\|\hat{\mathbf{E}}_n\|_2}{\sqrt{MK}}$ for pseudoinverse vs. number of iterations when using HP method different values of r in a CF mMIMO system with $N = 4$

results in $E_c = 9^{1/5} \approx 1.55$, which is higher than for $r = 3$ ($E_c = 3^{1/3} \approx 1.44$). The above factorization from [156] yields the best practical[5] computational efficiency of $E_c = 15^{1/6} \approx 1.57$.

Fig. 4.4b compares the convergence of the factorized HP methods for the inverse and pseudoinverse for these higher values of r. For $r = 9$, both inverse types display faster convergence than for $r = 3$. The pseudoinverse at first outperforms the inverse with initialization point given by (4.24), however after more iterations, the error matrix norms converge to each other. Much like in Fig. 4.4a, the convergence of the inverse with $\mathbf{X}_0$ given by (4.21) is considerably worse; thus, we do not depict it in Fig. 4.4b. For $r = 15$, the convergence is even faster for the inverse (e.g., $\|\mathbf{E}_n\|_2/K < 10^{-4}$ at $n = 6$), while the pseudoinverse also shows desirable performance. However, with higher values of r also comes higher computational complexity per iteration.

4.3 Scalable Cell-Free Massive MIMO

In this section, we incorporate LLSFB AP selection as proposed in [104]. By applying AP selection, the effective channel matrix for the network becomes sparser, which affects the convergence properties of the iterative inversion methods (see e.g. [158]). Lets denote $\mathcal{L}_k \subseteq \{1, ..., L\}$ as the subset of APs that serve user k, the block-diagonal binary $M \times M$ clustering matrix $\mathbf{D}_k$ for user k is then defined as

$$\mathbf{D}_k = \text{diag}(\mathbf{D}_{1k}, \ldots, \mathbf{D}_{Lk}), \tag{4.37}$$

where $\mathbf{D}_k$ is $\mathbf{I}_N$ if AP l serves user k and $\mathbf{0}_N$ otherwise. Then, we use partial zero-forcing (P-ZF) precoding[6] to calculate the precoding vector of user k as

[5]Higher computational efficiencies are theoretically possible, but they would require r to be at least 24 at minimum. This high a value of r, combined with the effects of numerical roundoff errors, means that implementing such a scheme would likely be impractical [156].

[6]This is the same as partial regularized zero-forcing (P-RZF) precoding in [34] except without the regularization term in the inverse. The power allocated to each user in the regularization term of P-RZF must be optimized to maximize the system performance, which is outside the scope of this work. However, the same methodology for matrix inversion can still be applied to P-RZF as we do for P-ZF in this section.

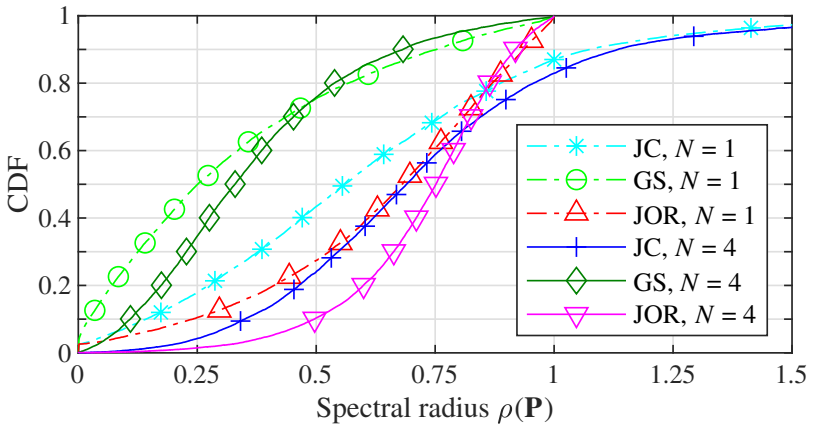

Figure 4.5: CDFs of spectral radius $\rho(\mathbf{P})$ for JC, GS, and JOR methods for a scalable CF mMIMO system; $N = \{1, 4\}$, JOR uses $\omega = 1/\rho(\mathbf{D}^{-1}\mathbf{A})$

$$\mathbf{w}_k^{\text{P-ZF}} = \left[\mathbf{D}_k \mathbf{G}_{\mathcal{S}_k}^H (\mathbf{G}_{\mathcal{S}_k} \mathbf{D}_k \mathbf{G}_{\mathcal{S}_k}^H)^{-1}\right]_{:,1} \tag{4.38}$$

where $\mathcal{S}_k$ is the set of users served at least in part by the same APs as user k, including user k itself. $\mathbf{G}_{\mathcal{S}_k} \in \mathbb{C}^{|\mathcal{S}_k| \times M}$ is obtained by including the channel (row) vectors of the users in $\mathcal{S}_k$, where it is specified that the first row of $\mathbf{G}_{\mathcal{S}_k}$ is the channel row vector of user k. (The order of the remaining users does not matter in this case.) Thus, it is the first column of the matrix calculated by the terms inside the square brackets in (4.38) that serves as the precoding vector for user k.

Here, we want to examine the effect of AP selection on the convergence of selected iterative methods. As seen in (4.38), the matrix being inverted is now $\mathbf{A} = \mathbf{G}_{\mathcal{S}_k} \mathbf{D}_k \mathbf{G}_{\mathcal{S}_k}^H \in \mathbb{C}^{|\mathcal{S}_k| \times |\mathcal{S}_k|}$. A new consideration is that the effective channel matrix $\mathbf{G}_{\mathcal{S}_k} \mathbf{D}_k$ (or equivalently $\mathbf{G}_{\mathcal{S}_k} \mathbf{D}_k^{1/2}$) becomes much sparser with many elements (i.e., those corresponding to antennas not serving the user) equal to zero; this can affect the rank and invertibility of $\mathbf{A}$. Along with the selection condition in (2.22), the system must also ensure the total number of users being served jointly by the APs does not exceed the total number of antennas at those APs, while still assigning at least one AP to each user. This new factor comes more into play the fewer the number of APs that serve a given user (especially if a user is only served by one AP) and the fewer antennas at the APs. Meeting these constraints means that $\mathbf{A}$ will still be

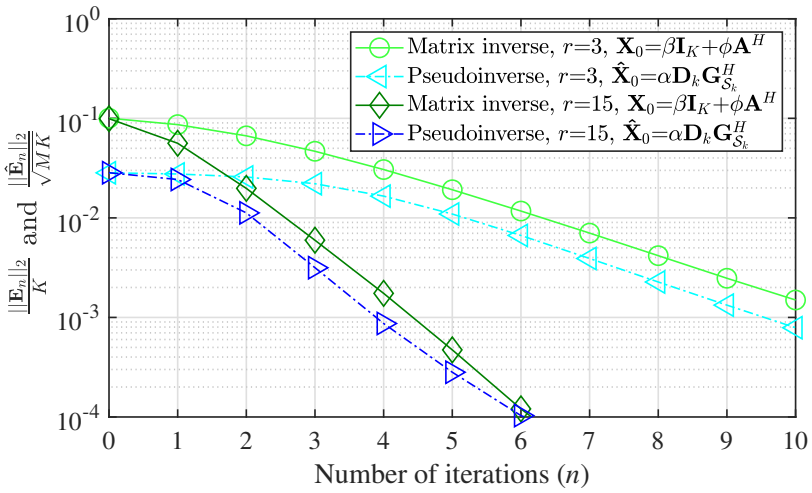

Figure 4.6: $\frac{\|\mathbf{E}_n\|_2}{K}$ and $\frac{\left\|\hat{\mathbf{E}}_n\right\|_2}{\sqrt{MK}}$ vs. number of iterations for HP method with different values of r for a scalable CF mMIMO system

Hermitian and positive definite and convergence will be guaranteed. Otherwise, $\mathbf{A}$ can be rank-deficient and not have an inverse.

The CDFs of the spectral radius of $\mathbf{P}$ for the JC, GS, and JOR methods are depicted in Fig. 4.5. The curves show a similar behaviour as those obtained earlier for conventional CF mMIMO. Similar to Fig. 4.2, $\rho(\mathbf{P})$ for JC is larger than 1, but both the GS and JOR methods converge with $\rho(\mathbf{P}) < 1$. Increasing the number of antennas per AP from $N = 1$ to $N = 4$ causes $\rho(\mathbf{P})$ for GS and JOR to reduce, thus making those two methods converge faster. Comparing Figs. 4.2 and 4.5 indicates that by considering user-centric AP selection to make CF mMIMO scalable, with fewer APs serving each user, the convergence rate for both the GS and JOR methods decreases; $\rho(\mathbf{P})$ is smaller in Fig. 4.2 than in Fig. 4.5.

Fig. 4.6 depicts the normalized 2-norm of the error matrix $\frac{\|\mathbf{E}_n\|_2}{K}$ or $\frac{\|\hat{\mathbf{E}}_n\|_2}{\sqrt{MK}}$ vs. the number of iterations of the HP method for both the matrix inverse and the pseudoinverse. Similar to earlier, we use the initialization point $\mathbf{X}_0 = \beta\mathbf{I}_{|\mathcal{S}_k|} + \phi\mathbf{A}^H$ for the inverse, with β and ϕ given by (4.25) and (4.26), respectively; the maximum and minimum eigenvalues are approximated with the upper bounds of (4.27)–(4.30), replacing K with $|\mathcal{S}_k|$. Likewise, for the pseudoinverse, we set $\hat{\mathbf{X}}_0 = \alpha(\mathbf{G}_{\mathcal{S}_k}\mathbf{D}_k)^H$, with $\alpha = 2/\mathrm{tr}(\mathbf{G}_{\mathcal{S}_k}\mathbf{D}_k\mathbf{G}_{\mathcal{S}_k}^H)$. As seen, for $r = 3$, both types of inverse converge,

though somewhat slowly. Increasing r to 15 leads to a more acceptable convergence rate using fewer iterations. Much like what was seen in Fig. 4.4, the performances of both inverses are similar and converge to each other after a few iterations. However, the convergence for scalable CF mMIMO in Fig. 4.6 is again slower than what was seen in Fig. 4.4. It should also be noted that for the inverse, the same additional AP selection conditions as earlier in this section still apply, to guarantee $\mathbf{A}$ is positive definite. In contrast, the pseudoinverse does not need to satisfy these conditions, as the matrix being pseudo-inverted need not have full rank.

4.4 Computational Complexity

We calculate the computational complexity of the matrix inversion methods examined in this chapter in terms of the number of real-valued floating point operations (flops) required, considering operations on a mixture of real and complex numbers. We generally use [72, 159] as a guide for calculating the complexity of the various operations. Finding the squared magnitude of a complex number requires 3 flops (2 multiplications and one addition). Multiplying two complex numbers requires 4 real multiplications and 2 real summations (6 flops in total) and adding complex numbers consists of 2 real summations (2 flops). However, multiplying a real number times a complex one only requires 2 flops, and adding a real number to a complex one is 1 flop. Calculating a square root is not itself a flop, but has $\mathcal{O}(1)$ complexity. The complexity of the methods is summarized in Table 4.2, where we also break down the total flops into multiplications and additions.

We consider direct matrix inversion of $\mathbf{A}$ via Cholesky decomposition (i.e., $\mathbf{A} = \mathbf{M}\mathbf{M}^H$, where $\mathbf{M}$ is lower triangular, as is $\mathbf{M}^{-1}$). The procedure is described in [159], but fewer flops are required if one keeps track of when squared magnitudes vs. general complex multiplications are calculated, and when division is by a real number. It can be found that (a) the Cholesky decomposition $\mathbf{A} = \mathbf{M}\mathbf{M}^H$ requires $\frac{4}{3}K^3 - K^2 + \frac{2}{3}K + \mathcal{O}(K) - 1$ flops (where $\mathcal{O}(K)$ comes from K square roots);

(b) finding $\mathbf{M}^{-1}$ by forward substitution requires $\frac{4}{3}K^3-\frac{1}{3}K$ flops; and (c) obtaining $\mathbf{A}^{-1} = (\mathbf{M}^{-1})^H\mathbf{M}^{-1}$ requires $\frac{4}{3}K^3+K^2+\frac{2}{3}K$ flops. Therefore, in total, direct inversion of $\mathbf{A}$ requires $4K^3+K+\mathcal{O}(K)-1$ flops.

The JC, GS, and JOR methods all calculate $\mathbf{x}_{n+1} = \mathbf{P}\mathbf{x}_n + \mathbf{q}$, which ordinarily requires $8K^2$ flops [159]. However, for JC the diagonal elements of $\mathbf{P}$ are all zero, as are the first column's elements for GS. This reduces the complexity per iteration for those two methods to $8K^2-8K$ flops. JC, GS, and JOR are distinguished more in how they initialize $\mathbf{P}$ and $\mathbf{q}$. Initializing JC is equivalent to solving $\mathbf{D}[\mathbf{P},\mathbf{q}] = [-(\mathbf{L}+\mathbf{U}),\mathbf{s}]$, which requires simply $2K^2$ flops since $\mathbf{D}$ is diagonal. Initializing GS means solving $(\mathbf{D}+\mathbf{L})[\mathbf{P},\mathbf{q}] = [-\mathbf{U},\mathbf{s}]$ by forward substitution. Following [159], this results in a total of $4K^3-3K^2+K$ flops required. For JOR, when calculating $\mathbf{I}_K-\omega\mathbf{D}^{-1}\mathbf{A}$, it takes only 1 flop to find and set all K diagonal elements of $\mathbf{P}$ equal to the resulting value of $1-\omega$. In total, initialization of JOR requires $2K^2+K+1$ flops[7].

In each iteration of the HP method, from (4.19), the needed steps are: (a) Find $\mathbf{E}_n = \mathbf{I}_K - \mathbf{A}\mathbf{X}_n$, which takes $8K^3 - 2K^2 + K$ flops; (b) add $\mathbf{I}_K$ and multiply by $\mathbf{E}_n$ a total of $r-2$ times each, for $(r-2)(8K^3 - 2K^2 + K)$ flops; (c) multiply by $\mathbf{X}_n$, using a final $8K^3-2K^2$ flops. Thus, the total complexity of an HP iteration is $r(8K^3 - 2K^2 + K)$ flops. For factorized HP with $r=15$, steps (a) and (c) above are the same. However, following (4.36), step (b) is replaced by calculating several matrix polynomials using a total of $32K^3 + 48K^2$ flops. Thus, overall, the factorized HP method uses $48K^3 + 44K^2 + K$ flops per iteration. To initialize the HP method, one needs either α for (4.21) or β and ϕ for (4.24); those in turn first need $\lambda_1(\mathbf{A})$ and $\lambda_k(\mathbf{A})$ from the bounds in (4.27) and (4.28) after finding m and s from (4.29) and (4.30). Finding $\lambda_1(\mathbf{A})$ and $\lambda_k(\mathbf{A})$ together requires $4K^2 + K + 6 + \mathcal{O}(1)$ flops. Afterwards, calculating α and (4.21) takes $K^2 + 4$ more flops, whereas calculating β, ϕ, and (4.24) takes $K^2 + K + 9$ more flops.

[7]This does not account for the complexity of first finding a suitable value of ω, which is roughly the same complexity as finding α for the HP method.

Table 4.2: Computational Complexity for Matrix Inversion and Pseudo-inversion Methods

Method	**Complexity**	
Direct Inversion	$4K^3+K+\mathcal{O}(K)-1$ flops $\left(\text{Multiplications } (\times)\text{: } 2K^3{+}2K^2{-}K, \text{Additions } (+)\text{: } 2K^3{-}2K^2{+}2K-1,\right.$ $\left.K \text{ square root operations}\right)$	
Iterative Inversion	Initialization	Per iteration
JC	$2K^2$ flops $\left(\times\text{: } 2K^2, +\text{: } 0\right)$	$8K^2-8K$ flops $\left(\times\text{: } 4K^2{-}4K, +\text{: } 4K^2{-}4K\right)$
GS	$4K^3-3K^2+K$ flops $\left(\times\text{: } 2K^3, +\text{: } 2K^3{-}3K^2{+}K\right)$	$8K^2-8K$ flops $\left(\times\text{: } 4K^2{-}4K, +\text{: } 4K^2{-}4K\right)$
JOR	$2K^2+K+1$ flops $\left(\times\text{: } 2K^2{+}K, +\text{: } 1\right)$	$8K^2$ flops $\left(\times\text{: } 4K^2, +\text{: } 4K^2\right)$
HP	$5K^2{+}K{+}10{+}\mathcal{O}(1)$ flops $\begin{pmatrix}\times\text{: } 3K^2{+}8,\\ +\text{: } 2K^2{+}K{+}2,\\ 2 \text{ square roots}\end{pmatrix}$ (4.21); $5K^2{+}2K{+}15{+}\mathcal{O}(1)$ flops $\begin{pmatrix}\times\text{: } 3K^2{+}11,\\ +\text{: } 2K^2{+}2K{+}4,\\ 2 \text{ square roots}\end{pmatrix}$ (4.24)	$r(8K^3{-}2K^2{+}K)$ flops $\begin{pmatrix}\times\text{: } 4rK^3,\\ +\text{: } r(4K^3{-}2K^2{+}K)\end{pmatrix}$
Factorized HP (r=15)	Same as for HP	$48K^3{+}44K^2{+}K$ flops $\begin{pmatrix}\times\text{: } 24K^3{+}26K^2,\\ +\text{: } 24K^3{+}18K^2{+}K\end{pmatrix}$
Iterative Pseudoinverse	Initialization	Per iteration
HP	$6KM$ flops (4.34) $\begin{pmatrix}\times\text{: } 4KM{+}1,\\ +\text{: } 2KM{-}1\end{pmatrix}$	$16K^2M{-}2KM{-}\ 16K^3{+}2K^2{+}$ $r(8K^3{-}2K^2{+}K)$ flops $\begin{pmatrix}\times\text{: } 8K^2M{-}8K^3{+}r(4K^3),\\ +\text{: } 8K^2M{-}2KM{-}\\ 8K^3{+}2K^2{+}\\ r(4K^3{-}2K^2{+}K)\end{pmatrix}$
Factorized HP (r=15)	Same as for HP	$16K^2M{-}2KM{+}32K^3{+}46K^2{+}K$ flops $\begin{pmatrix}\times\text{: } 8K^2M{+}16K^3{+}26K^2,\\ +\text{: } 8K^2M{-}2KM{+}\\ 16K^3{+}20K^2{+}K\end{pmatrix}$

The HP pseudoinverse method is quite similar to that for the inverse. The key difference is in the first and last step of each iteration. In calculating the error matrix in step (a), there is a product of a $K \times M$ matrix times an $M \times K$ matrix (rather than two $K \times K$ matrices), which requires $8K^2M - 2K^2$ flops. Similarly, in step (c) to calculate $\hat{\mathbf{X}}_{n+1}$, there is a an $M \times K$ matrix times a $K \times K$ matrix, using $8K^2M - 2KM$ flops. The error matrix is still $K \times K$, so the complexity of step (b) is unaffected. Consequently, the total complexity of the HP method becomes $16K^2M - 2KM - 16K^3 + 2K^2 + r(8K^3 - 2K^2 + K)$, and the total complexity of the factorized HP method with $r = 15$ becomes $16K^2M - 2KM + 32K^3 + 46K^2 + K$. However, it should be noted that $\mathbf{A}$ no longer needs to be calculated if $\alpha = 2/\mathrm{tr}(\mathbf{G}\mathbf{G}^H)$ is used. In this case, $6KM$ flops are required to initialize $\hat{\mathbf{X}}_0$ in (4.34).

4.5 Simulation Results

In this section, we evaluate the performance of the iterative matrix inversion methods for ZF precoding in a CF mMIMO system by examining the uncoded BER they achieve. We consider the partially-distributed scenario with $N = 4$ from before. 64-QAM modulation is used to transmit data symbols. Perfect knowledge of the channel matrices is assumed at both the transmitters and receivers, where the latter are assumed to use a matched filter detector.

Fig. 4.7 shows the BER vs. the total transmit SNR[8] P_t for ZF precoding comparing direct matrix inversion, the HP-based inverse with two different initialization points, and the HP-based pseudoinverse; two different values of r are considered. The BER achieved using direct matrix inversion serves as a lower bound and benchmark for the performance of the other methods. As expected, for $r = 3$ the BER of the HP-based inverse with $\mathbf{X}_0$ given by (4.24) closely follows that of direct matrix inversion, while the same method with $\mathbf{X}_0$ given by (4.21) displays an increasing gap at higher

[8]Since the total system power P_t in (4.2) is normalized to the noise power, it also equals the total transmit SNR.

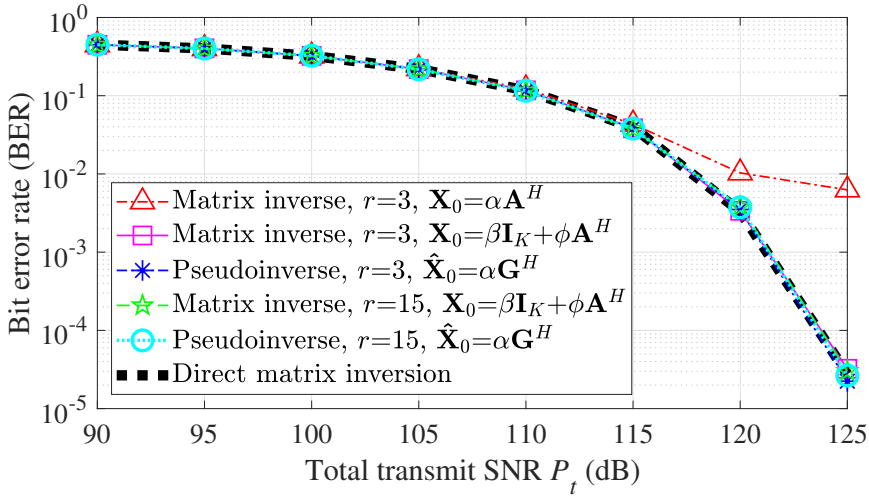

Figure 4.7: BER vs. total transmit SNR, comparing ZF precoding performed using HP-based matrix inverse and pseudoinverse methods, for a CF mMIMO system with 32 4-antenna APs serving 16 users. BER achieved using direct matrix inversion also shown as a lower bound benchmark.

transmit power. This demonstrates that in order for the HP method with $\mathbf{X}_0 = \alpha\mathbf{A}^H$ to perform acceptably, it must execute more than 20 iterations, which emphasizes the importance of the initialization point on both performance and reducing the computational complexity. Furthermore, although the HP method with $r = 15$ yields a similar performance, this result does not capture the effect of r on complexity; we will examine this next. Finally, the pseudoinverse with both values of r also closely follows ZF precoding with direct matrix inversion, which is desirable.

Fig. 4.8 shows the convergence of the HP-based matrix inverse and pseudoinverse methods with ZF precoding in terms of the BER they provide after calculating for n iterations. The BER achieved by direct matrix inversion again provides a lower bound on the performance. For the HP matrix inverse, we only consider the initialization point of (4.24) here due to its much better performance; $\hat{\mathbf{X}}_0 = \alpha\mathbf{G}^H$ is used again for the pseudoinverse. Naturally, with more iterations, the performance of all the cases improves, approaching the best possible BER provided by direct matrix inversion. However, for a given value of r, the inverse outperforms the pseudoinverse in terms of convergence. The HP method with $r = 15$ obtains the same BER as direct inversion in about 6–7 iterations. In comparison, the pseudoinverse with $r = 15$ achieves that

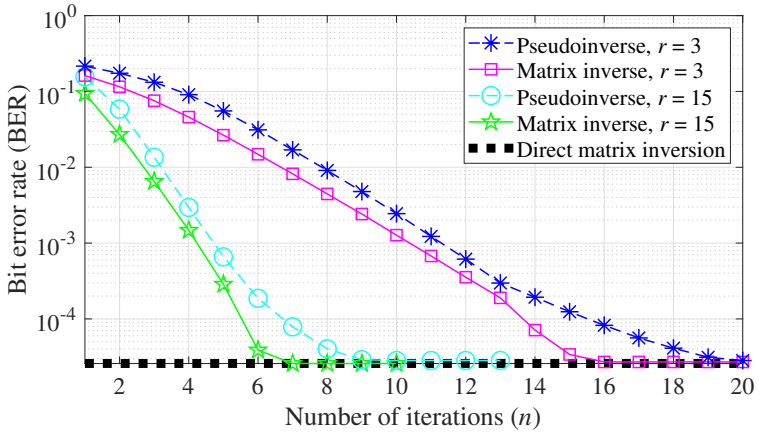

Figure 4.8: Convergence comparison of HP-based matrix inverse and pseudoinverse methods with ZF precoding in terms of BER vs. number of iterations n for two values of r; $P_t = 125$ dB, $L = 32$, $N = 4$, $K = 16$. BER achieved using direct matrix inversion also shown as a lower bound.

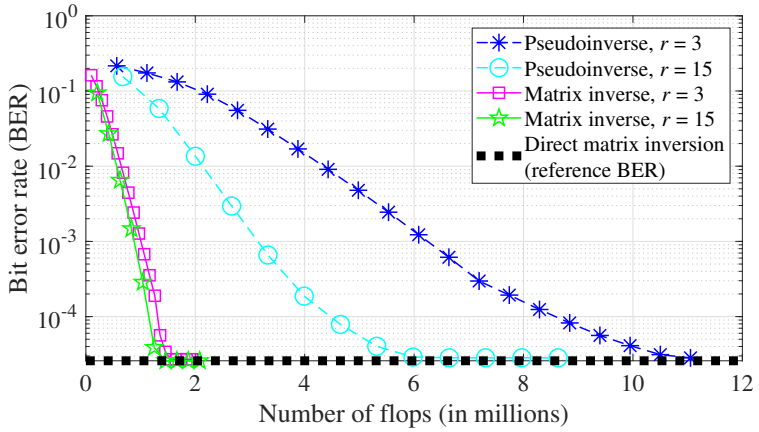

Figure 4.9: Convergence comparison of HP-based matrix inverse and pseudoinverse methods with ZF precoding in terms of BER vs. number of flops for two values of r; $P_t = 125$ dB, $L = 32$, $N = 4$, $K = 16$. BER achieved using direct matrix inversion also shown as a lower bound.

BER in about 8–10 iterations, whereas with $r = 3$, the inverse requires about 16 iterations and the pseudoinverse about 20 iterations. We also have investigated these methods at the lower SNR of 110 dB, and found that they all converge in about 2–3 iterations to a BER of about 0.12, so we do not depict those detailed results here.

Although Fig. 4.8 shows the comparative convergence of the BER of the methods, it does not indicate the complexity required to achieve that convergence. Therefore, in Fig. 4.9, we show BER vs. flops for the various methods[9]. While the inverse with $r = 15$ still performs the best, the figure shows the inverse with $r = 3$ is a close second in terms of the BER obtained for a given amount of computational effort. The $r = 3$ method spreads that effort over more iterations than the factorized method with $r = 15$.

4.6 Summary

In this chapter, we have examined several iterative methods to calculate the precoding matrix in a CF mMIMO system. We have investigated their computational complexity and convergence rate in the presence of small- and large-scale fading and spatial correlation between antennas. We have demonstrated that some iterative methods previously proposed for conventional mMIMO do not always converge for CF mMIMO. Since the performance and convergence of the HP method depends on initialization point, we have examined lower-complexity sub-optimal initialization points and have demonstrated that their performance is close to the optimal one. Simulation results have shown a factorized version of the HP method achieves the ZF performance of direct matrix inversion with few iterations, while the factorization helps reduce its computational complexity. We have also briefly examined the iterative methods in scalable CF mMIMO systems, and have found they converge somewhat slower, but can operate with greater parallelization on several smaller-sized matrices.

[9]In principle, direct matrix inversion should be a single point plotted in Fig. 4.9, since it is not iterative. We instead plot a "reference BER" line for direct matrix inversion to aid in visualizing its BER relative to the other methods.

Chapter 5

Symbiotic Backscatter Communication Underlying a Cell-Free Massive MIMO System

To reap the benefits of both CF mMIMO and SR, in this chapter, we consider a primary CF mMIMO system where the APs aid an underlaid BD layer to harvest energy and reflect information toward the primary receivers (which receive data from both layers). Most existing work (e.g., [61, 62, 160–163]) has considered SR in a cellular network with a single primary transmitter. While the authors of [164] have investigated the combination of CF mMIMO and SR, they assumed only one BD and one user. To the best of our knowledge, there has not yet been a full consideration of the coexistence of CF mMIMO and SR where multiple users and BDs are served. In this work, a two-phase UL pilot training method is proposed to acquire separate CSI of the direct and backscattered channels at the APs, with the effects of pilot contamination and spatial correlation between each AP's antennas accounted for. We then derive expressions for the average SINRs of both primary and backscatter signals, accounting for the effects of imperfect CSI, spatial correlation, pilot contamination, and channel hardening. Furthermore, the average power harvested in the BDs is derived.

5.1 System and Channel Models

5.1.1 System Model

We consider the DL of a symbiotic CF mMIMO system as illustrated in Fig. 5.1. N geographically-distributed APs, each equipped with L antennas, cooperatively serve K pieces of single-antenna UE equipment (UE). These UEs act as receivers for both the primary and AmBC data signals. We assume all APs are connected to a CPU via a perfect fronthaul network. Simultaneously, the APs support the secondary communication of K single-antenna BDs, with each UE paired with a different nearby BD. Each BD consists of a backscatter transmitter (e.g., a switched load impedance) and signal processor, a microcontroller, memory, and a rechargeable battery replenished by an energy harvester [61]. BD t_k, where $k = 1, \ldots, K$, aims to transmit information to UE u_k by changing its antenna impedance, thereby exploiting the ambient RF signal from the APs as both an energy source and a signal carrier.

There are two typical schemes to realize energy harvesting in AmBC: time-splitting (TS) and power-splitting (PS). In a TS scheme, the BD switches between harvesting energy and backscattering information in the time domain. In contrast, in a PS scheme, the BD splits the received RF signals into two power streams in the power domain, one for energy harvesting and the other for backscattering. Although the PS scheme requires a more complex transceiver in the BD than TS, since the legacy signal is used for both harvesting energy and reflecting information, PS is more efficient in its energy use. In addition, the PS scheme is a better candidate for delay-sensitive applications [165] since no time needs to be spent waiting for the BD to charge between transmissions. Because of these reasons, in this chapter, we consider a PS scheme.

We denote the UL channel between AP n and UE k as $\mathbf{g}_{b_n u_k} \in \mathbb{C}^{L\times 1}$, between AP n and BD t_k as $\mathbf{g}_{b_n t_k} \in \mathbb{C}^{L\times 1}$, and between BD t_k and UE k' as $g_{t_k u_{k'}}$. All the channels (except $g_{t_k u_k}$, see below) are assumed to undergo quasi-static block fading such that

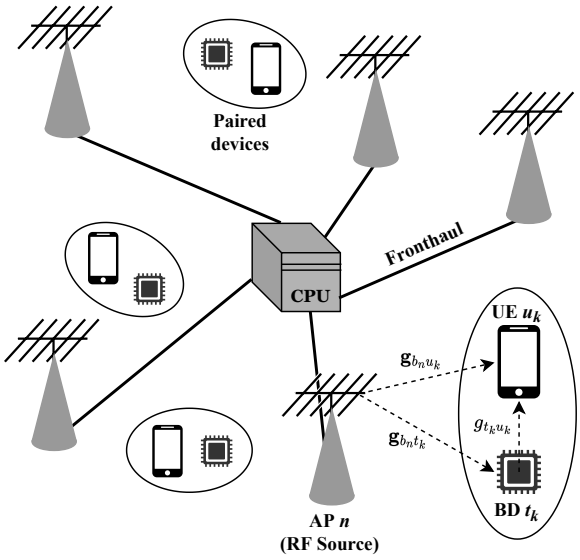

Figure 5.1: System layout of symbiotic CF mMIMO system

they remain constant during an (AP) transmission interval and only change between transmissions.

The block-fading channel coefficient vector $\mathbf{g}_{xy}$ between node x and receiver y is given by

$$\mathbf{g}_{xy} = \sqrt{\beta_{xy}}\mathbf{h}_{xy}. \tag{5.1}$$

β_{xy} is the large-scale fading coefficient which accounts for path loss and shadowing effects, whereas $\mathbf{h}_{xy}$ denotes the small-scale fading coefficients. We assume the channels undergo spatially-correlated Rayleigh fading. For UL channels from a BD or UE to an AP, $\mathbf{h}_{xy} \in \mathbb{C}^{L\times 1}$ is distributed $\sim \mathcal{CN}(0, \mathbf{R}_{\mathbf{h}})$, where $\mathbf{R}_{\mathbf{h}}$ is the covariance matrix. The covariance matrix of $\mathbf{g}_{xy}$ would therefore be $\mathbf{R}_{xy} = \beta_{xy}\mathbf{R}_{\mathbf{h}}$. For the UL channel between BD t_x and UE y, $\mathbf{h}_{t_x u_y}$ becomes a scalar $h_{t_x u_y} \sim \mathcal{CN}(0, 1)$. The exceptions to this are for every paired UE k and BD t_k; due to their proximity, their channel $g_{t_k u_k} \in \mathbb{C}$ is assumed to consist of only a line-of-sight component with no significant scattering, making it a constant[1] [62]. One typical application example for this scenario is a smartphone that simultaneously receives data from both a cel-

[1]An equivalent assumption is that although the UE and BD may move, their distance relative to each other remains approximately the same, again making $g_{t_k u_k}$ approximately constant over very large intervals of time.

lular network and a wearable sensor (e.g., a medical sensor or fitness tracker). The large-scale fading coefficients change much slower than small-scale ones, therefore we assume the APs know the large-scale coefficients perfectly.

5.1.2 Pilot Assignment and Channel Estimation

In this chapter, we assume that the CF mMIMO system uses TDD transmission mode. Thus, it can be assumed that UL/DL radio channel reciprocity holds, and the DL radio channels are the same as the UL radio channels. Accurate estimation of these channels at the APs is necessary to fully benefit from mMIMO; the channels are estimated via pilot signals sent from the UEs. Unfortunately, there may be insufficient number of orthogonal pilot sequences to assign a unique one to every UE in the system. This leads to errors in channel estimation known as pilot contamination. The topics of pilot assignment and contamination are largely outside the scope of this work. We employ the relatively simple scheme described in [34, Ch. 4.4] to assign pilots and determine which APs serve which UEs. The scheme mitigates pilot contamination by ensuring UEs that share pilot sequences are distant from each other, and any given AP only serves one of the UEs out of however many share that sequence.

With pilots assigned, the UL channels can be estimated. However, we need to consider that, in general, a symbiotic CF mMIMO system needs estimates of not only the direct-link channels $\mathbf{g}_{b_n u_k}$, but also of the backscatter channels $\mathbf{g}_{b_n t_k}$ and $g_{t_k u_k}$. To this end, we follow a similar approach as in [62] and utilize a two-phase channel estimation scheme for our system. In the first phase, UEs send pilot symbols while the BDs are in mute/non-reflection mode, so the signals received by the APs include only the effect of direct-link channels. In the second phase, UEs send more pilot signals, but this time the BDs also reflect the pilot symbols. So, in this phase the signals received at APs include a component from the direct-link channels together with a component from the cascaded backscatter channels $\mathbf{g}_{b_n t_k u_k}$ from UE k to BD t_k then to AP n. Hence, pilot signals received during the first phase are used to

estimate the direct-link channels, whereas those estimates together with the pilot signals received in the second phase are used to estimate the cascaded[2] backscatter channels.

Direct-Link Channel Estimation

In the first phase, all UEs simultaneously and synchronously transmit their pilot sequences, which are received by all APs. However, each AP only estimates the channels for the UE-BD pairs it serves. Let $\boldsymbol{\psi}_{k,1} \in \mathbb{C}^{\tau_1 \times 1}$ be the pilot sequence sent by UE k, with length τ_1 and $||\boldsymbol{\psi}_{k,1}||^2 = \tau_1, \forall k$. The received pilot signal $\mathbf{Y}_n \in \mathbb{C}^{L \times \tau_1}$ at AP n is [34]

$$\mathbf{Y}_n = \sum_{k=1}^{K} \sqrt{\rho_{k,1}}\, \mathbf{g}_{b_n u_k} \boldsymbol{\psi}_{k,1}^T + \mathbf{N}_n, \tag{5.2}$$

where $\rho_{k,1}$ is the pilot transmit power for UE k and $\mathbf{N}_n \in \mathbb{C}^{L \times \tau_1}$ is an additive noise matrix, whose elements are independent and identically distributed (i.i.d.) $\sim \mathcal{CN}(0, \sigma_n^2)$.

To estimate the direct-link channel $\mathbf{g}_{b_n u_k}$ of UE k, AP n correlates $\mathbf{Y}_n$ with the pilot sequence $\boldsymbol{\psi}_{k,1}$, which cancels the interference from all other pilot sequences. Let $\mathcal{S}_k$ denote the set of all UEs sharing the same pilot sequence as UE k (including k). Then, the correlated pilot signal $\mathbf{y}_{nk} \in \mathbb{C}^{L \times 1}$ can be written as [34]

$$\mathbf{y}_{nk} = \mathbf{Y}_n \frac{\boldsymbol{\psi}_{k,1}^*}{\sqrt{\tau_1}} = \sum_{k' \in \mathcal{S}_k} \sqrt{\rho_{k',1} \tau_1}\, \mathbf{g}_{b_n u_{k'}} + \mathbf{n}_{nk}, \tag{5.3}$$

where $\mathbf{n}_{nk} \sim \mathcal{CN}(0, \sigma_n^2 \mathbf{I}_L)$.

Then, the minimum mean square error (MMSE) estimate of $\mathbf{g}_{b_n u_k}$ can be calculated as [34]

$$\hat{\mathbf{g}}_{b_n u_k} = \sqrt{\rho_{k,1} \tau_1}\, \mathbf{R}_{b_n u_k} \boldsymbol{\Theta}_{nk}^{-1} \mathbf{y}_{nk}, \tag{5.4}$$

where

$$\boldsymbol{\Theta}_{nk} = \sum_{k' \in \mathcal{S}_k} \rho_{k',1} \tau_1 \mathbf{R}_{b_n u_{k'}} + \sigma_n^2 \mathbf{I}_L \tag{5.5}$$

[2]It is sufficient for our purposes to just estimate the cascaded channel $\mathbf{g}_{b_n t_k u_k}$ rather than requiring estimates of the individual channels $\mathbf{g}_{b_n t_k}$ and $g_{t_k u_k}$.

is the covariance matrix[3] of $\mathbf{y}_{nk}$, and $\mathbf{R}_{b_n u_{k'}}$ denotes the covariance matrix of $\mathbf{g}_{b_n u_{k'}}$.

Let $\tilde{\mathbf{g}}_{b_n u_k} = \mathbf{g}_{b_n u_k} - \hat{\mathbf{g}}_{b_n u_k}$ denote the channel estimation error. Based on a property of MMSE estimation, $\hat{\mathbf{g}}_{b_n u_k} \sim \mathcal{CN}(\mathbf{0}, \hat{\mathbf{R}}_{b_n u_k})$ and $\tilde{\mathbf{g}}_{b_n u_k} \sim \mathcal{CN}(\mathbf{0}, \tilde{\mathbf{R}}_{b_n u_k})$ are independent random variables, and their covariance matrices are respectively given by [34]

$$\hat{\mathbf{R}}_{b_n u_k} = \rho_{k,1} \tau_1 \mathbf{R}_{b_n u_k} \boldsymbol{\Theta}_{nk}^{-1} \mathbf{R}_{b_n u_k}, \tag{5.6}$$

$$\tilde{\mathbf{R}}_{b_n u_k} = \mathbf{R}_{b_n u_k} - \hat{\mathbf{R}}_{b_n u_k}. \tag{5.7}$$

Cascaded Backscatter Channel Estimation

In the second phase, every UE again transmits a pilot sequence; UE k transmits $\boldsymbol{\psi}_{k,2} \in \mathbb{C}^{\tau_2 \times 1}$ with length τ_2 and $||\boldsymbol{\psi}_{k,2}||^2 = \tau_2, \forall k$. (For the sake of generality, these do not necessarily have to be the same sequences as in the first phase.) The pilot signals propagate to the APs along both the direct-link channels and the cascaded backscatter channels from reflections off of the BDs. The received pilot signal $\mathbf{Y}'_n \in \mathbb{C}^{L \times \tau_2}$ at AP n therefore becomes

$$\mathbf{Y}'_n = \sum_{k=1}^{K} \sqrt{\rho_{k,2}}\, \mathbf{g}_{b_n u_k} \boldsymbol{\psi}_{k,2}^T + \sum_{k=1}^{K} \sqrt{\rho_{k,2}}\, \mathbf{g}_{b_n t_k} \sum_{k'=1}^{K} \sqrt{\Gamma_0}\, g_{t_k u_{k'}} \boldsymbol{\psi}_{k,2}^T + \mathbf{N}'_n, \tag{5.8}$$

where Γ_0 represents the signal power attenuation inside the BD due to imperfect reflections. Accounting for this attenuation, we specify the cascaded channel as $\mathbf{g}_{b_n t_k u'_k} = \mathbf{g}_{b_n t_k} \sqrt{\Gamma_0}\, g_{t_k u'_k}$.

Due to high penetration, diffraction, and distance-based power losses, caused by obstacles such as buildings and trees, signals reflected from faraway BDs are always significantly attenuated. As such, we henceforth assume for simplicity that the cascaded links between UE k and AP n via unassociated BDs $t_{k'}, k' \neq k$, are blocked[4] and provide a negligible contribution to the received signal. In other words, $\mathbf{g}_{b_n t_{k'} u_k} \approx 0$ for $k' \neq k$. Thus, under this assumption, $\mathbf{Y}'_n$ can be simplified as

$$\mathbf{Y}'_n = \sum_{k=1}^{K} \sqrt{\rho_{k,2} \tau_2}\, (\mathbf{g}_{b_n u_k} + \mathbf{g}_{b_n t_k u_k})\, \boldsymbol{\psi}_{k,2}^T + \mathbf{N}'_n. \tag{5.9}$$

[3] $\boldsymbol{\Theta}_{nk}$ can be obtained directly from measurements of $\mathbf{y}_{nk}$ without needing to know all the individual matrices $\mathbf{R}_{b_n u_{k'}}$.

[4] By extension, the channels between any two BDs are also blocked.

$\mathbf{Y}'_n$ can then be correlated with $\boldsymbol{\psi}_{k,2}$ like in (5.3) to obtain $\mathbf{y}'_{nk}$. Furthermore, since $\mathbf{g}_{b_n u_k} = \hat{\mathbf{g}}_{b_n u_k} + \tilde{\mathbf{g}}_{b_n u_k}$, AP n can subtract the contribution of channel estimate $\hat{\mathbf{g}}_{b_n u_k}$ for its served UE-BD pair k (obtained during the first phase) from $\mathbf{y}'_{nk}$. This leaves:

$$\mathbf{z}'_{nk} = \mathbf{Y}'_n \frac{\boldsymbol{\psi}^*_{k,2}}{\sqrt{\tau_2}} - \sqrt{\rho_{k,2}\tau_2}\,\hat{\mathbf{g}}_{b_n u_k} = \sqrt{\rho_{k,2}\tau_2}(\tilde{\mathbf{g}}_{b_n u_k} + \mathbf{g}_{b_n t_k u_k}) + \sum_{\ell \in \{\mathcal{S}_k \setminus k\}} \sqrt{\rho_{\ell,2}\tau_2}(\mathbf{g}_{b_n u_\ell} + \mathbf{g}_{b_n t_\ell u_\ell}) + \mathbf{n}'_{nk} \tag{5.10}$$

From $\mathbf{z}'_{nk}$, the MMSE estimate of cascaded backscatter channel $\mathbf{g}_{b_n t_k u_k}$ is

$$\hat{\mathbf{g}}_{b_n t_k u_k} = \sqrt{\rho_{k,2}\tau_2}\,\mathbf{R}_{b_n t_k u_k} \boldsymbol{\Phi}'^{\,-1}_{nk}\,\mathbf{z}'_{nk}, \tag{5.11}$$

where $\mathbf{R}_{b_n t_k u_k} = \mathbb{E}\{\mathbf{g}_{b_n t_k u_k}\mathbf{g}^H_{b_n t_k u_k}\} = \Gamma_0 |g_{t_k u_k}|^2\,\mathbf{R}_{b_n t_k}$ denotes the covariance matrix of $\mathbf{g}_{b_n t_k u_k}$ and $\boldsymbol{\Phi}'_{nk} = \mathbb{E}\{\mathbf{z}'_{nk}\mathbf{z}'^{\,H}_{nk}\}$ denotes the covariance matrix of $\mathbf{z}'_{nk}$. The latter is given by

$$\boldsymbol{\Phi}'_{nk} = \sigma_n^2 \mathbf{I}_L + \rho_{k,2}\tau_2(\tilde{\mathbf{R}}_{b_n u_k} + \mathbf{R}_{b_n t_k u_k}) + \sum_{\ell \in \{\mathcal{S}_k \setminus k\}} \rho_{\ell,2}\tau_2(\mathbf{R}_{b_n u_\ell} + \mathbf{R}_{b_n t_\ell u_\ell}) - \sum_{\ell \in \{\mathcal{S}_k \setminus k\}} \tau_1\tau_2\sqrt{\rho_{k,1}\rho_{k,2}\rho_{\ell,1}\rho_{\ell,2}} \begin{pmatrix} \mathbf{R}_{b_n u_k}\boldsymbol{\Theta}^{-1}_{nk}\mathbf{R}_{b_n u_\ell} + \\ \mathbf{R}_{b_n u_\ell}\boldsymbol{\Theta}^{-1}_{nk}\mathbf{R}_{b_n u_k} \end{pmatrix} \tag{5.12}$$

The last summation in (5.12) is a result of the (small) correlation between $\tilde{\mathbf{g}}_{b_n u_k}$ and $\mathbf{g}_{b_n u_\ell}, \ell \neq k$. For more details on the derivation, please refer to Appendix B.

Denoting $\tilde{\mathbf{g}}_{b_n t_k u_k} = \mathbf{g}_{b_n t_k u_k} - \hat{\mathbf{g}}_{b_n t_k u_k}$, it then results, similarly to (5.6) and (5.7), that $\hat{\mathbf{g}}_{b_n t_k u_k} \sim \mathcal{CN}(0, \hat{\mathbf{R}}_{b_n t_k u_k})$ and $\tilde{\mathbf{g}}_{b_n t_k u_k} \sim \mathcal{CN}(0, \tilde{\mathbf{R}}_{b_n t_k u_k})$ are independent with

$$\hat{\mathbf{R}}_{b_n t_k u_k} = \rho_{k,2}\tau_2 \mathbf{R}_{b_n t_k u_k} \boldsymbol{\Phi}'^{\,-1}_{nk} \mathbf{R}_{b_n t_k u_k}, \tag{5.13}$$

$$\tilde{\mathbf{R}}_{b_n t_k u_k} = \mathbf{R}_{b_n t_k u_k} - \hat{\mathbf{R}}_{b_n t_k u_k}. \tag{5.14}$$

5.1.3 Downlink Signal Model

While we assume CSI is acquired at the APs via UL pilot signals, the same is not true for the DL. Instead, we assume that no pilot signals are sent on the DL. As justified in [34, Remark 6.1], it is generally sufficient to only use pilots in the UL direction

[5]. This is especially true in a mMIMO system; due to its large number of antennas, the channels tend to undergo channel hardening [8, 34], such that the fluctuations in the channel gains around the mean become small. Unfortunately, it has been shown in [67] that the degree of channel hardening in CF mMIMO systems can be considerably smaller than in co-located mMIMO systems. Subsequently, the authors of [98] have proposed a variant of conjugate beamforming dubbed ENCB, in which the conjugate beamforming precoding vector (i.e., the conjugate of the channel gains) is normalized by the squared norm of the channel. This normalization enhances the effect of channel hardening, which improves the reliability of decoding data relying only on knowledge of the statistics of the CSI (or "statistical CSI" for short). ENCB also allows precoding calculations to easily be decentralized.

At the same time, in a symbiotic AmBC system, the achievable primary (legacy) and secondary (BD) data rates depend on the transmit beamforming vectors. Thus, the APs should design their beamforming vectors such that they factor in both UEs and BDs. While several works in the literature have investigated optimal beamforming designs, the authors of [62] have proven that the optimal beamforming vector lies in the subspace spanned by the normalized form of the channel vectors $\hat{\mathbf{g}}_{b_n u_k}$ and $\hat{\mathbf{g}}_{b_n t_k}$. In other words, the optimal beamforming vector $\mathbf{w}_{nk}$ at AP n for UE-BD pair k has the structure $\mathbf{w}_{nk} = \mu'_1 \frac{\hat{\mathbf{g}}_{b_n u_k}}{||\hat{\mathbf{g}}_{b_n u_k}||} + \mu'_2 \frac{\hat{\mathbf{g}}_{b_n t_k}}{||\hat{\mathbf{g}}_{b_n t_k}||}$, where the complex-valued weights μ'_1 and μ'_2 are subject to $|\mu'_1|^2 + |\mu'_2|^2 = 1$.

Combining the above, in this chapter, we use a beamforming vector that enhances channel hardening while lying in the optimal subspace. Our beamforming vector at AP n for UE-BD pair k is given by

$$\mathbf{w}_{nk} = \mu_{1,nk} \frac{\hat{\mathbf{g}}_{b_n u_k}}{||\hat{\mathbf{g}}_{b_n u_k}||^2} + \mu_{2,nk} \frac{\hat{\mathbf{g}}_{b_n t_k u_k}}{||\hat{\mathbf{g}}_{b_n t_k u_k}||^2} \tag{5.15}$$

such that $\left| \frac{\mu_{1,nk}}{||\hat{\mathbf{g}}_{b_n u_k}||} \right|^2 + \left| \frac{\mu_{2,nk}}{||\hat{\mathbf{g}}_{b_n t_k u_k}||} \right|^2 = 1$, for every pair k served by AP n. We note that

[5]Nevertheless, some training for DL CSI acquisition at the DL receiver can still be beneficial to counteract partial or imperfect CSI at the APs [34, 166].

our beamforming vector uses $\hat{\mathbf{g}}_{b_n t_k u_k}$ rather than $\hat{\mathbf{g}}_{b_n t_k}$. Since $g_{t_k u_k}$ is assumed to be a scalar constant, its magnitude will be normalized out. Additionally, if $g_{t_k u_k}$ has a complex phase, the effect of that phase will become incorporated into the value of μ_2. Thus, $\hat{\mathbf{g}}_{b_n t_k u_k}$ and $\hat{\mathbf{g}}_{b_n t_k}$ are equivalent from the perspective of the BD. Meanwhile, using $\hat{\mathbf{g}}_{b_n t_k u_k}$ allows primary data to be properly directed to the UE via the BD and eliminates the need to know $g_{t_k u_k}$ separately, which simplifies the channel estimation.

Hence, the overall signal sent by AP n can be written as

$$\mathbf{x}_n = \sum_{k=1}^{K} \sqrt{p_t \eta_{nk}} \left(\mu_{1,nk} \frac{\hat{\mathbf{g}}_{b_n u_k}}{||\hat{\mathbf{g}}_{b_n u_k}||^2} + \mu_{2,nk} \frac{\hat{\mathbf{g}}_{b_n t_k u_k}}{||\hat{\mathbf{g}}_{b_n t_k u_k}||^2} \right) s_k, \tag{5.16}$$

where p_t is the maximum transmit power of each AP, η_{nk} is the power coefficient (i.e., the fraction of its total power) used by AP n to transmit data to legacy UE k, and s_k is the data symbol intended for legacy UE k, with $\mathbb{E}\{|s_k|^2\} = 1$.

5.2 Derivation of SINRs and Harvested Power

In this section, we derive expressions for the SINR of transmissions from the APs and BDs, based on the channel estimates $\hat{\mathbf{g}}_{b_n u_k}$ and $\hat{\mathbf{g}}_{b_n t_k u_k}, \forall n, k$. From these, achievable data rates of the primary transmission and BER of secondary transmissions are given. We also derive the amount of power harvested within our SR network.

5.2.1 Achievable Data rates at the UEs

Besides the data signal transmitted from the APs, each BD t_k backscatters the ambient RF signals to convey its information symbols s_{t_k} intended for UE k. In this work, binary phase shift keying (BPSK) has been considered for the BDs, such that $s_{t_k} \in \{-1, 1\}$. Although it is possible to use higher-order signal constellations for the BD data symbols [167], we assume the simpler BPSK is used to decrease the implementation cost and complexity. Furthermore, as is typical in the literature (e.g., [56]), we assume there is no signal processing delay in the BD circuitry. The critical aspects of transmissions from a BD are as follows:

- For each data symbol, a BD tunes its antenna impedance to generate a different reflection coefficient which corresponds to the symbol. The relation between point c_i in the constellation $\mathcal{K}_c$ and the corresponding reflection coefficient Γ_i is

$$\Gamma_i = \sqrt{\Gamma_0}\,\frac{c_i}{\max\limits_{c_j \in \mathcal{K}_c} |c_j|}, \tag{5.17}$$

  where $0 < \Gamma_0 < 1$. In our case, with BPSK, the symbols ± 1 simply map to the reflection coefficients $\pm\sqrt{\Gamma_0}$.

- In practice, a BD backscatters its own information at a much lower data rate than that of the AP. Hence, we assume the symbol duration for a BD is M times that of an AP, with $M \gg 1$ [62, 160]. For $M = 1$ synchronization is required between s_k and s_{t_k} to avoid the so-called "spectrum growth" phenomenon, which is the increase in the signal's bandwidth caused by overlaying the BD transmission on top of the primary transmission [163, 168]. However, for large M, spectrum growth becomes negligible [163, 168].

If no primary signal is intended for UE k, BD t_k may still have data to send to UE k by backscattering AP signals. We assume in such cases that the UE, as part of its control signals, continues to transmit pilot signals that can still be used for channel estimation. Then, the APs can direct a beam towards BD t_k by using only $\hat{\mathbf{g}}_{b_n t_k u_k}$ to find $\mathbf{w}_{nk}$ and setting $\mu_{1,nk}$ to zero. The purpose at this point is just to supply BD t_k with power and a carrier wave; as such, the symbols sent by the AP using $\mathbf{w}_{nk}$ are rather meaningless and arbitrary. To avoid causing interference on other legacy UEs (albeit likely small, since the beam is not directed toward them), these symbols could be some combination of the intended data symbols for those other UEs.

We denote $\mathcal{U}_n$ as the set of UE-BD pairs served by AP n and $\mathcal{A}_k$ as the set of APs serving UE-BD pair k. Furthermore, let α_{t_k} denote the PS ratio for BD t_k, with $0 < \alpha_{t_k} < 1$. α_{t_k} represents the fraction of the harvested power at BD t_k that is allocated to its data transmission; the rest goes toward powering the circuitry of the

BD. Then, the signal received by UE k during a primary symbol interval (or $1/M$ of a BD symbol interval) is given by[6]

$$y_k = \sum_{n=1}^{N} \sum_{k' \in \mathcal{U}_n} \sqrt{p_t \eta_{nk'}} \mathbf{g}_{b_n u_k}^H \mathbf{w}_{nk'} s_{k'} + \sum_{n=1}^{N} \sum_{k'=1}^{K} \sum_{k'' \in \mathcal{U}_n} \sqrt{p_t \eta_{nk''} \alpha_{t_{k'}}} \mathbf{g}_{b_n t_{k'} u_{k''}}^H \mathbf{w}_{nk''} s_{k''} s_{t_{k'}} + n_k \tag{5.18}$$

that can be expanded as

$$\begin{aligned} y_k = & \underbrace{\sum_{n \in \mathcal{A}_k} \sqrt{p_t \eta_{nk}}\, \mathbf{g}_{b_n u_k}^H \mathbf{w}_{nk} s_k}_{S_1} + \underbrace{\sum_{n=1}^{N} \sum_{\substack{\ell \in \mathcal{U}_n, \\ \ell \neq k}} \sqrt{p_t \eta_{n\ell}}\, \mathbf{g}_{b_n u_k}^H \mathbf{w}_{n\ell} s_\ell}_{R_1} \\ & + \underbrace{\sum_{n \in \mathcal{A}_k} \sqrt{p_t \eta_{nk} \Gamma_0 \alpha_{t_k}}\, \mathbf{g}_{b_n t_k}^H \mathbf{w}_{nk} s_k g_{t_k u_k} s_{t_k}}_{S_2} + \underbrace{\sum_{n=1}^{N} \sum_{\substack{\ell \in \mathcal{U}_n, \\ \ell \neq k}} \sqrt{p_t \eta_{n\ell} \Gamma_0 \alpha_{t_k}}\, \mathbf{g}_{b_n t_k}^H \mathbf{w}_{n\ell} s_\ell g_{t_k u_k} s_{t_k}}_{R_2} \\ & + \underbrace{\sum_{n=1}^{N} \sum_{\substack{k'=1, \\ k' \neq k}}^{K} \sum_{k'' \in \mathcal{U}_n} \sqrt{p_t \eta_{nk''} \Gamma_0 \alpha_{t_{k'}}}\, \mathbf{g}_{b_n t_{k'}}^H \mathbf{w}_{nk''} s_{k''} g_{t_{k'} u_k} s_{t_{k'}} + n_k}_{X_2} \end{aligned} \tag{5.19}$$

where S_1 represents the signal intended for UE k from the APs received via direct-link channels, and R_1 represents multiuser interference from all APs received via direct-link channels. S_2 represents signals intended for UE k that are sent by or reflected from BD t_k; this contains a composite of data from the APs and data from t_k. R_2 represents multiuser interference from the APs reflected off of BD t_k to its paired UE k. Although this term represents interference for the primary transmission, it contains useful data for the BD transmission. X_2 represents signals received by UE k that have been reflected from or sent by other BDs $t_{k'}, k' \neq k$. This term contains both useful data and interference. However, as discussed earlier, we assume that channels from non-paired BDs are blocked. Consequently, X_2 may be neglected. Lastly, $n_k \sim \mathcal{CN}(0, \sigma_n^2)$ is additive white Gaussian noise. As can be seen, due to how

[6]In practice, under UL/DL radio channel reciprocity, if the UL channel vector is $\mathbf{g}$, the DL channel vector would be $\mathbf{g}^T$ instead of $\mathbf{g}^H$. Using $\mathbf{g}^H$ for the DL channel is a mathematical convenience to simplify the notation, and does not change the analysis or performance (see also [34, Ch. 2.3.4]).

AmBC shares spectrum, there exists interference between the primary and backscatter systems. This interference may become severe if UEs and BDs are densely distributed in a small area.

Because both the primary data signals and the signals reflected off the BDs originate from the CF mMIMO system, we assume there is additionally some sort of synchronization or other type of reference signal[7] sent along with the data that enables partially-coherent reception at the UE. That is, this reference signal is sufficient to detect and make use of the phase of the received data signals, but is insufficient for full instantaneous CSI at the UE. The UE instead only has statistical CSI available for decoding data signals. More specifically, we assume UE k has separate CSI estimates of the direct-link precoded effective channels $\mathbb{E}\{\hat{\mathbf{g}}_{b_n u_k}^H \mathbf{w}_{nk}\}$ and the cascased precoded effective channels $\mathbb{E}\{\hat{\mathbf{g}}_{b_n t_k u_k}^H \mathbf{w}_{nk}\}$ from its serving APs $\forall n \in \mathcal{A}_k$. These could be estimated over multiple intervals at the UE or fed from the APs to the UE occasionally, since they consist of only two complex-valued scalars per AP that change very slowly.

We denote $\hat{\mathbf{q}}_{b_n u_k} = \frac{\hat{\mathbf{g}}_{b_n u_k}}{||\hat{\mathbf{g}}_{b_n u_k}||^2}$ with covariance matrix $\hat{\mathbf{Q}}_{b_n u_k}$ and $\hat{\mathbf{q}}_{b_n t_k u_k} = \frac{\hat{\mathbf{g}}_{b_n t_k u_k}}{||\hat{\mathbf{g}}_{b_n t_k u_k}||^2}$ with covariance matrix $\hat{\mathbf{Q}}_{b_n t_k u_k}$. Since the symbol duration of s_{t_k} is M times larger than that of s_k, the backscatter link can be treated as a multipath component when decoding the primary signal [61]. Hence, the average[8] SINR of the primary transmission at UE k, as derived in Appendix B.2, may be calculated as given by

$$\mathrm{SINR}_k^{(1)} = \frac{p_t \sum\limits_{i \in \mathcal{A}_k} \sum\limits_{j \in \mathcal{A}_k} \sqrt{\eta_{ik}\eta_{jk}} (\mu_{1,ik}\mu_{1,jk}^* + \alpha_{t_k}\mu_{2,ik}\mu_{2,jk}^*)}{I_{\mathcal{A}_k} + \mathbb{E}\{|R_1|^2\} + \mathbb{E}\{|R_2|^2\} + \sigma_n^2}, \tag{5.20}$$

[7]Examples could include the demodulation reference signal (DM-RS) or phase tracking reference signals (PT-RS) included in 5th generation cellular systems [169].

[8]This is in contrast to some of the related literature such as [160, 163, 170], which instead consider the instantaneous SINR.

where

$$I_{\mathcal{A}_k} = \sum_{n\in\mathcal{A}_k} p_t\eta_{nk}\Bigg[|\mu_{1,nk}|^2\mathrm{tr}\big[\big(\tilde{\mathbf{R}}_{b_nu_k}+\alpha_{t_k}\mathbf{R}_{b_nt_ku_k}\big)\hat{\mathbf{Q}}_{b_nu_k}\big] + |\mu_{2,nk}|^2\Big(\mathbb{E}\{\tilde{\mathbf{g}}^H_{b_nu_k}\hat{\mathbf{q}}_{b_nt_ku_k}\hat{\mathbf{q}}^H_{b_nt_ku_k}\tilde{\mathbf{g}}_{b_nu_k}\}+\mathrm{tr}\big[\big(\hat{\mathbf{R}}_{b_nu_k}+\alpha_{t_k}\tilde{\mathbf{R}}_{b_nt_ku_k}\big)\hat{\mathbf{Q}}_{b_nt_ku_k}\big]\Big)\Bigg] + \sum_{i\in\mathcal{A}_k}\sum_{\substack{j\in\mathcal{A}_k,\\ j\neq i}} p_t\sqrt{\eta_{ik}\eta_{jk}}\,\mu_{2,ik}\,\mu^*_{2,jk}\,\mathbb{E}\{\tilde{\mathbf{g}}^H_{b_iu_k}\hat{\mathbf{q}}_{b_it_ku_k}\}\mathbb{E}\{\hat{\mathbf{q}}^H_{b_jt_ku_k}\tilde{\mathbf{g}}_{b_ju_k}\} \tag{5.21}$$

$$\mathbb{E}\{|R_1|^2\}=\sum_{n=1}^{N}\sum_{\substack{\ell\in\mathcal{U}_n,\\ \ell\neq k}} p_t\eta_{n\ell}\times\begin{cases}|\mu_{1,n\ell}|^2\mathrm{tr}(\mathbf{R}_{b_nu_k}\hat{\mathbf{Q}}_{b_nu_\ell})+|\mu_{2,n\ell}|^2\mathrm{tr}(\mathbf{R}_{b_nu_k}\hat{\mathbf{Q}}_{b_nt_\ell u_\ell}), & \text{if } k\notin\mathcal{S}_\ell,\\ |\mu_{1,n\ell}|^2\,\mathbb{E}\{\mathbf{g}^H_{b_nu_k}\hat{\mathbf{q}}_{b_nu_\ell}\hat{\mathbf{q}}^H_{b_nu_\ell}\mathbf{g}_{b_nu_k}\} & \\ \quad+|\mu_{2,n\ell}|^2\,\mathbb{E}\{\mathbf{g}^H_{b_nu_k}\hat{\mathbf{q}}_{b_nt_\ell u_\ell}\hat{\mathbf{q}}^H_{b_nt_\ell u_\ell}\mathbf{g}_{b_nu_k}\} & \text{if } k\in\mathcal{S}_\ell\\ \quad+2\,\mathfrak{Re}\Big\{\mu_{1,n\ell}\,\mu^*_{2,n\ell}\,\mathbb{E}\{\mathbf{g}^H_{b_nu_k}\hat{\mathbf{q}}_{b_nu_\ell}\hat{\mathbf{q}}^H_{b_nt_\ell u_\ell}\mathbf{g}_{b_nu_k}\}\Big\}, & \end{cases}$$

$$+\sum_{i=1}^{N}\sum_{\substack{j=1,\\ j\neq i}}^{N}\sum_{\substack{\ell\in\mathcal{U}_i\cap\mathcal{U}_j,\\ \ell\neq k}} p_t\sqrt{\eta_{i\ell}\eta_{j\ell}}\times\begin{cases}0, & \text{if } k\notin\mathcal{S}_\ell,\\ \mu_{1,i\ell}\,\mu^*_{1,j\ell}\,\mathbb{E}\{\mathbf{g}^H_{b_iu_k}\hat{\mathbf{q}}_{b_iu_\ell}\}\mathbb{E}\{\hat{\mathbf{q}}^H_{b_ju_\ell}\mathbf{g}_{b_ju_k}\} & \\ \quad+\mu_{2,i\ell}\,\mu^*_{2,j\ell}\,\mathbb{E}\{\mathbf{g}^H_{b_iu_k}\hat{\mathbf{q}}_{b_it_\ell u_\ell}\}\mathbb{E}\{\hat{\mathbf{q}}^H_{b_jt_\ell u_\ell}\mathbf{g}_{b_ju_k}\} & \text{if } k\in\mathcal{S}_\ell\\ \quad+2\,\mathfrak{Re}\Big\{\mu_{1,i\ell}\,\mu^*_{2,j\ell}\,\mathbb{E}\{\mathbf{g}^H_{b_iu_k}\hat{\mathbf{q}}_{b_iu_\ell}\}\mathbb{E}\{\hat{\mathbf{q}}^H_{b_jt_\ell u_\ell}\mathbf{g}_{b_ju_k}\}\Big\}, & \end{cases} \tag{5.22}$$

$$\mathbb{E}\{|R_2|^2\} = \sum_{n=1}^{N}\sum_{\substack{\ell\in\mathcal{U}_n,\\ \ell\neq k}} p_t\alpha_{t_k}\eta_{n\ell}\Bigg(|\mu_{1,n\ell}|^2\mathrm{tr}(\mathbf{R}_{b_nt_ku_k}\hat{\mathbf{Q}}_{b_nu_\ell}) + |\mu_{2,n\ell}|^2\times\begin{cases}\mathrm{tr}(\mathbf{R}_{b_nt_ku_k}\hat{\mathbf{Q}}_{b_nt_\ell u_\ell}), & \text{if } \ell\notin\mathcal{S}_k,\\ \mathbb{E}\{\mathbf{g}^H_{b_nt_ku_k}\hat{\mathbf{q}}_{b_nt_\ell u_\ell}\hat{\mathbf{q}}^H_{b_nt_\ell u_\ell}\mathbf{g}_{b_nt_ku_k}\}, & \text{if } \ell\in\mathcal{S}_k,\end{cases}\Bigg)$$

$$+\sum_{i=1}^{N}\sum_{\substack{j=1,\\ j\neq i}}^{N}\sum_{\substack{\ell\in\mathcal{U}_i\cap\mathcal{U}_j,\\ \ell\neq k}} p_t\alpha_{t_k}\sqrt{\eta_{i\ell}\eta_{j\ell}}\times\begin{cases}0, & \text{if } \ell\notin\mathcal{S}_k,\\ \mu_{2,i\ell}\mu^*_{2,j\ell}\,\mathbb{E}\{\mathbf{g}^H_{b_it_ku_k}\hat{\mathbf{q}}_{b_it_\ell u_\ell}\}\mathbb{E}\{\hat{\mathbf{q}}^H_{b_jt_\ell u_\ell}\mathbf{g}_{b_jt_ku_k}\}, & \text{if } \ell\in\mathcal{S}_k\end{cases}$$

With the assumption of partially-coherent reception, the average achievable primary data rate for UE k is

$$R_k^{(1)} = B_1\log_2\Big(1+\mathrm{SINR}_k^{(1)}\Big), \tag{5.23}$$

where B_1 is the bandwidth of the primary transmission.

Due to the double-fading effect over the two channels $\mathbf{g}_{b_nt_k}$ and $g_{t_ku_k}$, along with the PS ratio α_{t_k} and attenuation Γ_0, in almost all cases the signal strength received from the BD will be much lower than that from the APs. Thus, in this chapter , we perform successive interference cancellation (SIC) at the UEs to remove the primary signal from the received signal before decoding the BD signal [56]. However, since

only statistical CSI is known at the UEs, they can only remove a portion of the primary signal using average values. The remaining signal is consequently

$$y_k^{\mathrm{SIC}} = \sum_{n=1}^{N} \sum_{k' \in \mathcal{U}_n} \sqrt{p_t \eta_{nk'} \alpha_{t_k}}\, \mathbf{g}_{b_n t_k u_k}^H \mathbf{w}_{nk'} s_{k'} \;\; s_{t_k} \tag{5.24}$$
$$\underbrace{+ \sum_{n \in \mathcal{A}_k} \sqrt{p_t \eta_{nk}} \left(\mathbf{g}_{b_n u_k}^H \mathbf{w}_{nk} - \mathbb{E}\left\{ \hat{\mathbf{g}}_{b_n u_k}^H \mathbf{w}_{nk} \right\} \right) s_k + \sum_{n=1}^{N} \sum_{\substack{\ell \in \mathcal{U}_n, \\ \ell \neq k}} \sqrt{p_t \eta_{n\ell}}\, \mathbf{g}_{b_n u_k}^H \mathbf{w}_{n\ell} s_\ell + n_k}_{y_{\mathrm{I+N}}\text{: interference + noise}}$$

SIC with statistical CSI removes most of S_1 in (5.19), but still leaves some residual direct-link interference from serving APs. R_1 in (5.19) also constitutes unremoved interference for the BD transmission. The useful signal components for the BD transmission are S_2 and R_2 in (5.19). Unfortunately, statistical CSI is only available for S_2, but since R_2 can also constitute a significant contribution to the power, the partial statistical CSI is not as useful in this case. Without statistical CSI of the combined S_2+R_2 (in particular its magnitude), under the assumption of partially-coherent reception, the best the UEs can do is equal gain combining (EGC) [171, Ch. 6.4] of the BD transmissions across M primary symbol intervals.

The effective precoded channel for the BD transmission in primary interval m is $g_{\mathrm{BD}}(m) = \sum_{n=1}^{N} \sum_{k' \in \mathcal{U}_n(m)} \sqrt{p_t \eta_{nk'}(m) \alpha_{t_k}(m)}\, \mathbf{g}_{b_n t_k u_k}^H(m) \mathbf{w}_{nk'}(m) s_{k'}(m)$, where we note that multiple transmission parameters could potentially change between primary intervals. After cancelling the phase of $g_{\mathrm{BD}}(m)$, the UE has the phase-corrected received signal $|g_{\mathrm{BD}}(m)| s_{t_k} + y_{\mathrm{I+N}}(m) e^{-j \angle g_{\mathrm{BD}}(m)}$. EGC then adds together the M phase-corrected received signals. This results in an SINR for the BD transmission from t_k, as derived in Appendix B.3, of

$$\mathrm{SINR}_k^{(2)} = \frac{\left(\begin{array}{c} \sum_{m=1}^{M} \Big(\mathbb{E}\{|S_2(m)|^2\} + \mathbb{E}\{|R_2(m)|^2\} \Big) + \\ \frac{\pi}{4} \sum_{i=1}^{M} \sum_{\substack{j=1, \\ j \neq i}}^{M} \sqrt{\big(\mathbb{E}\{|S_2(i)|^2\} + \mathbb{E}\{|R_2(i)|^2\} \big) \big(\mathbb{E}\{|S_2(j)|^2\} + \mathbb{E}\{|R_2(j)|^2\} \big)} \end{array} \right)}{M \sigma_n^2 + \sum_{m=1}^{M} \Big(I_{\mathrm{res}}(m) + \mathbb{E}\{|R_1(m)|^2\} \Big)} \tag{5.25}$$

where

$$\mathbb{E}\{|S_2(m)|^2\} = p_t\,\alpha_{t_k}(m)\Bigg(\sum_{n\in\mathcal{A}_k(m)}\eta_{nk}(m)\Bigg[|\mu_{1,nk}(m)|^2\mathrm{tr}(\mathbf{R}_{b_nt_ku_k}\hat{\mathbf{Q}}_{b_nu_k}) + |\mu_{2,nk}(m)|^2\mathrm{tr}(\tilde{\mathbf{R}}_{b_nt_ku_k}\hat{\mathbf{Q}}_{b_nt_ku_k})\Bigg] + \sum_{i\in\mathcal{A}_k(m)}\sum_{j\in\mathcal{A}_k(m)}\sqrt{\eta_{ik}(m)\eta_{jk}(m)}\,\mu_{2,ik}(m)\mu^*_{2,jk}(m)\Bigg), \tag{5.26}$$

$$\begin{aligned} I_{\mathrm{res}}(m) = &\sum_{n\in\mathcal{A}_k(m)} p_t\eta_{nk}(m)\Bigg[|\mu_{1,nk}(m)|^2\mathrm{tr}(\tilde{\mathbf{R}}_{b_nu_k}\hat{\mathbf{Q}}_{b_nu_k}) \\ &+ |\mu_{2,nk}(m)|^2\Big(\mathrm{tr}(\hat{\mathbf{R}}_{b_nu_k}\hat{\mathbf{Q}}_{b_nt_ku_k}) + \mathbb{E}\{\tilde{\mathbf{g}}^H_{b_nu_k}\hat{\mathbf{q}}_{b_nt_ku_k}\hat{\mathbf{q}}^H_{b_nt_ku_k}\tilde{\mathbf{g}}_{b_nu_k}\}\Big)\Bigg] \\ &+\sum_{i\in\mathcal{A}_k(m)}\sum_{j\in\mathcal{A}_k(m)\setminus i} p_t\sqrt{\eta_{ik}(m)\eta_{jk}(m)}\,\mu_{2,ik}(m)\mu^*_{2,jk}(m)\,\mathbb{E}\{\tilde{\mathbf{g}}^H_{b_iu_k}\hat{\mathbf{q}}_{b_it_ku_k}\}\mathbb{E}\{\hat{\mathbf{q}}^H_{b_jt_ku_k}\tilde{\mathbf{g}}_{b_ju_k}\}, \end{aligned} \tag{5.27}$$

and $\mathbb{E}\{|R_1(m)|^2\}$ and $\mathbb{E}\{|R_2(m)|^2\}$ are the same as in (5.22) and (5.23), respectively, with the index m added where needed.

Since we are using a practical modulation scheme (BPSK) at the BD devices instead of a Gaussian-distributed signal constellation, the BER gives a better insight into the BD performance than the data rate. With BPSK, 1 minus the BER can also be considered as the "goodput" of the BD, i.e., how many bits are received on average without error per channel use (or per second per Hz). For BPSK, the (uncoded[9]) BER for the BD transmission from t_k is [172, Eq. (4.3-13)]

$$\mathrm{BER}_k^{(2)} = Q\left(\sqrt{2\cdot\mathrm{SINR}_k^{(2)}}\right), \tag{5.28}$$

where $Q(x) = \frac{1}{\sqrt{2\pi}}\int_x^\infty \exp(\frac{-u^2}{2})\,du$.

5.2.2 Harvested Power at the BDs

To calculate the power harvested at BD t_k, first we formulate the received signal at t_k from the APs as

$$\begin{aligned} y_{t_k} &= \sum_{n=1}^{N}\sum_{k'\in\mathcal{U}_n}\sqrt{p_t\eta_{nk'}}\,\mathbf{g}^H_{b_nt_k}\mathbf{w}_{nk'}s_{k'} + n_{t_k} \\ &= \sum_{n=1}^{N}\sum_{k'\in\mathcal{U}_n}\sqrt{p_t\eta_{nk'}}\left(\mu_{1,nk'}\frac{\mathbf{g}^H_{b_nt_k}\hat{\mathbf{g}}_{b_nu_{k'}}}{||\hat{\mathbf{g}}_{b_nu_{k'}}||^2} + \mu_{2,nk'}\frac{\mathbf{g}^H_{b_nt_k}\hat{\mathbf{g}}_{b_nt_{k'}u_{k'}}}{||\hat{\mathbf{g}}_{b_nt_{k'}u_{k'}}||^2}\right)s_{k'} + n_{t_k}, \end{aligned} \tag{5.29}$$

[9]If an error correction code is used at the BD, this can be accounted for by multiplying the SINR by a coding gain.

where $n_{t_k} \sim \mathcal{CN}(0, \sigma_{n_t}^2)$. Since a BD only includes passive components, and it performs few signal processing operations itself, it can be assumed that the thermal noise at the BD is insignificant relative to the total power from the APs. Thus, we can omit the effect of n_{t_k} when calculating the average total received power, similarly to [56, 173, 174]. Since the data symbols to different UEs are uncorrelated, the average total received power $P_{t_k} = \mathbb{E}\{|y_{t_k}|^2\}$ at BD t_k is

$$P_{t_k} = p_t \left(\sum_{n=1}^{N} \sum_{k' \in \mathcal{U}_n} \eta_{nk'} \mathbb{E}\left\{ \mathbf{g}_{b_n t_k}^H \mathbf{w}_{nk'} \mathbf{w}_{nk'}^H \mathbf{g}_{b_n t_k} \right\} + \sum_{i=1}^{N} \sum_{\substack{j=1, \\ j \neq i}}^{N} \sum_{k' \in \mathcal{U}_i \cap \mathcal{U}_j} \sqrt{\eta_{ik'} \eta_{jk'}}\, \mathbb{E}\left\{ \mathbf{g}_{b_i t_k}^H \mathbf{w}_{ik'} \mathbf{w}_{jk'}^H \mathbf{g}_{b_j t_k} \right\} \right) \tag{5.30}$$

The expectation terms in (5.30) are similar to those that appear when deriving the SINR expressions, except for the presence of $\mathbf{g}_{b_n t_k}$ instead of $\mathbf{g}_{b_n u_k}$ or $\mathbf{g}_{b_n t_k u_k}$. We may replace $\mathbf{g}_{b_n t_k}$ by $\frac{\mathbf{g}_{b_n t_k u_k}}{\sqrt{\Gamma_0}\, g_{t_k u_k}}$ to reuse some of those earlier derivations. Three separate cases arise for the terms: 1) when $k' = k$, 2) when $k' \neq k$ and UEs k and k' share a pilot sequence, and 3) UEs k and k' do not share a pilot sequence. Accounting for these cases, the received power becomes

$$\begin{aligned} P_{t_k} = \frac{p_t}{\Gamma_0 |g_{t_k u_k}|^2} \Bigg(& \sum_{n=1}^{N} \sum_{k' \in \mathcal{U}_n} \eta_{nk'} \left[|\mu_{1,nk'}|^2 \mathrm{tr}(\mathbf{R}_{b_n t_k u_k} \hat{\mathbf{Q}}_{b_n u_{k'}}) + |\mu_{2,nk'}|^2 \chi_{nk'} \right] \\ & + \sum_{i=1}^{N} \sum_{\substack{j=1, \\ j \neq i}}^{N} \sum_{k' \in \mathcal{U}_i \cap \mathcal{U}_j} \sqrt{\eta_{ik'} \eta_{jk'}}\, \mu_{2,ik'} \mu_{2,jk'}^{*} \chi_{ijk'} \Bigg), \end{aligned} \tag{5.31}$$

where

$$\chi_{nk'} = \begin{cases} 1 + \mathrm{tr}(\tilde{\mathbf{R}}_{b_n t_k u_k} \hat{\mathbf{Q}}_{b_n t_k u_k}), & \text{if } k' = k, \\ \mathbb{E}\left\{ \mathbf{g}_{b_n t_k u_k}^H \hat{\mathbf{q}}_{b_n t_{k'} u_{k'}} \hat{\mathbf{q}}_{b_n t_{k'} u_{k'}}^H \mathbf{g}_{b_n t_k u_k} \right\}, & \text{if } k' \neq k \text{ and } k' \in \mathcal{S}_k, \\ \mathrm{tr}(\mathbf{R}_{b_n t_k u_k} \hat{\mathbf{Q}}_{b_n t_{k'} u_{k'}}), & \text{if } k' \neq k \text{ and } k' \notin \mathcal{S}_k, \end{cases} \tag{5.32}$$

and

$$\chi_{ijk'} = \begin{cases} 1, & \text{if } k' = k, \\ \mathbb{E}\left\{ \mathbf{g}_{b_i t_k u_k}^H \hat{\mathbf{q}}_{b_i t_{k'} u_{k'}} \right\} \mathbb{E}\left\{ \hat{\mathbf{q}}_{b_j t_{k'} u_{k'}}^H \mathbf{g}_{b_j t_k u_k} \right\}, & \text{if } k' \neq k \text{ and } k' \in \mathcal{S}_k, \\ 0, & \text{if } k' \neq k \text{ and } k' \notin \mathcal{S}_k. \end{cases} \tag{5.33}$$

Like in [175, 176], we consider a constant circuit power consumption rate in the BDs. Since we assume the use of PS for energy harvesting, only a fraction $1 - \alpha_{t_k}$ of

the received power goes toward power harvesting in BD t_k. Hence, the total harvested power in BD t_k (to run its circuitry) is

$$P_{t_k}^{har} = \zeta(1 - \alpha_{t_k})P_{t_k}, \tag{5.34}$$

where ζ is the RF-to-DC conversion efficiency.

5.3 Simulation Results

In this section, we numerically evaluate the performance of the proposed CF mMIMO system with underlaid symbiotic backscatter communication. We assume that $N = 25$ APs, each with $L = 4$ antennas, and $K = 20$. legacy UEs are uniformly distributed at random within a square of size 0.5 km $\times$ 0.5 km. Furthermore, we assume each BD is distributed uniformly over the area of a circle centered at its associated UEs with a radius at of $d_{t_k u_k}^{\max} = 0.5$ m. In order to avoid boundary effects when simulating the CF network, distances are measured wrapped around the borders of the simulation area.

For large-scale fading, we use the 3GPP Urban Microcell non-line-of-sight hexagonal cell layout path loss and shadow fading model [135, Table B.1.2.1-1], also used in [177]. The large-scale fading Λ_{xy} (in dB) is then given by

$$\Lambda_{xy} = 30.5 + 36.7 \log_{10}(d_{xy}) + \Omega_{xy}, \tag{5.35}$$

where d_{xy} (in m) is the 3D distance between AP x and UE/BD y, which accounts for the border wraparound and antenna heights of 10 m. Ω_{xy} represents lognormal shadow fading and is distributed (in dB) as $\sim \mathcal{N}(0, 4^2)$. The shadowing values between all nodes (i.e., an AP, UE, or BD) are assumed to be jointly correlated according to Gudmunson's exponential correlation model [171, Ch. 2.6.1],[135]. The shadowing correlation parameter κ (normalized to a shadowing standard deviation of 1) between any two given nodes is given by

$$\kappa = \exp(-\Delta/d_{corr}), \tag{5.36}$$

where Δ is the distance between the two nodes, and $d_{corr} = 13$ m [135, Table B.1.2.2.1-4] is the shadowing correlation distance of the environment. Finally, the large-scale fading parameter $\beta_{xy} = 10^{-\Lambda_{xy}/10}$. For $g_{t_k u_k}$, we instead use a slightly modified[10] version of the propagation model used in [62], given (in dB) as

$$\Lambda_{t_k u_k} = \max\left(26 + 20\log_{10}(d_{t_k u_k}),\, 0\right) \tag{5.37}$$

Then, the same as before, $\beta_{t_k u_k} = 10^{-\Lambda_{t_k u_k}/10}$. Since (5.37) models a single-path line-of-sight environment, the complex phase of $g_{t_k u_k}$ is assumed to be zero (i.e., $g_{t_k u_k}$ is real-valued).

The spatial correlation matrix of the small-scale part of the channel vector from multi-antenna AP x to UE/BD y is modeled based on the local scattering model described in [8, Ch. 2]. With $\mathbf{g}_{xy} = \sqrt{\beta_{xy}}\,\mathbf{h}_{xy}$ as in (5.1), element (a, b) of the covariance matrix of $\mathbf{h}_{xy}$ is given by

$$\exp\left[2\pi j d_H(a-b)\sin(\phi) - \frac{\sigma_\phi^2}{2}\left(2\pi d_H(a-b)\cos(\phi)\right)^2\right]. \tag{5.38}$$

d_H is the antenna spacing (in multiples of wavelengths), ϕ (in radians) is the nominal angle between the antenna array at AP x and UE/BD y, and σ_ϕ (in radians) is the angular standard deviation (ASD). The approximation in (5.38) is for a uniform linear array and a Gaussian distribution of angles of arrival of paths around the nominal central angle. For this approximation to be valid, the ASD must be small, e.g., below $\frac{\pi}{12}$ radians (15°). Based on [8, 178], we assume $\sigma_\phi = \frac{\pi}{18}$ radians (10°) herein.

Unless otherwise stated, we use the following simulation settings: primary bandwidth $B_1 = 20$ MHz, carrier frequency 2 GHz, noise figure 7 dB, $\tau_1 = \tau_2 = 10$, $\rho_{k,1} = \rho_{k,2} = 0.1$ W for all k, $\Gamma_0 = 0.64$ [55], $\zeta = 1$ [179], $p_t = 1$ W [99], $\alpha_{t_k} = 0.1$ for all k, and $M = 40$. At the APs, the two components of their estimated precoded channels (that is, $\hat{\mathbf{g}}_{b_n u_k}^H \hat{\mathbf{q}}_{b_n u_k}$ and $\hat{\mathbf{g}}_{b_n t_k u_k}^H \hat{\mathbf{q}}_{b_n t_k u_k}$) end up as being real-valued. Therefore, it may be assumed that the multipliers $\mu_{1,nk}$ and $\mu_{2,nk}$ are also real numbers.

[10] We include the max in (5.37) to prevent the path loss from becoming negative (i.e., a path gain) in the event $d_{t_k u_k}$ happens to be less than 5 cm.

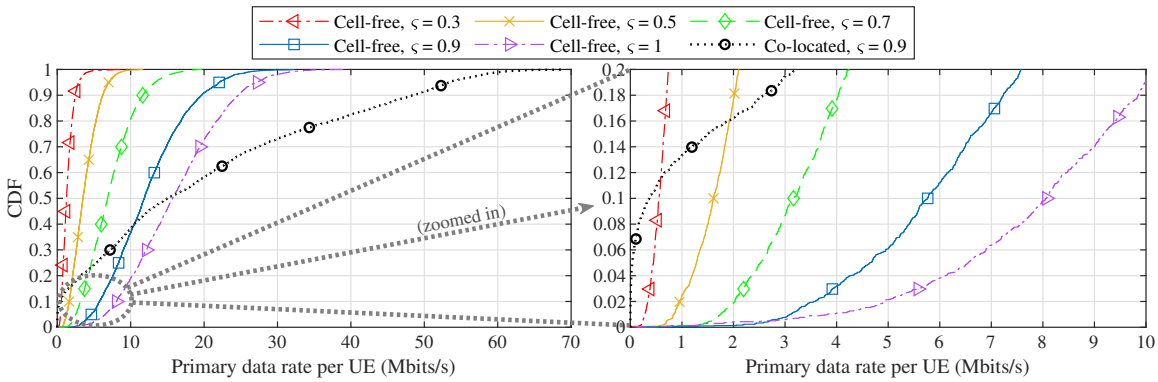

Figure 5.2: CDFs of primary transmission data rates per UE for SR CF mMIMO with different values of ς. CDF for co-located mMIMO with $\varsigma = 0.9$ also shown for comparison.

Let us define ς such that $\mu_{1,nk} = \varsigma||\hat{\mathbf{g}}_{b_n u_k}||$. Then, $\mu_{2,nk} = ||\hat{\mathbf{g}}_{b_n t_k u_k}||\sqrt{1-\varsigma^2}$, with our default value being $\varsigma = 0.9$. Lastly, we assume full power transmission at all APs and equal power allocation to every UE at each AP, so that $\eta_{n,k} = 1/|\mathcal{U}_n|$.

Fig. 5.2 shows the CDFs of the data rate per UE for the primary transmission in the SR mMIMO system. It can be observed that for CF mMIMO, when varying ς from 0.3 to 0.9, the data rate per UE increases significantly. This can be explained by the fact that increasing ς gives more emphasis to the portion of the precoded beams directed toward the UEs; hence, the SINR of the primary transmission (and thus its data rate) increases. For $\varsigma = 0.9$, the median data rate is about 12 Mbits/s, whereas for $\varsigma = 0.7$, the median decreases to about 7 Mbits/s; at $\varsigma = 0.7$, the UE data rate is less than 12 Mbits/s about 90% of the time. By further decreasing ς to 0.5 and 0.3, the data rates correspondingly decrease even more. At this point, no UE can achieve 11.4 Mbits/s anymore, whereas that previously was the median rate for $\varsigma = 0.9$. For $\varsigma = 0.3$, the median rate of the primary transmission is only 1.3 Mbits/s. Therefore, the value of ς has a significant impact on the quality of service of the primary transmissions from the CF mMIMO network. By increasing ς to 1, the primary data rates are the highest, as expected. In this case, there are no longer any beams intended for the BDs and all the power is directed toward the UEs.

For comparison, for $\varsigma = 0.9$, we also show the CDF of the primary transmission

data rates achieved by a co-located mMIMO system with its BS (at the center of the simulation area) having the same total transmit power and number of antennas as all the APs in the CF system. As expected, CF mMIMO provides considerably more uniform data rates for the UEs (i.e., steeper CDFs) than co-located mMIMO. Although some UEs that are closest to the co-located mMIMO BS achieve very high data rates for their primary transmissions, the rates for UEs at the edge of the coverage area is quite low. From Fig. 5.2(b), the 5th percentile rate for co-located mMIMO is only about 41.4 Kbits/s/Hz. In comparison, for CF mMIMO, the 5th percentile rates for $\varsigma = 0.3$, 0.5, 0.7, and 0.9 are about 0.44, 1.28, 2.52 and 4.68 Mbits/s, respectively.

To examine the impact of the value of ς on the performance, Fig. 5.3 depicts the average SINR and BER per BD vs. ς, while Fig. 5.4 shows the average harvested power per BD vs. ς. Both figures compare the performance of CF mMIMO with co-located mMIMO. Please recall from (5.19) and the numerator of (5.25), the part of the overall signal y_k reflected off of BD t_k includes two components: S_2, consisting of those signals intended for UE u_k from its serving APs, and R_2, consisting of signals from all APs intended for UEs other than u_k. As previously noted, because S_2 and R_2 are both reflected off t_k, they both represent and contain a useful part of the signal sent from t_k. We have observed in our simulations that for CF mMIMO, the power of component R_2 can be significant and may even surpass the power of component S_2. It is known that the degree of favorable propagation is less for CF mMIMO than it is with co-located mMIMO [34]; that is, the channel directions between different UEs are further from being orthogonal to each other. It is for this reason that the power of R_2 can be much more significant in CF mMIMO than in co-located MIMO, since ENCB precoding does not actively suppress interference between UEs. Furthermore, recall from earlier that we assume that the channels between a BD and a non-paired UE or another BD are blocked. Thus, any power an AP directs in a beam specifically towards a given BD will not reach any other BD. For these reasons, with CF mMIMO,

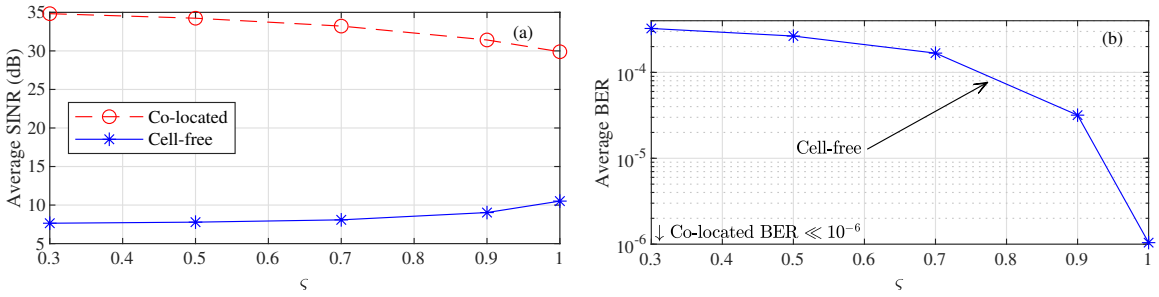

Figure 5.3: Average performance per BD for CF mMIMO and co-located mMIMO when varying ς; $\alpha_{t_k} = 0.1$. (a) SINR vs. ς. (b) BER vs. ς.

by increasing ς the impact of R_2 from non-serving APs increases, and consequently the SINR of the transmission from a BD increases on average. Increasing ς from 0.3 to 1 results in the BD SINR increasing from about 7.6 dB to about 10.5 dB, and decreases the uncoded BER of the BD transmission from about 3.2×10^{-4} to about 1.0×10^{-6}. Due to having a higher degree of favorable propagation and only one transmitting node, the same type of result is not observed for co-located mMIMO. In this case, the impact of R_2 is much smaller than that of S_2, and hence increasing ς leads to a decrease in the BD SINR and increase in the BER. (However, considering the very small BERs observed for co-located mMIMO, this is not much of an issue.)

As for the harvested power, Fig. 5.4 shows that increasing ς leads to a decrease in the amount of power harvested for both CF mMIMO and co-located mMIMO, since less power is directed specifically toward the BDs. Although for $\varsigma = 0.3$ the average amount of power harvested by the BDs is greater for co-located mMIMO than for CF mMIMO (about 12.6 µW vs. about 12.2 µW), by increasing ς this amount drops well below that of CF mMIMO (e.g., about 3.0 µW vs. about 9.9 µW with $\varsigma = 1$). This result may again be expected on account of the difference in the degree of favorable propagation between the two scenarios. It can also be seen that the amount that the harvested power changes with ς is considerably smaller. This is also due to the fact that a UE-BD pair is on average much closer to an AP in CF mMIMO than it would be to the BS in co-located mMIMO. Thus, the BD can generally harvest more power from the nearby APs in CF mMIMO, despite their amount of transmitted power per

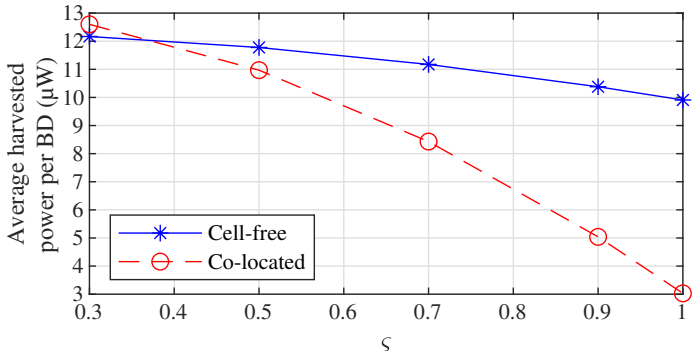

Figure 5.4: Average harvested power per BD vs. ς for CF mMIMO and co-located mMIMO; $\alpha_{t_k} = 0.1$.

AP being less than that of the BS in co-located MIMO.

Based on these simulation results, we can conclude that in a scenario like ours where BDs are close to their paired UEs, using CF mMIMO with ENCB precoding eliminates much of the need for some special consideration of the existence of BDs. In consideration of the amount of harvested power the BDs need to operate and the value of SINR/BER that is achieved, the best choice for the APs might be to simply precode signals only for the primary UEs, and let the BDs scavenge off of those signals. This appears to be the opposite of the case for co-located mMIMO. In that case, due to a combination of the higher degree of favorable propagation and the one BS being on average further from the BDs, it appears useful to explicitly direct some power towards the BDs in a co-located mMIMO system.

In Fig. 5.5, we examine the impact of the value of the PS ratio α_{t_k} on average SINR and harvested power of the BDs. (We do not depict the BER this time, since it rapidly falls well below 10^{-6}.) First, it can be observed that by increasing α_{t_k} from 0.1 to 0.9, the average harvested power decreases approximately linearly. For larger values of α_{t_k}, more power is allocated to the backscattered signal transmission, and thus less power will be harvested. On the other hand, by increasing α_{t_k}, the average SINR of the BD transmission increases for the same reason: more power has been allocated to it. Similarly, the BER decreases with increasing α_{t_k} as well. Hence, as expected, there is a trade-off between the amount of power harvested by the BDs

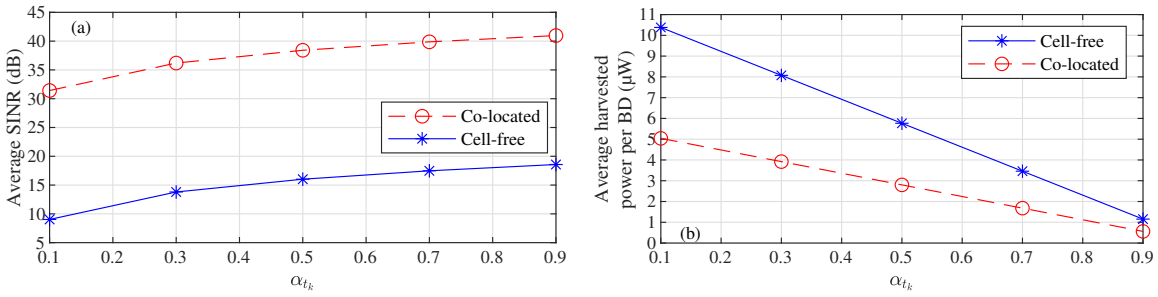

Figure 5.5: Average performance per BD for CF mMIMO and co-located mMIMO when varying α_{t_k}; $\varsigma = 0.9$. (a) SINR vs. α_{t_k}. (b) Harvested power vs. α_{t_k}.

and the SINR/BER of their transmissions. The SINR and BER results must be viewed with a caveat, however. If the harvested power drops below some threshold needed for the BD to operate, then the SINR and BER in Fig. 5.5 are not actually achievable, since the BD would not be able to transmit to begin with. The circuit power consumption for backscattering is estimated to be around 8.9 μW [**shyz20**].

In these simulations, we have assumed that all the BDs use the same value of α_{t_k}. However, by considering the specific channel conditions and requirements of each BD, the value of α_{t_k} could be optimized for each of them. In such a case, the performance of the system is expected to improve significantly.

5.4 Summary

In this chapter, we have investigated the performance of CF mMIMO in facilitating the implementation of BC. First, an efficient two-phase channel estimation method has been proposed to estimate the direct-link channel and cascaded backscatter channel by considering the effects of pilot contamination and spatial correlation between antennas. However, the receivers have been assumed to only have partial CSI (statistical knowledge plus instantaneous phase information for partially-coherent reception). Assuming UL/DL radio channel reciprocity, the CSI has been used to design DL precoding vectors for the APs such that channel hardening is enhanced and both primary receivers and BDs benefit. Then, SINRs of both primary and secondary transmission taking into account the effect imperfect CSI, spatial correlation, pilot contamination,

and channel hardening have been derived. Moreover, the average power harvested in the BDs is derived. Simulation results have been provided to demonstrate the performance of the SR CF mMIMO systems.

Chapter 6

Conclusions, Recommendations and Future Work

6.1 Summary of Contributions

In Chapter 3, the energy-efficient deployment of MIMO in SC HetNets has been considered. MIMO and SC deployments need to be integrated with well-designed interference mitigation and resource allocation methods to achieve high EE. To this end, we have proposed and investigated user-centric clustering and coordinated beamforming with null-space projection and ZF precoding to mitigate interference in a HetNet. A single-RF-chain massive MIMO transceiver design for the macro cell and antenna selection for the SCs have been proposed to reduce hardware power consumption. We have designed a joint antenna selection and RB allocation algorithm, followed by a power optimization algorithm, to maximize the system EE under the additional constraints of minimum guaranteed user rates and maximum fronthaul capacity limits. The power allocation problem has been solved using the Dinkelbach method. Simulation results have demonstrated that our proposed methodology and algorithms ensure higher EE than previously known benchmark algorithms while being significantly less complex than an exhaustive search. The effect on the system EE and SE performance when varying the clustering threshold, the number of users, cell association bias, fronthaul capacity, and reliability of CSI has been examined.

In Chapter 4, we have investigated several different iterative matrix inversion meth-

ods for CF mMIMO systems to avoid direct matrix inversion for ZF precoding. Unlike related works, both small- and large-scale fading have been considered in our channel model, along with spatial correlation of co-located antennas at APs, when examining these iterative methods' performance and computational complexity. Our examination has demonstrated that, unlike co-located mMIMO, when large-scale fading is factored in, the JC inversion method is no longer guaranteed to converge. While the GS method does converge, its computations cannot be done in parallel. Therefore, we have focused on regular and factorized versions of the HP inversion method. Several initialization points for the HP method have been examined, and their effect on the performance was studied; we found that lower-complexity initialization points performed suitably well. We have also considered HP methods for the Moore-Penrose pseudoinverse and have found that they perform similarly to the matrix inverse but at a much higher complexity when in the typical mMIMO regime of many more antennas than users. The factorized HP method with $r = 15$ exhibits the fastest convergence and best computational efficiency E_c of the iterative methods examined. However, it also requires significant parallelization of computations to achieve the low latency of direct inversion. We have also briefly examined the iterative inversion schemes with scalable CF mMIMO systems. We have found that these methods converge somewhat slower in this case. Moreover, there are also several lower-dimensional matrices to invert instead of one large matrix.

To investigate the compatibility of AmBC and CF mMIMO, in Chapter 5, we have examined the performance of SR underlaying a CF mMIMO network. A two-phase pilot-based channel estimation method has been proposed to obtain separate estimates for the direct-link and cascaded backscatter channels at the APs. The derived channel estimates account for the effects of pilot contamination and spatial correlation between the antennas at the APs. In contrast, other works in the literature tend to neglect these factors. For DL precoding, we have modified ENCB [98], so the APs can assist both primary and BD transmissions while enhancing channel hardening. Ex-

pressions for the average SINRs of both primary and backscatter transmissions have been derived, and for the average harvested energy in the BDs. Our derived expressions account for the effects of channel estimation error, pilot contamination, spatial correlation between the AP antennas, knowledge of only the statistics of the CSI (both magnitude and phase) for the primary transmissions, and partially-coherent reception of BD transmissions. Lastly, we have compared the performance of SR underlaying CF mMIMO to that of SR underlaying co-located mMIMO. We demonstrated that using CF mMIMO results in much more uniformity of data rates for the primary transmissions across the users. Furthermore, the performance of the AmBC layer was shown to have considerably less dependence on the amount of power the APs specifically direct towards PRs vs. BDs than in a co-located mMIMO system. The most notable conclusion was that excellent performance for both the primary and AmBC layers could be obtained in a CF mMIMO system without having to account for the presence of BDs in the system specifically; the same cannot be said for a co-located mMIMO system.

6.2 Future Work

Future direction for Chapter 3 may involve the addition of user scheduling for even larger numbers of users requesting service, as well as the impact of user mobility on the performance of the proposed scheme. Also, the current work has mostly assumed perfect channel estimation. However, imperfect CSI due to pilot contamination [15, 180] is quite common in practical massive MIMO systems. Therefore, future work should account for its effects on the system and the proposed scheme.

Scalable CF mMIMO would likely experience the most benefit from parallelization; the matrix inversion problem can be split into parallel computations between APs, between the matrices at each AP, and/or within each of those matrices. Furthermore, as the scalable name implies, the system can be scaled to an arbitrarily large size, so the parallelization per AP would be about the same, regardless of the total number of

APs/antennas in the system. A more in-depth examination of this specific scenario may be the subject of future work related to Chapter 4.

The closed-form expressions that have been derived in Chapter 5 for the SINRs of both the primary and backscattered signals, as well as for the average amount of power harvested by each BD, can be employed in future work as part of an optimal resource allocation strategy for a symbiotic CF mMIMO system. It is expected that joint optimization of the amount of transmitted power allocated to each primary signal (i.e., η_{nk}), the PS ratio α_{t_k} for each BD, and the complex-valued weights $\mu_{1,nk}$ and $\mu_{2,nk}$ of the precoding vector will significantly improve the performance of the proposed SR CF mMIMO system and will help facilitate the implementation of energy-efficient IoT. Moreover, a scenario in which multiple BDs may be associated with each UE is an interesting topic that can be considered as future work. Finally, the modified ENCB precoding used in this work does not actively cancel interference between UEs. Using a precoding method, such as zero-forcing or otherwise, that suppresses interference between UEs provides significantly better data rates to the UEs, especially in CF MIMO systems [34]. However, such precoding methods also direct power away from certain channel directions or subspaces, meaning that said power may no longer always be available for BDs to harvest. Hence, future work should explore SR CF mMIMO systems using different precoding schemes to investigate the effect on the underlying AmBC layer. The BDs may then have to be explicitly supported by the APs (or at least to a larger degree) compared to what we observed when using modified ENCB precoding.

Bibliography

[1] Ericsson, "Ericsson mobility report," Tech. Rep., Nov. 2021. Accessed: Sept. 25, 2022. [Online]. Available: https://www.ericsson.com/en/reports-and-papers/mobility-report/dataforecasts/mobile-traffic-forecast.

[2] "Cisco Annual Internet Report, 2018–2023," Cisco White Paper, Mar. 2020. Accessed: Sept. 28, 2022. [Online]. Available: https://www.cisco.com/c/en/us/solutions/collateral/executive-perspectives/annual-internet-report/white-paper-c11-741490.html.

[3] "IMT vision – Framework and overall objectives of the future development of IMT for 2020 and beyond," International Telecommunication Union, Recommendation ITU-R M.2083-0 (09/2015), 2015.

[4] E. Björnson, L. Sanguinetti, and M. Kountouris, "Deploying dense networks for maximal energy efficiency: Small cells meet massive MIMO," *IEEE J. Sel. Areas Commun.*, vol. 34, no. 4, pp. 832–847, 2016.

[5] J. Huang, Y. Meng, X. Gong, Y. Liu, and Q. Duan, "A novel deployment scheme for green Internet of Things," *IEEE Internet Things J.*, vol. 1, no. 2, pp. 196–205, 2014.

[6] O. Souihli and T. Ohtsuki, "Benefits of rich scattering in MIMO channels: A graph-theoretical perspective," *IEEE Commun. Lett.*, vol. 17, no. 1, pp. 23–26, 2013.

[7] J. Hoydis, S. ten Brink, and M. Debbah, "Massive MIMO in the UL/DL of cellular networks: How many antennas do we need?" *IEEE J. Sel. Areas Commun.*, vol. 31, no. 2, pp. 160–171, 2013.

[8] E. Björnson, J. Hoydis, and L. Sanguinetti, "Massive MIMO networks: Spectral, energy, and hardware efficiency," *Foundations and Trends in Signal Process.*, vol. 11, no. 3–4, pp. 154–655, 2017.

[9] Rysavy Research, "Global 5G: Implications of a transformational technology," 5G Americas White Paper, Sept. 2019. Accessed: Jan. 26, 2021. [Online]. Available: https://www.5gamericas.org/wp-content/uploads/2019/09/2019-5G-Americas-Rysavy-Implications-of-a-Transformational-Technology-White-Paper.pdf.

[10] "Multiplexing and channel coding (release 15)," 3rd Generation Partnership Project, Tech. Spec. 3GPP TS 38.212 v15.9.0 (2020-06), 2020.

[11] H. Q. Ngo and E. G. Larsson, "No downlink pilots are needed in TDD massive MIMO," *IEEE Trans. Wireless Commun.*, vol. 16, no. 5, pp. 2921–2935, 2017.

[12] E. Björnson, E. G. Larsson, and T. L. Marzetta, "Massive MIMO: Ten myths and one critical question," *IEEE Commun. Mag.*, vol. 54, no. 2, pp. 114–123, 2016.

[13] E. G. Larsson, O. Edfors, F. Tufvesson, and T. L. Marzetta, "Massive MIMO for next generation wireless systems," *IEEE Commun. Mag.*, vol. 52, no. 2, pp. 186–195, 2014. DOI: 10.1109/MCOM.2014.6736761.

[14] J. Jose, A. Ashikhmin, T. L. Marzetta, and S. Vishwanath, "Pilot contamination and precoding in multi-cell TDD systems," *IEEE Trans. Wireless Commun.*, vol. 10, no. 8, pp. 2640–2651, 2011.

[15] O. Elijah, C. Y. Leow, T. A. Rahman, S. Nunoo, and S. Z. Iliya, "A comprehensive survey of pilot contamination in massive MIMO—5G system," *IEEE Commun. Surveys Tuts.*, vol. 18, no. 2, pp. 905–923, 2016.

[16] H. Mohammadghasemi, M. F. Sabahi, *et al.*, "Pilot-decontamination in massive MIMO systems using interference alignment," *IEEE Commun. Lett.*, vol. 24, no. 3, pp. 672–675, 2020.

[17] L. A. Lago, Y. Zhang, N. Akbar, Z. Fei, N. Yang, and Z. He, "Pilot decontamination based on superimposed pilots assisted by time-multiplexed pilots in massive MIMO networks," *IEEE Trans. Veh. Technol.*, vol. 69, no. 1, pp. 405–417, 2020.

[18] K. Upadhya, S. A. Vorobyov, and M. Vehkapera, "Superimposed pilots are superior for mitigating pilot contamination in massive MIMO," *IEEE Trans. Signal Process.*, vol. 65, no. 11, pp. 2917–2932, 2017.

[19] J. G. Andrews, "Seven ways that HetNets are a cellular paradigm shift," *IEEE Commun. Mag.*, vol. 51, no. 3, pp. 136–144, 2013.

[20] J. Hoydis, M. Kobayashi, and M. Debbah, "Green small-cell networks," *IEEE Veh. Technol. Mag.*, vol. 6, no. 1, pp. 37–43, 2011.

[21] D. Lopez-Perez, I. Guvenc, G. de la Roche, M. Kountouris, T. Q. Quek, and J. Zhang, "Enhanced intercell interference coordination challenges in heterogeneous networks," *IEEE Wireless Commun.*, vol. 18, no. 3, pp. 22–30, 2011.

[22] U. Siddique, H. Tabassum, E. Hossain, and D. I. Kim, "Wireless backhauling of 5G small cells: Challenges and solution approaches," *IEEE Wireless Commun.*, vol. 22, no. 5, pp. 22–31, 2015.

[23] G. Miao, N. Himayat, G. Y. Li, and S. Talwar, "Distributed interference-aware energy-efficient power optimization," *IEEE Trans. Wireless Commun.*, vol. 10, no. 4, pp. 1323–1333, 2011.

[24] S. Cai, Y. Che, L. Duan, J. Wang, S. Zhou, and R. Zhang, "Green 5G heterogeneous networks through dynamic small-cell operation," *IEEE J. Sel. Areas Commun.*, vol. 34, no. 5, pp. 1103–1115, 2016.

[25] L. Budzisz *et al.*, "Dynamic resource provisioning for energy efficiency in wireless access networks: A survey and an outlook," *IEEE Commun. Surveys Tuts.*, vol. 16, no. 4, pp. 2259–2285, Fourthquarter 2014.

[26] D. Gesbert, S. Hanly, H. Huang, S. Shamai Shitz, O. Simeone, and W. Yu, "Multi-cell MIMO cooperative networks: A new look at interference," *IEEE J. Sel. Areas Commun.*, vol. 28, no. 9, pp. 1380–1408, 2010.

[27] "Coordinated multi-point operation for LTE physical layer aspects (release 11)," 3rd Generation Partnership Project, Tech. Rep. 3GPP TR 36.819 v11.2.0 (2013-09), 2013.

[28] D. Lee *et al.*, "Coordinated multipoint transmission and reception in LTE-advanced: Deployment scenarios and operational challenges," *IEEE Commun. Mag.*, vol. 50, no. 2, pp. 148–155, 2012.

[29] M. A. Habibi, M. Nasimi, B. Han, and H. D. Schotten, "A comprehensive survey of RAN architectures toward 5G mobile communication system," *IEEE Access*, vol. 7, pp. 70 371–70 421, 2019.

[30] J. Wu, Z. Zhang, Y. Hong, and Y. Wen, "Cloud radio access network (C-RAN): A primer," *IEEE Network*, vol. 29, no. 1, pp. 35–41, 2015. DOI: 10.1109/MNET.2015.7018201.

[31] Z. Hasan, H. Boostanimehr, and V. K. Bhargava, "Green cellular networks: A survey, some research issues and challenges," *IEEE Commun. Surveys Tuts.*, vol. 13, no. 4, pp. 524–540, 2011.

[32] A. Checko *et al.*, "Cloud ran for mobile networks—A technology overview," *IEEE Commun. Surveys Tuts.*, vol. 17, no. 1, pp. 405–426, 2015.

[33] M. Peng, Y. Li, J. Jiang, J. Li, and C. Wang, "Heterogeneous cloud radio access networks: A new perspective for enhancing spectral and energy efficiencies," *IEEE Wireless Commun.*, vol. 21, no. 6, pp. 126–135, 2014.

[34] Özlem Tugfe Demir, E. Björnson, and L. Sanguinetti, "Foundations of user-centric cell-free massive MIMO," *Foundations and Trends® in Signal Processing*, vol. 14, no. 3-4, pp. –, 2020, ISSN: 1932-8346. DOI: 10.1561/2000000109. [Online]. Available: http://dx.doi.org/10.1561/2000000109.

[35] G. Interdonato, E. Björnson, H. Q. Ngo, P. Frenger, and E. G. Larsson, "Ubiquitous cell-free massive MIMO communications," *EURASIP J Wirel Commun Netw*, vol. 2019, no. 1, p. 197, 2019.

[36] X.-H. You, D.-M. Wang, B. Sheng, X.-Q. Gao, X.-S. Zhao, and M. Chen, "Cooperative distributed antenna systems for mobile communications," *IEEE Wireless Commun.*, vol. 17, no. 3, pp. 35–43, 2010.

[37] H. Huang *et al.*, "Increasing downlink cellular throughput with limited network MIMO coordination," *IEEE Trans. Wireless Commun.*, vol. 8, no. 6, pp. 2983–2989, 2009.

[38] D. Lee *et al.*, "Coordinated multipoint transmission and reception in LTE-advanced: Deployment scenarios and operational challenges," *IEEE Commun. Mag.*, vol. 50, no. 2, pp. 148–155, 2012.

[39] H. Yang and T. L. Marzetta, "Energy efficiency of massive MIMO: Cell-free vs. cellular," in *Proc. 2018 IEEE 87th Veh. Technol. Conf. (VTC Spring),* Porto, Portugal, 2018, pp. 1–5.

[40] H. Q. Ngo, L. Tran, T. Q. Duong, M. Matthaiou, and E. G. Larsson, "On the total energy efficiency of cell-free massive MIMO," *IEEE Trans. Green Commun. Netw.*, vol. 2, no. 1, pp. 25–39, 2018.

[41] A. Al-Fuqaha, M. Guizani, M. Mohammadi, M. Aledhari, and M. Ayyash, "Internet of Things: A survey on enabling technologies, protocols, and applications," *IEEE Commun. Surveys Tuts.*, vol. 17, no. 4, pp. 2347–2376, 2015.

[42] L. Zhang, Y. Liang, and M. Xiao, "Spectrum sharing for internet of things: A survey," *IEEE Wireless Commun.*, vol. 26, no. 3, pp. 132–139, 2019.

[43] W. Zhang *et al.*, "A green paradigm for internet of things: Ambient backscatter communications," *China Communications*, vol. 16, no. 7, pp. 109–119, 2019.

[44] K. W. Choi *et al.*, "Simultaneous wireless information and power transfer (SWIPT) for Internet of Things: Novel receiver design and experimental validation," *IEEE Internet Things J.*, vol. 7, no. 4, pp. 2996–3012, 2020.

[45] K. Han and K. Huang, "Wirelessly powered backscatter communication networks: Modeling, coverage, and capacity," *IEEE Trans. Wireless Commun.*, vol. 16, no. 4, pp. 2548–2561, 2017.

[46] H. Stockman, "Communication by means of reflected power," *Proceedings of the IRE*, vol. 36, no. 10, pp. 1196–1204, 1948.

[47] H. Lehpamer, *RFID Design Principles*, 2nd ed. Boston, MA, USA: Artech House, 2012.

[48] D. Mishra and E. G. Larsson, "Optimal channel estimation for reciprocity-based backscattering with a full-duplex MIMO reader," *IEEE Trans. Signal Process.*, vol. 67, no. 6, pp. 1662–1677, 2019.

[49] X. Lu, D. Niyato, H. Jiang, D. I. Kim, Y. Xiao, and Z. Han, "Ambient backscatter assisted wireless powered communications," *IEEE Wireless Commun.*, vol. 25, no. 2, pp. 170–177, 2018.

[50] J. Kimionis, A. Bletsas, and J. N. Sahalos, "Increased range bistatic scatter radio," *IEEE Trans. Commun.*, vol. 62, no. 3, pp. 1091–1104, 2014.

[51] F. Rezaei, C. Tellambura, and S. Herath, "Large-scale wireless-powered networks with backscatter communications—a comprehensive survey," *IEEE Open J. Commun. Soc.*, vol. 1, pp. 1100–1130, 2020.

[52] X. Jia and X. Zhou, "Power beacon placement for maximizing guaranteed coverage in bistatic backscatter networks," *IEEE Trans. Commun.*, vol. 69, no. 11, pp. 7895–7909, 2021.

[53] G. Wang, F. Gao, R. Fan, and C. Tellambura, "Ambient backscatter communication systems: Detection and performance analysis," *IEEE Trans. Commun.*, vol. 64, no. 11, pp. 4836–4846, 2016. DOI: 10.1109/TCOMM.2016.2602341.

[54] N. Van Huynh, D. T. Hoang, X. Lu, D. Niyato, P. Wang, and D. I. Kim, "Ambient backscatter communications: A contemporary survey," *IEEE Commun. Surveys Tuts.*, vol. 20, no. 4, pp. 2889–2922, 2018.

[55] S. Ma, G. Wang, R. Fan, and C. Tellambura, "Blind channel estimation for ambient backscatter communication systems," *IEEE Commun. Lett.*, vol. 22, no. 6, pp. 1296–1299, 2018.

[56] X. Kang, Y. Liang, and J. Yang, "Riding on the primary: A new spectrum sharing paradigm for wireless-powered IoT devices," *IEEE Trans. Wireless Commun.*, vol. 17, no. 9, pp. 6335–6347, 2018.

[57] Y. Alsaba, S. K. A. Rahim, and C. Y. Leow, "Beamforming in wireless energy harvesting communications systems: A survey," *IEEE Commun. Surv. Tutor.*, vol. 20, no. 2, pp. 1329–1360, Secondquarter 2018.

[58] I. F. Akyildiz, A. Kak, and S. Nie, "6G and beyond: The future of wireless communications systems," *IEEE Access*, vol. 8, pp. 133 995–134 030, 2020.

[59] L. Bariah *et al.*, "A prospective look: Key enabling technologies, applications and open research topics in 6G networks," *IEEE Access*, vol. 8, pp. 174 792–174 820, 2020.

[60] S. Chen, Y.-C. Liang, S. Sun, S. Kang, W. Cheng, and M. Peng, "Vision, requirements, and technology trend of 6G: How to tackle the challenges of system coverage, capacity, user data-rate and movement speed," *IEEE Wireless Commun.*, vol. 27, no. 2, pp. 218–228, 2020.

[61] G. Yang, Q. Zhang, and Y.-C. Liang, "Cooperative ambient backscatter communications for green Internet-of-Things," *IEEE Internet Things J.*, vol. 5, no. 2, pp. 1116–1130, 2018.

[62] R. Long, Y.-C. Liang, H. Guo, G. Yang, and R. Zhang, "Symbiotic radio: A new communication paradigm for passive Internet of Things," *IEEE Internet Things J.*, vol. 7, no. 2, pp. 1350–1363, 2020.

[63] Y.-C. Liang, Q. Zhang, E. G. Larsson, and G. Y. Li, "Symbiotic radio: Cognitive backscattering communications for future wireless networks," *IEEE Trans. Cogn. Commun. Netw.*, vol. 6, no. 4, pp. 1242–1255, 2020.

[64] M. K. D. Gesbert, "From single user to multiuser communications: Shifting the MIMO paradigm," *IEEE Signal Process. Mag.*, vol. 24, no. 5, pp. 36–46, 2007.

[65] T. L. Marzetta, "Noncooperative cellular wireless with unlimited numbers of base station antennas," *IEEE Trans. Wireless Commun.*, vol. 9, no. 11, pp. 3590–3600, 2010.

[66] S. Gunnarsson, J. Flordelis, L. Van Der Perre, and F. Tufvesson, "Channel hardening in massive MIMO: Model parameters and experimental assessment," *IEEE Open J. Commun. Soc.*, vol. 1, pp. 501–512, 2020.

[67] Z. Chen and E. Björnson, "Channel hardening and favorable propagation in cell-free massive MIMO with stochastic geometry," *IEEE Trans. Commun.*, vol. 66, no. 11, pp. 5205–5219, 2018. DOI: 10.1109/TCOMM.2018.2846272.

[68] F. Rusek *et al.*, "Scaling up MIMO: Opportunities and challenges with very large arrays," *IEEE Signal Process. Mag.*, vol. 30, no. 1, pp. 40–60, 2013.

[69] H. Q. Ngo, E. G. Larsson, and T. L. Marzetta, "Aspects of favorable propagation in massive MIMO," in *Proc. 2014 22nd European Signal Process. Conf. (EUSIPCO)*, Lisbon, Portugal, Nov. 2014, pp. 76–80.

[70] B. Hochwald, T. Marzetta, and V. Tarokh, "Multiple-antenna channel hardening and its implications for rate feedback and scheduling," *IEEE Trans. Inf. Theory*, vol. 50, no. 9, pp. 1893–1909, 2004.

[71] E. Björnson, J. Hoydis, and L. Sanguinetti, "Massive MIMO networks: Spectral, energy, and hardware efficiency," *Foundations and Trends in Signal Process.*, vol. 11, no. 3–4, pp. 154–655, 2017.

[72] G. H. Golub and C. F. Van Loan, *Matrix Computations*, 4th ed. Baltimore, MD, USA: The John Hopkins Univ. Press, 2013.

[73] W. Song, X. Chen, L. Wang, and X. Lu, "Joint conjugate gradient and Jacobi iteration based low complexity precoding for massive MIMO systems," in *Proc. IEEE/CIC Int. Conf. Commun. China (ICCC)*, Chengdu, China, 2016, pp. 1–5.

[74] H. Prabhu, J. Rodrigues, O. Edfors, and F. Rusek, "Approximative matrix inverse computations for very-large MIMO and applications to linear pre-coding systems," in *Proc. IEEE Wireless Commun. Netw. Conf. (WCNC)*, Shanghai, China, 2013, pp. 2710–2715.

[75] H. Prabhu, O. Edfors, J. Rodrigues, L. Liu, and F. Rusek, "Hardware efficient approximative matrix inversion for linear pre-coding in massive MIMO," in *Proc. IEEE Int. Symp. Circuits Syst. (ISCAS)*, Melbourne, Australia, 2014, pp. 1700–1703.

[76] S. M. Abbas and C.-Y. Tsui, "Low-latency approximate matrix inversion for high-throughput linear pre-coders in massive MIMO," in *Proc. IFIP/IEEE Int. Conf. Very Large Scale Integration (VLSI-SoC)*, Tallinn, Estonia, 2016, pp. 1–5.

[77] B. Y. Kong and I.-C. Park, "Low-complexity symbol detection for massive MIMO uplink based on Jacobi method," in *Proc. IEEE 27th Annu. Int. Symp. Pers., Indoor, Mobile Radio Commun. (PIMRC)*, Valencia, Spain, 2016, pp. 1–5.

[78] J. Minango and C. de Almeida, "A low-complexity linear precoding algorithm based on Jacobi method for massive MIMO systems," in *Proc. IEEE 87th Veh. Technol. Conf. (VTC 2018-Spring)*, Porto, Portugal, 2018, pp. 1–5.

[79] Y. Wang and H. Leib, "Sphere decoding for MIMO systems with Newton iterative matrix inversion," *IEEE Commun. Lett.*, vol. 17, no. 2, pp. 389–392, 2013.

[80] X. Qin, Z. Yan, and G. He, "A near-optimal detection scheme based on joint steepest descent and Jacobi method for uplink massive MIMO systems," *IEEE Commun. Lett.*, vol. 20, no. 2, pp. 276–279, 2016.

[81] J. Minango, C. de Almeida, and C. D. Altamirano, "Low-complexity MMSE detector for massive MIMO systems based on damped Jacobi method," in *Proc. IEEE 28th Annu. Int. Symp. Pers., Indoor Mobile Radio Commun. (PIMRC)*, Montreal, Canada, 2017, pp. 1–5.

[82] L. Dai *et al.*, "Low-complexity soft-output detection based on Gauss–Seidel method for uplink multiuser large-scale MIMO systems," *IEEE Trans. Veh. Technol.*, vol. 64, no. 10, pp. 4839–4845, 2015.

[83] J. Minango and C. de Almeida, "Low complexity zero forcing detector based on Newton-Schultz iterative algorithm for massive MIMO systems," *IEEE Trans. Veh. Technol.*, vol. 67, no. 12, pp. 11 759–11 766, 2018.

[84] C. Tang *et al.*, "High precision low complexity matrix inversion based on Newton iteration for data detection in the massive MIMO," *IEEE Commun. Lett.*, vol. 20, no. 3, pp. 490–493, 2016.

[85] F. Khaksar Haghani and F. Soleymani, "An improved Schulz-type iterative method for matrix inversion with application," *Trans. Inst. Meas. Control*, vol. 36, no. 8, pp. 983–991, 2014.

[86] J. Minango and C. de Almeida, "Hyper-power zero forcing detector for massive MIMO systems," *Wireless Netw.*, vol. 25, no. 7, pp. 4349–4357, 2019.

[87] I. Ahmed *et al.*, "A survey on hybrid beamforming techniques in 5G: Architecture and system model perspectives," *IEEE Commun. Surveys Tuts.*, vol. 20, no. 4, pp. 3060–3097, 2018.

[88] C. G. Tsinos, S. Maleki, S. Chatzinotas, and B. Ottersten, "On the energy-efficiency of hybrid analog–digital transceivers for single- and multi-carrier large antenna array systems," *IEEE J. Sel. Areas Commun.*, vol. 35, no. 9, pp. 1980–1995, 2017.

[89] M. A. Sedaghat, R. R. Müller, and G. Fischer, "A novel single-RF transmitter for massive MIMO," in *Proc. 18th Int. ITG Workshop on Smart Antennas,* Erlangen, Germany, 2014, pp. 1–8.

[90] M. A. Sedaghat, V. I. Barousis, R. R. Müller, and C. B. Papadias, "Load modulated arrays: A low-complexity antenna," *IEEE Commun. Mag.*, vol. 54, no. 3, pp. 46–52, 2016.

[91] R. R. Müller, M. A. Sedaghat, and G. Fischer, "Load modulated massive MIMO," in *Proc. 2014 IEEE Global Conf. Signal Inf. Process.,* Atlanta, GA, USA, 2014, pp. 622–626.

[92] M. A. Sedaghat, R. R. Müller, G. Fischer, and A. Ali, "Discrete load-modulated single-RF MIMO transmitters," in *Proc. 20th Int. ITG Workshop on Smart Antennas,* Munich, Germany, 2016, pp. 260–266.

[93] S. C. Cripps, *RF Power Amplifiers for Wireless Communications*, 2nd ed. Boston, MA, USA: Artech House, 2006.

[94] S.-E. Hong and K.-S. Oh, "A comparison of ESPAR-MIMO and LMA-MIMO for single-RF transmission of spatially multiplexed QAM signals," in *Proc. 2017 IEEE Int. Conf. Consum. Electron. (ICCE),* Las Vegas, NV, USA, 2017, pp. 133–134.

[95] J. Oh, H. Kim, S. Cho, and G. Jo, "A single RF-chain load modulation transmitter of simple structure for massive MIMO," in *Proc. 2017 Int. Conf. Inf. Commun. Technol. Convergence (ICTC),* Jeju, South Korea, 2017, pp. 954–956.

[96] S. Bhat and A. Chockalingam, "LSE precoder for load modulated arrays with channel modulation," *IEEE Wireless Commun. Lett.*, vol. 9, no. 8, pp. 1295–1299, 2020.

[97] S. Bhat and A. Chockalingam, "Load modulated arrays using channel modulation with RF mirrors," in *Proc. 2019 IEEE 89th Veh. Technol. Conf. (VTC Spring),* Kuala Lumpur, Malaysia, 2019, pp. 1–5.

[98] G. Interdonato, H. Q. Ngo, and E. G. Larsson, "Enhanced normalized conjugate beamforming for cell-free massive MIMO," *IEEE Trans. Commun.*, vol. 69, no. 5, pp. 2863–2877, 2021.

[99] E. Björnson and L. Sanguinetti, "Scalable cell-free massive MIMO systems," *IEEE Trans. Commun.*, vol. 68, no. 7, pp. 4247–4261, 2020.

[100] H. Q. Ngo, L. Tran, T. Q. Duong, M. Matthaiou, and E. G. Larsson, "On the total energy efficiency of cell-free massive MIMO," *IEEE Trans. Green Commun. Netw.*, vol. 2, no. 1, pp. 25–39, 2018.

[101] H. T. Dao and S. Kim, "Effective channel gain-based access point selection in cell-free massive MIMO systems," *IEEE Access*, vol. 8, pp. 108 127–108 132, 2020.

[102] S. Biswas and P. Vijayakumar, "AP selection in cell-free massive MIMO system using machine learning algorithm," in *Proc. 2021 IEEE 6th Wireless Communications, Signal Processing and Networking Conf. (WiSPNET)*, 2021, pp. 158–161.

[103] V. Ranasinghe, N. Rajatheva, and M. Latva-aho, "Graph neural network based access point selection for cell-free massive MIMO systems," in *Proc. 2021 IEEE Global Commun. Conf. (GLOBECOM)*, 2021, pp. 01–06.

[104] H. Q. Ngo, L.-N. Tran, T. Q. Duong, M. Matthaiou, and E. G. Larsson, "On the total energy efficiency of cell-free massive MIMO," *IEEE Trans. Green Commun. Netw.*, vol. 2, no. 1, pp. 25–39, 2018.

[105] G. Amarasuriya, E. G. Larsson, and H. V. Poor, "Wireless information and power transfer in multiway massive MIMO relay networks," *IEEE Trans. Wireless Commun.*, vol. 15, no. 6, pp. 3837–3855, 2016.

[106] M. Agiwal, A. Roy, and N. Saxena, "Next generation 5G wireless networks: A comprehensive survey," *IEEE Commun. Surveys Tuts.*, vol. 18, no. 3, pp. 1617–1655, 2016.

[107] M. Peng, K. Zhang, J. Jiang, J. Wang, and W. Wang, "Energy-efficient resource assignment and power allocation in heterogeneous cloud radio access networks," *IEEE Trans. Veh. Technol.*, vol. 64, no. 11, pp. 5275–5287, 2015.

[108] N.-T. Le, L.-N. Tran, Q.-D. Vu, and D. Jayalath, "Energy-efficient resource allocation for OFDMA heterogeneous networks," *IEEE Trans. Commun.*, vol. 67, no. 10, pp. 7043–7057, 2019.

[109] M. R. Mili, A. Khalili, D. W. K. Ng, and H. Steendam, "A novel performance tradeoff in heterogeneous networks: A multi-objective approach," *IEEE Wireless Commun. Lett.*, vol. 8, no. 5, pp. 1402–1405, 2019.

[110] L. D. Nguyen, H. D. Tuan, T. Q. Duong, O. A. Dobre, and H. V. Poor, "Downlink beamforming for energy-efficient heterogeneous networks with massive MIMO and small cells," *IEEE Trans. Wireless Commun.*, vol. 17, no. 5, pp. 3386–3400, 2018.

[111] Q.-D. Vu, L.-N. Tran, R. Farrell, and E.-K. Hong, "Energy-efficient zero-forcing precoding design for small-cell networks," *IEEE Trans. Commun.*, vol. 64, no. 2, pp. 790–804, 2016.

[112] Y. Kwon, T. Hwang, and X. Wang, "Energy-efficient transmit power control for multi-tier MIMO HetNets," *IEEE J. Sel. Areas Commun.*, vol. 33, no. 10, pp. 2070–2086, 2015.

[113] J. Tang, D. K. C. So, A. Shojaeifard, K.-K. Wong, and J. Wen, "Joint antenna selection and spatial switching for energy efficient MIMO SWIPT system," *IEEE Trans. Wireless Commun.*, vol. 16, no. 7, pp. 4754–4769, 2017.

[114] H. Li, J. Cheng, Z. Wang, and H. Wang, "Joint antenna selection and power allocation for an energy-efficient massive MIMO system," *IEEE Wireless Commun. Lett.*, vol. 8, no. 1, pp. 257–260, 2019, ISSN: 2162–2337. DOI: 10.1109/LWC.2018.2869152.

[115] B. Huang and A. Guo, "Spectral and energy efficient resource allocation for massive MIMO HetNets with wireless backhaul," *IEEE Wireless Commun. Lett.*, vol. 8, no. 2, pp. 552–555, 2019.

[116] X. Wu, Z. Ma, X. Chen, F. Labeau, and S. Han, "Energy efficiency-aware joint resource allocation and power allocation in multi-user beamforming," *IEEE Trans. Veh. Technol.*, vol. 68, no. 5, pp. 4824–4833, 2019.

[117] G. Dong, H. Zhang, S. Jin, and D. Yuan, "Energy-efficiency-oriented joint user association and power allocation in distributed massive MIMO systems," *IEEE Trans. Veh. Technol.*, vol. 68, no. 6, pp. 5794–5808, 2019, ISSN: 1939-9359.

[118] A. Liu and V. K. N. Lau, "Joint BS-user association, power allocation, and user-side interference cancellation in cell-free heterogeneous networks," *IEEE Trans. Signal Process.*, vol. 65, no. 2, pp. 335–345, 2017, ISSN: 1941-0476.

[119] B. Dai and W. Yu, "Sparse beamforming and user-centric clustering for downlink cloud radio access network," *IEEE Access*, vol. 2, pp. 1326–1339, 2014.

[120] D. Ha, K. Lee, and J. Kang, "Energy efficiency analysis with circuit power consumption in massive MIMO systems," in *Proc. 2013 IEEE 24th Annu. Int. Symp. Pers., Indoor Mobile Radio Commun. (PIMRC)*, London, UK, Sept. 2013, pp. 938–942.

[121] P. Viswanath, D. N. C. Tse, and R. Laroia, "Opportunistic beamforming using dumb antennas," *IEEE Trans. Inf. Theory*, vol. 48, no. 6, pp. 1277–1294, 2002.

[122] F. P. Kelly, A. K. Maulloo, and D. K. H. Tan, "Rate control for communication networks: Shadow prices, proportional fairness and stability," *J. Oper. Res. Soc.*, vol. 49, no. 3, pp. 237–252, 1998.

[123] Q. H. Spencer, A. L. Swindlehurst, and M. Haardt, "Zero-forcing methods for downlink spatial multiplexing in multiuser MIMO channels," *IEEE Trans. Signal Process.*, vol. 52, no. 2, pp. 461–471, 2004.

[124] W. Hao and S. Yang, "Small cell cluster-based resource allocation for wireless backhaul in two-tier heterogeneous networks with massive MIMO," *IEEE Trans. Veh. Technol.*, vol. 67, no. 1, pp. 509–523, 2018.

[125] W. Dinkelbach, "On nonlinear fractional programming," *Manag. Sci.*, vol. 13, no. 7, pp. 492–498, 1967.

[126] A. Zappone, L. Sanguinetti, G. Bacci, E. Jorswieck, and M. Debbah, "Energy-efficient power control: A look at 5G wireless technologies," *IEEE Trans. Signal Process.*, vol. 64, no. 7, pp. 1668–1683, 2016.

[127] S. Boyd and L. Vandenberghe, "Convex optimization.," in *Convex Optimization*. Cambridge, UK: Cambridge Univ. Press, 2004.

[128] K. T. K. Cheung, S. Yang, and L. Hanzo, "Achieving maximum energy-efficiency in multi-relay OFDMA cellular networks: A fractional programming approach," *IEEE Trans. Commun.*, vol. 61, no. 7, pp. 2746–2757, 2013.

[129] W. Yu and R. Lui, "Dual methods for nonconvex spectrum optimization of multicarrier systems," *IEEE Trans. Commun.*, vol. 54, no. 7, pp. 1310–1322, 2006.

[130] J. G. Andrews, F. Baccelli, and R. K. Ganti, "A tractable approach to coverage and rate in cellular networks," *IEEE Trans. Commun.*, vol. 59, no. 11, pp. 3122–3134, 2011.

[131] Y. J. Chun, S. L. Cotton, H. S. Dhillon, F. J. Lopez-Martinez, J. F. Paris, and S. K. Yoo, "A comprehensive analysis of 5G heterogeneous cellular systems operating over κ-μ shadowed fading channels," *IEEE Trans. Wireless Commun.*, vol. 16, no. 11, pp. 6995–7010, 2017.

[132] V. Chandrasekhar, M. Kountouris, and J. G. Andrews, "Coverage in multi-antenna two-tier networks," *IEEE Trans. Wireless Commun.*, vol. 8, no. 10, pp. 5314–5327, 2009.

[133] H.-S. Jo, Y. J. Sang, P. Xia, and J. G. Andrews, "Heterogeneous cellular networks with flexible cell association: A comprehensive downlink SINR analysis," *IEEE Trans. Wireless Commun.*, vol. 11, no. 10, pp. 3484–3495, 2012.

[134] K. Hosseini, W. Yu, and R. S. Adve, "Large-scale MIMO versus network MIMO for multicell interference mitigation," *IEEE J. Sel. Topics. Signal Process.*, vol. 8, no. 5, pp. 930–941, 2014.

[135] "Evolved universal terrestrial radio access (E-UTRA); Further advancements for E-UTRA physical layer aspects (release 9)," 3rd Generation Partnership Project, Tech. Rep. 3GPP TR 36.814 v9.2.0, 2017.

[136] A. Mesodiakaki, F. Adelantado, L. Alonso, M. Di Renzo, and C. Verikoukis, "Energy- and spectrum-efficient user association in millimeter-wave backhaul small-cell networks," *IEEE Trans. Veh. Technol.*, vol. 66, no. 2, pp. 1810–1821, 2017, ISSN: 1939–9359. DOI: 10.1109/TVT.2016.2565539.

[137] J. Minango and C. de Almeida, "Low complexity zero forcing detector based on Newton-Schultz iterative algorithm for massive MIMO systems," *IEEE Trans. Veh. Technol.*, vol. 67, no. 12, pp. 11 759–11 766, 2018.

[138] E. Nayebi *et al.*, "Precoding and power optimization in cell-free massive MIMO systems," *IEEE Trans. Wireless Commun.*, vol. 16, no. 7, pp. 4445–4459, 2017.

[139] R. Bagnara, "A unified proof for the convergence of Jacobi and Gauss–Seidel methods," *SIAM Rev.*, vol. 37, no. 1, pp. 93–97, 1995.

[140] E. Björnson and L. Sanguinetti, "Making cell-free massive MIMO competitive with MMSE processing and centralized implementation," *IEEE Trans. Wireless Commun.*, vol. 19, no. 1, pp. 77–90, 2020.

[141] A. Quarteroni, R. Sacco, and F. Saleri, *Numerical Mathematics*, 2nd ed. Berlin, Germany: Springer, 2006.

[142] X. Qiao, Y. Zhang, and L. Yang, "Conjugate gradient method based linear precoding with low-complexity for massive MIMO systems," in *Proc. IEEE 4th Int. Conf. Comput. Commun. (ICCC)*, Chengdu, China, 2018, pp. 420–424.

[143] A. Ben-Israel, "An iterative method for computing the generalized inverse of an arbitrary matrix," *Math. Comput.*, vol. 19, no. 91, pp. 452–455, 1965.

[144] M. D. Petković and M. S. Petković, "Hyper-power methods for the computation of outer inverses," *J. Comput. Appl. Math.*, vol. 278, pp. 110–118, 2015.

[145] J. F. Traub, *Iterative Methods for the Solution of Equations*, 2nd ed. New York, NY, USA: Chelsea Publishing Co., 1982.

[146] A. Ben-Israel, "A note on an iterative method for generalized inversion of matrices," *Math. Comput.*, vol. 20, no. 95, pp. 439–440, 1966.

[147] A. Ben-Israel and D. Cohen, "On iterative computation of generalized inverses and associated projections," *SIAM J. Numer. Anal.,*, vol. 3, no. 3, pp. 410–419, 1966.

[148] V. Pan and R. Schreiber, "An improved Newton iteration for the generalized inverse of a matrix, with applications," *SIAM J. Scientific Statist. Comput.*, vol. 12, no. 5, pp. 1109–1130, 1991.

[149] H. Wolkowicz and G. P. H. Styan, "Bounds for eigenvalues using traces," *Linear Algebra and its Appl.*, vol. 29, 471—506, 1980.

[150] R. Sharma, R. Kumar, and R. Saini, "Note on bounds for eigenvalues using traces," *arXiv*, pp. 1–13, 2014. [Online]. Available: https://arxiv.org/abs/1409.0096.

[151] W. V. Petryshyn, "On generalized inverses and on the uniform convergence of $(I-\beta K)^n$ with application to iterative methods," *J. Math. Anal. Appl.*, vol. 18, no. 3, pp. 417–439, 1967.

[152] A. Ben-Israel and T. N. E. Greville, *Generalized Inverses: Theory and Applications*, 2nd ed. New York, NY, USA: Springer-Verlag, 2003.

[153] F. Soleymani, P. S. Stanimirović, and F. Khaksar Haghani, "On hyperpower family of iterations for computing outer inverses possessing high efficiencies," *Linear Algebra and its Appl.*, vol. 484, pp. 477–495, 2015.

[154] M. Sharifi, M. Arab, and F. Khaksar Haghani, "Finding generalized inverses by a fast and efficient numerical method," *J. Comput. Appl. Math.*, vol. 279, pp. 187–191, 2015.

[155] V. Y. Pan, F. Soleymani, and L. Zhao, "An efficient computation of generalized inverse of a matrix," *Appl. Math. Comput.*, vol. 316, pp. 89–101, 2018.

[156] M. D. Petković, M. A. Krstić, and K. P. Rajković, "Rapid generalized Schultz iterative methods for the computation of outer inverses," *J. Comput. Appl. Math.*, vol. 344, pp. 572–584, 2018.

[157] A. Kumar *et al.*, "Factorizations of hyperpower family of iterative methods via least squares approach," *Comput. Appl. Math.*, vol. 37, no. 3, pp. 3226–3240, 2018.

[158] M. Kallio, A. Ruszczynski, and S. Salo, "A regularized Jacobi method for large-scale linear programming," Int. Inst. Appl. Syst. Appl. (IIASA), Laxenburg, Austria, Working Paper WP-93-061, 1993. [Online]. Available: http://pure.iiasa.ac.at/id/eprint/3753/.

[159] R. Hunger, "Floating point operations in matrix-vector calculus," Technische Universität München, Associate Institute for Signal Processing, Tech. Rep., 2007. [Online]. Available: https://mediatum.ub.tum.de/doc/625604/625604.

[160] H. Chen, G. Yang, and Y.-C. Liang, "Joint active and passive beamforming for reconfigurable intelligent surface enhanced symbiotic radio system," *IEEE Wireless Commun. Lett.*, vol. 10, no. 5, pp. 1056–1060, 2021.

[161] T. Wu, M. Jiang, Q. Zhang, Q. Li, and J. Qin, "Beamforming design in multiple-input-multiple-output symbiotic radio backscatter systems," *IEEE Commun. Lett.*, vol. 25, no. 6, pp. 1949–1953, 2021.

[162] G. Yang, T. Wei, and Y.-C. Liang, "Joint hybrid and passive beamforming for millimeter wave symbiotic radio systems," *IEEE Wireless Commun. Lett.*, vol. 10, no. 10, pp. 2294–2298, 2021.

[163] H. Guo, Y.-C. Liang, R. Long, S. Xiao, and Q. Zhang, "Resource allocation for symbiotic radio system with fading channels," *IEEE Access*, vol. 7, pp. 34 333–34 347, 2019.

[164] Z. Dai, R. Li, J. Xu, Y. Zeng, and S. Jin, "Cell-free symbiotic radio: Channel estimation method and achievable rate analysis," in *2021 IEEE/CIC (ICCC Workshops)*, Xiamen, China, Jul. 2021, pp. 25–30.

[165] D. Mishra and G. C. Alexandropoulos, "Transmit precoding and receive power splitting for harvested power maximization in MIMO SWIPT systems," *IEEE Trans. Green Commun. Netw.*, vol. 2, no. 3, pp. 774–786, 2018.

[166] G. Interdonato, H. Q. Ngo, P. Frenger, and E. G. Larsson, "Downlink training in cell-free massive MIMO: A blessing in disguise," *IEEE Trans. Wireless Commun.*, vol. 18, no. 11, pp. 5153–5169, 2019.

[167] Y. Liu, G. Wang, Z. Dou, and Z. Zhong, "Coding and detection schemes for ambient backscatter communication systems," *IEEE Access*, vol. 5, pp. 4947–4953, 2017.

[168] H. Guo, R. Long, and Y.-C. Liang, "Cognitive backscatter network: A spectrum sharing paradigm for passive IoT," *IEEE Wireless Commun. Lett.*, vol. 8, no. 5, pp. 1423–1426, 2019.

[169] *Physical channels and modulation (release 17)*, Tech. Spec. 3rd Generation Partnership Project (3GPP), 2022.

[170] Q. Zhang, Y.-C. Liang, and H. V. Poor, "Reconfigurable intelligent surface assisted MIMO symbiotic radio networks," *IEEE Trans. Commun.*, vol. 69, no. 7, pp. 4832–4846, 2021.

[171] G. L. Stüber, *Principles of Mobile Communication*, 4th. Cham, Switzerland: Springer, 2017.

[172] J. G. Proakis and M. Salehi, *Digital Communications*, 5th. Boston, MA, USA: McGraw-Hill, 2008.

[173] J. Qian, F. Gao, G. Wang, S. Jin, and H. Zhu, "Noncoherent detections for ambient backscatter system," *IEEE Transactions on Wireless Communications*, vol. 16, no. 3, pp. 1412–1422, 2017. DOI: 10.1109/TWC.2016.2635654.

[174] S. Xiao, H. Guo, and Y. Liang, "Resource allocation for full-duplex-enabled cognitive backscatter networks," *IEEE Trans. Wireless Commun.*, vol. 18, no. 6, pp. 3222–3235, 2019.

[175] X. Lu, H. Jiang, D. Niyato, D. I. Kim, and Z. Han, "Wireless-powered device-to-device communications with ambient backscattering: Performance modeling and analysis," *IEEE Trans. Wireless Commun.*, vol. 17, no. 3, pp. 1528–1544, 2018.

[176] B. Lyu, C. You, Z. Yang, and G. Gui, "The optimal control policy for RF-powered backscatter communication networks," *IEEE Trans. Veh. Technol.*, vol. 67, no. 3, pp. 2804–2808, 2018.

[177] E. Björnson and L. Sanguinetti, "Making cell-free massive MIMO competitive with MMSE processing and centralized implementation," *IEEE Trans. Wireless Commun.*, vol. 19, no. 1, pp. 77–90, 2020.

[178] K. I. Pedersen, P. E. Mogensen, and B. H. Fleury, "Power azimuth spectrum in outdoor environments," *Electron. Lett.*, vol. 33, no. 18, pp. 1583–1584, 1997.

[179] X. Wang, X. Wang, and A. Ashikhmin, "Long-term scheduling and power control for wirelessly powered cell-free IoT," *IEEE Internet Things J.*, pp. 1–1, 2020.

[180] L. Lu, G. Y. Li, A. L. Swindlehurst, A. Ashikhmin, and R. Zhang, "An overview of massive MIMO: Benefits and challenges," *IEEE J. Sel. Areas Commun.*, vol. 8, no. 5, pp. 742–758, 2014.

[181] H. Q. Ngo, A. Ashikhmin, H. Yang, E. G. Larsson, and T. L. Marzetta, "Cell-free massive MIMO versus small cells," *IEEE Trans. Wireless Commun.*, vol. 16, no. 3, pp. 1834–1850, 2017, ISSN: 1558-2248.

Appendix A:

A.1 Proof for Lemma 1 of Chapter 3

One may consider the PPPs Φ_s and Φ_u to be uniformly distributed over the area A of a circle centered at the origin o of the plane and having radius R_A, where R_A tends to infinity. We consider the typical user $u \in \Phi_u$, who is served by BS $s \in \Phi_s$. Without loss of generality, we may consider this user to be located at the origin. The distribution of the distance $d_{s,u}$ from the user to its serving BS, i.e., the nearest point in Φ_s, is [130]

$$f_{d_{s,u}}(r) = 2\pi\lambda_s r \exp(-\pi\lambda_s r^2) \tag{A.1}$$

Meanwhile, the location of any other arbitrary BS $r \in \Phi_s \backslash s$ is independent of the location of s and uniformly distributed over A. Therefore, the distribution of the distance $d_{r,u}$ between r and the origin is

$$f_{d_{r,u}}(r) = \frac{2\pi r}{\pi R_A^2} = \frac{2r}{R_A^2} \tag{A.2}$$

Since u is served by s, $d_{r,u}$ must be larger than $d_{s,u}$. However, to be part of the cluster for u, from (3.26) we have that $d_{r,u}$ can be no larger than $\Delta d_{s,u}$. Therefore, the probability that an arbitrary BS r will be part of the cluster for u (but not serve u), conditioned on $d_{s,u}$, is $\mathbb{P}_u^{supp}|d_{s,u} = \mathbb{E}_{d_{r,u}}[\mathbb{1}(d_{s,u} < d_{r,u} \leq \Delta d_{s,u})|d_{s,u}]$, where $\mathbb{1}(x)$ is an indicator function that equals 1 if x is true, and 0 otherwise.

$$\begin{aligned} \mathbb{P}_u^{supp}|d_{s,u} &= \int_0^{\infty} \mathbb{1}(d_{s,u} < d_{r,u} \leq \Delta d_{s,u})\ f_{d_{r,u}}(r)\mathrm{d}r \\ &= \int_{d_{s,u}}^{\Delta d_{s,u}} \frac{2r}{R_A^2}\mathrm{d}r = \frac{d_{s,u}^2(\Delta^2 - 1)}{R_A^2} \end{aligned} \tag{A.3}$$

Then, deconditioning on $d_{s,u}$ to obtain $p_u^{supp} = \mathbb{E}_{d_{s,u}}[\mathbb{P}_u^{supp}|d_{s,u}]$:

$$\begin{aligned} p_u^{supp} &= \int_0^\infty \mathbb{P}_u^{supp}|d_{s,u}\ f_{d_{s,u}}(r)\mathrm{d}r \\ &= \int_0^\infty \frac{r^2(\Delta^2-1)}{R_A^2} 2\pi\lambda_s r \exp(-\pi\lambda_s r^2)\mathrm{d}r \\ &= \frac{(\Delta^2-1)}{\pi\lambda_s R_A^2} \end{aligned} \tag{A.4}$$

p_u^{supp} is the probability of supporting, but not serving, some typical user u. (This would be a user in the set $\mathcal{I}_s$.) However, there are a total of N_U users uniformly distributed over A, where N_U is a Poisson-distributed random variable with mean $\lambda_u \pi R_A^2$. Each user is independently placed, meaning the statistics for any given user are identical. (When considering some other user, without loss of generality one can relocate the origin of the infinite plane to that user's location and thus obtain the same probability.) Consequently, the probability of supporting (but not serving) n out of N_U users is a binomial-distributed random variable:

$$\mathbb{P}[I_s = n|N_U] = \binom{N_U}{n} (p_u^{supp})^n (1-p_u^{supp})^{N_U-n} \tag{A.5}$$

The mean value of I_s is

$$\begin{aligned} \mathbb{E}[I_s] &= \mathbb{E}_{N_U,n}\{\mathbb{P}[I_s{=}n|N_U]\} = \mathbb{E}_{N_U}[\mathbb{E}_n\{\mathbb{P}[I_s{=}n|N_U]\}] \\ &= \mathbb{E}_{N_U}[N_U p_u^{supp}] = \lambda_u \pi R_A^2 p_u^{supp} \\ &= \lambda_u \pi R_A^2 \frac{(\Delta^2-1)}{\pi\lambda_s R_A^2} = (\Delta^2-1)\frac{\lambda_u}{\lambda_s} \end{aligned} \tag{A.6}$$

The mean value of the number of served users per BS, $\mathbb{E}[K_s]$, is known to be λ_u/λ_s [133]. Since $\mathcal{K}_s$ and $\mathcal{I}_s$ are disjoint, the mean number of supported users (served and clustered) $\mathbb{E}[L_s]$ in $\mathcal{L}_s$ is just the sum of $\mathbb{E}[K_s]$ and $\mathbb{E}[I_s]$. Therefore:

$$\begin{aligned} \mathbb{E}[L_s] &= \mathbb{E}[K_s] + \mathbb{E}[I_s] \\ &= (\Delta^2-1)\frac{\lambda_u}{\lambda_s} + \frac{\lambda_u}{\lambda_s} = \Delta^2\frac{\lambda_u}{\lambda_s}, \end{aligned} \tag{A.7}$$

which completes the proof.

Appendix B:

B.1 Derivations for Second Phase of Channel Estimation of Chapter 5

To find the covariance of $\mathbf{z}'_{nk}$, we have

$$\begin{aligned}
\boldsymbol{\Phi}'_{nk} &= \mathbb{E}\{\mathbf{z}'_{nk}\mathbf{z}'^{H}_{nk}\} = \mathbb{E}\Bigg\{\Bigg[\sqrt{\rho_{k,2}\tau_2}(\tilde{\mathbf{g}}_{b_n u_k} + \mathbf{g}_{b_n t_k u_k}) + \sum_{\ell\in\{\mathcal{S}_k\setminus k\}}\sqrt{\rho_{\ell,2}\tau_2}(\mathbf{g}_{b_n u_\ell} + \mathbf{g}_{b_n t_\ell u_\ell}) + \mathbf{n}'_{nk}\Bigg]\times \\
&\quad \Bigg[\sqrt{\rho_{k,2}\tau_2}(\tilde{\mathbf{g}}^H_{b_n u_k} + \mathbf{g}^H_{b_n t_k u_k}) + \sum_{\ell\in\{\mathcal{S}_k\setminus k\}}\sqrt{\rho_{\ell,2}\tau_2}(\mathbf{g}^H_{b_n u_\ell} + \mathbf{g}^H_{b_n t_\ell u_\ell}) + \mathbf{n}'^{H}_{nk}\Bigg]\Bigg\} \\
&= \rho_{k,2}\tau_2\big[\mathbb{E}\{\tilde{\mathbf{g}}_{b_n u_k}\tilde{\mathbf{g}}^H_{b_n u_k}\} + \mathbb{E}\{\mathbf{g}_{b_n t_k u_k}\mathbf{g}^H_{b_n t_k u_k}\}\big] + \sum_{\ell\in\{\mathcal{S}_k\setminus k\}}\rho_{\ell,2}\tau_2\big[\mathbb{E}\{\mathbf{g}_{b_n u_\ell}\mathbf{g}^H_{b_n u_\ell}\} + \mathbb{E}\{\mathbf{g}_{b_n t_\ell u_\ell}\mathbf{g}^H_{b_n t_\ell u_\ell}\}\big] \\
&\quad + \tau_2\sum_{\ell\in\{\mathcal{S}_k\setminus k\}}\sqrt{\rho_{k,2}\rho_{\ell,2}}\left[\mathbb{E}\{\tilde{\mathbf{g}}_{b_n u_k}\mathbf{g}^H_{b_n u_\ell}\} + \mathbb{E}\{\mathbf{g}_{b_n u_\ell}\tilde{\mathbf{g}}^H_{b_n u_k}\}\right] + \mathbb{E}\{\mathbf{n}'_{nk}\mathbf{n}'^{H}_{nk}\} \\
&= \rho_{k,2}\tau_2(\tilde{\mathbf{R}}_{b_n u_k} + \mathbf{R}_{b_n t_k u_k}) + \sum_{\ell\in\{\mathcal{S}_k\setminus k\}}\rho_{\ell,2}\tau_2(\mathbf{R}_{b_n u_\ell} + \mathbf{R}_{b_n t_\ell u_\ell}) \\
&\quad + \tau_2\sum_{\ell\in\{\mathcal{S}_k\setminus k\}}\sqrt{\rho_{k,2}\rho_{\ell,2}}\left(\mathbb{E}\{\tilde{\mathbf{g}}_{b_n u_k}\mathbf{g}^H_{b_n u_\ell} + \mathbf{g}_{b_n u_\ell}\tilde{\mathbf{g}}^H_{b_n u_k}\}\right) + \sigma_n^2\mathbf{I}_L.
\end{aligned} \tag{B.1}$$

Due to pilot contamination, there is a correlation between the channel estimates $\hat{\mathbf{g}}_{b_n u_{k'}}$ for any PRs $k' \in \mathcal{S}_k$ sharing the same pilot sequence, and consequently a correlation between $\tilde{\mathbf{g}}_{b_n u_k}$ and $\mathbf{g}_{b_n u_\ell}$, $k \neq \ell$. Hence, we have

$$\begin{aligned}
\mathbb{E}\{\tilde{\mathbf{g}}_{b_n u_k}\mathbf{g}^H_{b_n u_\ell}\} &= \mathbb{E}\{(\mathbf{g}_{b_n u_k} - \hat{\mathbf{g}}_{b_n u_k})\mathbf{g}^H_{b_n u_\ell}\} = -\mathbb{E}\{\hat{\mathbf{g}}_{b_n u_k}\mathbf{g}^H_{b_n u_\ell}\} = -\mathbb{E}\{\sqrt{\rho_{k,1}\tau_1}\,\mathbf{R}_{b_n u_k}\boldsymbol{\Theta}^{-1}_{nk}\mathbf{y}_{nk}\mathbf{g}^H_{b_n u_\ell}\} \\
&= -\sqrt{\rho_{k,1}\tau_1}\,\mathbb{E}\Big\{\mathbf{R}_{b_n u_k}\boldsymbol{\Theta}^{-1}_{nk}\Big(\sum_{k'\in\mathcal{S}_k}\sqrt{\rho_{k',1}\tau_1}\,\mathbf{g}_{b_n u_{k'}} + \mathbf{n}_{nk}\Big)\mathbf{g}^H_{b_n u_\ell}\Big\} \\
&= -\sqrt{\rho_{k,1}\tau_1}\,\mathbb{E}\Big\{\mathbf{R}_{b_n u_k}\boldsymbol{\Theta}^{-1}_{nk}\Big(\sqrt{\rho_{\ell,1}\tau_1}\,\mathbf{g}_{b_n u_\ell}\mathbf{g}^H_{b_n u_\ell} + \sum_{k'\in\{\mathcal{S}_k\setminus\ell\}}\sqrt{\rho_{k',1}\tau_1}\,\mathbf{g}_{b_n u_{k'}}\mathbf{g}^H_{b_n u_\ell} + \mathbf{n}_{nk}\mathbf{g}^H_{b_n u_\ell}\Big)\Big\} \\
&= -\tau_1\sqrt{\rho_{k,1}\rho_{\ell,1}}\,\mathbf{R}_{b_n u_k}\boldsymbol{\Theta}^{-1}_{nk}\mathbf{R}_{b_n u_\ell}.
\end{aligned} \tag{B.2}$$

Similarly, we have

$$\mathbb{E}\{\mathbf{g}_{\mathbf{b_n u_\ell}}\tilde{\mathbf{g}}_{b_n u_k}^H\} = -\tau_1\sqrt{\rho_{k,1}\rho_{\ell,1}}\,\mathbf{R}_{b_n u_\ell}\boldsymbol{\Theta}_{nk}^{-1}\mathbf{R}_{b_n u_k}. \tag{B.3}$$

Substituting (B.2) and (B.3) into the last line of (B.1) gives the result in (5.12).

B.2 SINR Derivation of Primary Transmissions

Rearranging (5.19) to combine S_1 with S_2 and R_1 with R_2, and neglecting X_2, we have

$$y_k = \underbrace{\sum_{n\in\mathcal{A}_k}\sqrt{p_t\eta_{nk}}(\mathbf{g}_{b_n u_k}^H + \sqrt{\alpha_{t_k}}\mathbf{g}_{b_n t_k u_k}^H s_{t_k})\mathbf{w}_{nk}s_k}_{A} + \underbrace{\sum_{n=1}^{N}\sum_{\substack{\ell\in\mathcal{U}_n,\\ \ell\neq k}}\sqrt{p_t\eta_{n\ell}}(\mathbf{g}_{b_n u_k}^H + \sqrt{\alpha_{t_k}}\mathbf{g}_{b_n t_k u_k}^H s_{t_k})\mathbf{w}_{n\ell}s_\ell}_{B\text{: multiuser interference}} + n_k \tag{B.4}$$

Recall that the precoding at the APs uses estimated channel vectors, and that the PRs have only statistical CSI. As a consequence, part A in (B.4) can be decomposed as

$$A = \underbrace{\sum_{n\in\mathcal{A}_k}\sqrt{p_t\eta_{nk}}\big(\mathbb{E}\{\hat{\mathbf{g}}_{b_n u_k}^H\mathbf{w}_{nk}\} + \sqrt{\alpha_{t_k}}\,\mathbb{E}\{\hat{\mathbf{g}}_{b_n t_k u_k}^H\mathbf{w}_{nk}\}s_{t_k}\big)s_k}_{a_1\text{: useful signal}} + \underbrace{\sum_{n\in\mathcal{A}_k}\sqrt{p_t\eta_{nk}}(\tilde{\mathbf{g}}_{b_n u_k}^H + \sqrt{\alpha_{t_k}}\,\tilde{\mathbf{g}}_{b_n t_k u_k}^H s_{t_k})\mathbf{w}_{nk}s_k}_{a_2\text{: channel estimation error}}$$
$$+ \underbrace{\sum_{n\in\mathcal{A}_k}\sqrt{p_t\eta_{nk}}\Big[\big(\hat{\mathbf{g}}_{b_n u_k}^H\mathbf{w}_{nk} - \mathbb{E}\{\hat{\mathbf{g}}_{b_n u_k}^H\mathbf{w}_{nk}\}\big) + \sqrt{\alpha_{t_k}}\big(\hat{\mathbf{g}}_{b_n t_k u_k}^H\mathbf{w}_{nk} - \mathbb{E}\{\hat{\mathbf{g}}_{b_n t_k u_k}^H\mathbf{w}_{nk}\}\big)s_{t_k}\Big]s_k}_{a_3\text{: lack of instantaneous channel knowledge at PR}} \tag{B.5}$$

Meanwhile, B can be decomposed as

$$B = \underbrace{\sum_{n=1}^{N}\sum_{\substack{\ell\in\mathcal{U}_n,\\ \ell\neq k}}\sqrt{p_t\eta_{n\ell}}\mathbf{g}_{b_n u_k}^H\mathbf{w}_{n\ell}s_\ell}_{R_1\text{: interference from direct-link channels}} + \underbrace{\sum_{n=1}^{N}\sum_{\substack{\ell\in\mathcal{U}_n,\\ \ell\neq k}}\sqrt{p_t\eta_{n\ell}\alpha_{t_k}}\mathbf{g}_{b_n t_k u_k}^H s_{t_k}\mathbf{w}_{n\ell}s_\ell}_{R_2\text{: interference from cascaded backscatter channels}} \tag{B.6}$$

To find a lower bound on the achievable direct-link data rate, we consider the fact that a_2, a_3, B, and n_k are all uncorrelated with each other. The mean squared magnitudes of the various terms are computed as follows. First, since $\hat{\mathbf{g}}_{b_n u_k}^H$ and $\hat{\mathbf{g}}_{b_n t_k u_k}^H$ are uncorrelated, the expectation terms in a_1 and a_3 can be reduced thusly:

$$\mathbb{E}\{\hat{\mathbf{g}}_{b_n u_k}^H \mathbf{w}_{nk}\} = \mathbb{E}\left\{\hat{\mathbf{g}}_{b_n u_k}^H \left(\frac{\mu_{1,nk}\,\hat{\mathbf{g}}_{b_n u_k}}{||\hat{\mathbf{g}}_{b_n u_k}||^2} + \frac{\mu_{2,nk}\,\hat{\mathbf{g}}_{b_n t_k u_k}}{||\hat{\mathbf{g}}_{b_n t_k u_k}||^2}\right)\right\} = \mu_{1,nk} \tag{B.7}$$

$$\mathbb{E}\{\hat{\mathbf{g}}_{b_n t_k u_k}^H \mathbf{w}_{nk}\} = \mathbb{E}\left\{\hat{\mathbf{g}}_{b_n t_k u_k}^H \left(\frac{\mu_{1,nk}\,\hat{\mathbf{g}}_{b_n u_k}}{||\hat{\mathbf{g}}_{b_n u_k}||^2} + \frac{\mu_{2,nk}\,\hat{\mathbf{g}}_{b_n t_k u_k}}{||\hat{\mathbf{g}}_{b_n t_k u_k}||^2}\right)\right\} = \mu_{2,nk} \tag{B.8}$$

Then,

$$\begin{aligned}\mathbb{E}\{|a_1|^2\} &= \mathbb{E}\left\{\left|\sum_{n\in\mathcal{A}_k}\sqrt{p_t\eta_{nk}}\left(\mu_{1,nk}+\sqrt{\alpha_{t_k}}\,\mu_{2,nk}s_{t_k}\right)s_k\right|^2\right\} \\ &= p_t\sum_{i\in\mathcal{A}_k}\sum_{j\in\mathcal{A}_k}\sqrt{\eta_{ik}\eta_{jk}}(\mu_{1,ik}\mu_{1,jk}^*+\alpha_{t_k}\mu_{2,ik}\mu_{2,jk}^*)\end{aligned} \tag{B.9}$$

For the remaining terms, we define variables $\hat{\mathbf{q}}_{b_n u_k} = \frac{\hat{\mathbf{g}}_{b_n u_k}}{||\hat{\mathbf{g}}_{b_n u_k}||^2}$ and $\hat{\mathbf{q}}_{b_n t_k u_k} = \frac{\hat{\mathbf{g}}_{b_n t_k u_k}}{||\hat{\mathbf{g}}_{b_n t_k u_k}||^2}$, and make use of the following two Lemmas:

Lemma 1 *If $\mathbf{x} \in \mathbb{C}^n$ is distributed $\sim \mathcal{CN}(0, \mathbf{R}_x)$, then $\mathbf{y} = \frac{\mathbf{x}}{||\mathbf{x}||^2}$ has zero mean and a probability density function (PDF) of*

$$f_{\mathbf{y}}(\mathbf{y}) = \frac{\exp\left(-\frac{\mathbf{y}^H}{\|\mathbf{y}\|^2}\mathbf{R}_x^{-1}\frac{\mathbf{y}}{\|\mathbf{y}\|^2}\right)}{\pi^n\|\mathbf{y}\|^{4n}\det(\mathbf{R}_x)} \tag{B.10}$$

Proof. We first convert the complex normal distribution to its equivalent real-valued normal distribution by vertically stacking the real part of $\mathbf{x}$ on top of its imaginary part to make vector $\mathbf{z} \in \mathbb{R}^{2n}$, and let $m = 2n$. The covariance matrix of $\mathbf{z}$ is $\mathbf{R}_z = \frac{1}{2}\begin{bmatrix}\Re\mathfrak{e}(\mathbf{R}_x) & -\Im\mathfrak{m}(\mathbf{R}_x)\\ \Im\mathfrak{m}(\mathbf{R}_x) & \Re\mathfrak{e}(\mathbf{R}_x)\end{bmatrix}$. The real-valued equivalent of $\mathbf{y}$ will therefore be $\mathbf{v} = \frac{\mathbf{z}}{\|\mathbf{z}\|^2}$. The equation transforming element z_i of $\mathbf{z}$ to element v_i of $\mathbf{v}$ is $v_i = u_i(z_1, z_2, \ldots, z_m) = z_i/\sum_{\forall i} z_i^2$. Similarly, the reverse transformation is given by $z_i = w_i(z_1, z_2, \ldots, z_m) = v_i/\sum_{\forall i} v_i^2$. Hence, in vector form, we have $\mathbf{z} = \frac{\mathbf{v}}{||\mathbf{v}||^2}$ (and thus $\mathbf{x} = \frac{\mathbf{y}}{||\mathbf{y}||^2}$).

The partial derivatives of the reverse equations are $\frac{\partial w_i}{\partial v_i} = \frac{v_1^2+v_2^2+\ldots-v_i^2+\ldots+v_m^2}{v_1^2+v_2^2+\ldots+v_m^2}$ (note the minus sign on the v_i^2 term in the numerator) and $\frac{\partial w_i}{\partial v_j} = \frac{-2v_iv_j}{v_1^2+v_2^2+\ldots+v_m^2}$ for $j \neq i$.

Hence, the Jacobian of the transformation is

$$|J| = \operatorname{abs}\det\begin{bmatrix} \frac{\partial w_1}{\partial v_1} & \frac{\partial w_1}{\partial v_2} & \dots & \frac{\partial w_1}{\partial v_m} \\ \frac{\partial w_2}{\partial v_1} & \frac{\partial w_2}{\partial v_2} & \dots & \frac{\partial w_2}{\partial v_m} \\ \vdots & \vdots & \ddots & \vdots \\ \frac{\partial w_m}{\partial v_1} & \frac{\partial w_m}{\partial v_2} & \dots & \frac{\partial w_m}{\partial v_m} \end{bmatrix} = \frac{1}{(v_1^2 + v_2^2 + \ldots + v_m^2)^m} = \frac{1}{\|\mathbf{v}\|^{2m}} \tag{B.11}$$

The PDF of $\mathbf{v}$ thus is

$$f_{\mathbf{v}}(\mathbf{v}) = |J| f_{\mathbf{z}}\left(\tfrac{\mathbf{v}}{\|\mathbf{v}\|^2}\right) = \frac{\exp\left(-\frac{1}{2}\frac{\mathbf{v}^T}{\|\mathbf{v}\|^2}\mathbf{R}_z^{-1}\frac{\mathbf{v}}{\|\mathbf{v}\|^2}\right)}{\|\mathbf{v}\|^{2m}\sqrt{(2\pi)^m \det(\mathbf{R}_z)}} \tag{B.12}$$

Note $\det(\mathbf{R}_z) = \frac{1}{2^m}(\det(\mathbf{R}_x))^2$. Converting the real-valued form in (B.12) back to a complex-valued form yields (B.10).

Trivially, if $\mathbf{x}$ has zero mean, dividing by its squared norm will not change the mean from being zero. More formally, $\mathbf{y} \cdot f_{\mathbf{y}}(\mathbf{y})$ is an odd function for both the real and imaginary parts of each element of $\mathbf{y}$. Hence, $\int_{\mathbb{C}^n} \mathbf{y} f_{\mathbf{y}}(\mathbf{y})\, d\mathbf{y} = 0$. ■

Lemma 2 *If* $\mathbf{x}$ *and* $\mathbf{y} \in \mathbb{C}^n$ *are related by* $\mathbf{y} = \mathbf{A}\mathbf{x} + \mathbf{v}$*, with* $\mathbf{x} \sim \mathcal{CN}(0, \mathbf{R}_x)$ *and* $\mathbf{v} \sim \mathcal{CN}(0, \mathbf{R}_v)$ *being uncorrelated and* $\mathbf{A} \in \mathbb{C}^{n\times n}$ *being constant, then the joinf PDF of* $\mathbf{x}$ *and* $\mathbf{z} = \frac{\mathbf{y}}{||\mathbf{y}||^2}$ *is*

$$f_{\mathbf{x},\mathbf{z}}(\mathbf{x}, \mathbf{z}) = \frac{\exp\left(-\left(\frac{\mathbf{z}}{\|\mathbf{z}\|^2} - \mathbf{A}\mathbf{x}\right)^H \mathbf{R}_v^{-1}\left(\frac{\mathbf{z}}{\|\mathbf{z}\|^2} - \mathbf{A}\mathbf{x}\right) - \mathbf{x}^H \mathbf{R}_x^{-1}\mathbf{x}\right)}{\pi^{2n}\|\mathbf{z}\|^{4n}\det(\mathbf{R}_v\mathbf{R}_x)} \tag{B.13}$$

Proof. The joint PDF of $\mathbf{x}$ and $\mathbf{y}$ is obtained by $f(\mathbf{x}, \mathbf{y}) = f(\mathbf{y}|\mathbf{x})f(\mathbf{x})$. Conditioned on knowing $\mathbf{x}$, the distribution of $\mathbf{y}|\mathbf{x}$ is complex Gaussian with mean $\mathbf{A}\mathbf{x}$ and covariance matrix $\mathbf{R}_v$. Conversion from $f(\mathbf{x}, \mathbf{y})$ to $f(\mathbf{x}, \mathbf{z})$ then proceeds in the same fashion as in the proof of Lemma 1. ■

We also note the following manipulation if vectors $\mathbf{a}$ and $\mathbf{b}$ are uncorrelated with covariance $\mathbf{R}_a$ and $\mathbf{R}_b$ respectively; this makes use of the properties $\mathbb{E}\{\operatorname{tr}(\cdot)\} = \operatorname{tr}(\mathbb{E}\{\cdot\})$ and $\operatorname{tr}(\mathbf{AB}) = \operatorname{tr}(\mathbf{BA})$ for matrices $\mathbf{A}$ and $\mathbf{B}$ having compatible dimensions.

$$\mathbb{E}\{\mathbf{a}^H\mathbf{b}\mathbf{b}^H\mathbf{a}\} = \mathbb{E}\{\operatorname{tr}(\mathbf{a}^H\mathbf{b}\mathbf{b}^H\mathbf{a})\} = \mathbb{E}\{\operatorname{tr}(\mathbf{a}\mathbf{a}^H\mathbf{b}\mathbf{b}^H)\} = \operatorname{tr}(\mathbb{E}\{\mathbf{a}\mathbf{a}^H\}\mathbb{E}\{\mathbf{b}\mathbf{b}^H\}) = \operatorname{tr}(\mathbf{R}_a\mathbf{R}_b) \tag{B.14}$$

Examination of (5.10) shows that $\mathbf{z}'_{nk}$ is a function of $\tilde{\mathbf{g}}_{b_n u_k}$. Therefore, $\tilde{\mathbf{g}}_{b_n u_k}$ and $\hat{\mathbf{g}}_{b_n t_k u_k}$ have some correlation in the calculation of (5.11), though that correlation will be small if the estimate $\hat{\mathbf{g}}_{b_n u_k}$ is good. (The quality of said estimate depends on the amount of pilot contamination in the system.) Replacing $\tilde{\mathbf{g}}_{b_n u_k}$ by $\mathbf{g}_{b_n u_k} - \hat{\mathbf{g}}_{b_n u_k}$ and $\hat{\mathbf{g}}_{b_n u_k}$ by (5.4), and combining the other independent vectors in (5.10) into one equivalent vector with the same overall distribution, (5.11) can be manipulated into the form $\hat{\mathbf{g}}_{b_n t_k u_k} = \mathbf{A}\mathbf{g}_{b_n u_k} + \mathbf{v}$ like in Lemma 2. Hence, the joint PDF of $\mathbf{g}_{b_n u_k}$ and $\hat{\mathbf{g}}_{b_n t_k u_k}$ can be written as in (B.13), where $\mathbf{R}_x = \mathbf{R}_{b_n u_k}$ and $\mathbf{A}$ and $\mathbf{R}_v$ are given by

$$\mathbf{A} = \rho_{k,2}\tau_2 \mathbf{R}_{b_n t_k u_k} \mathbf{\Phi}'^{-1}_{nk} (\mathbf{I}_L - \rho_{k,1}\tau_1 \mathbf{R}_{b_n u_k} \mathbf{\Theta}^{-1}_{nk}) \tag{B.15}$$

$$\mathbf{R}_v = \hat{\mathbf{R}}_{b_n t_k u_k} - \mathbf{A}\mathbf{R}_{b_n u_k}\mathbf{A}^H \tag{B.16}$$

Let the covariance matrix of $\hat{\mathbf{q}}_{b_n u_k}$ and $\hat{\mathbf{q}}_{b_n t_k u_k}$ be denoted as $\hat{\mathbf{Q}}_{b_n u_k}$ and $\hat{\mathbf{Q}}_{b_n t_k u_k}$, respectively. Unfortunately, obtaining a symbolic expression for these matrices using (B.10) is exceedingly difficult. Similar difficulty is experienced in obtaining the cross-covariance matrix between $\mathbf{g}_{b_n u_k}$ and $\hat{\mathbf{g}}_{b_n t_k u_k}$ using (B.13). Both equations are resistant to symbolic integration. However, one can instead do the integrations numerically[1] to obtain the desired covariance and cross-covariance matrices. Alternatively, estimates of the matrices can be obtained by averaging numerous samples of the channel vectors in question; this is how the system would obtain the covariance matrices of the channels in practice.

With the above PDFs and covariance matrices, $\mathbb{E}\{|a_2|^2\}$ and $\mathbb{E}\{|a_3|^2\}$ can be cal-

[1] In performing a numerical integration, care must be taken near the origin of the multi-dimensional space. Due to the singularity of the PDFs at $||\mathbf{y}||$ and $||\mathbf{z}|| = 0$, the value of the PDF changes rapidly near that singularity. Thus, the spacing between samples taken near the origin should be sufficiently small to capture this rapid change.

culated as

$$\begin{aligned}
\mathbb{E}\{|a_2|^2\} &= \mathbb{E}\Bigg\{ \sum_{n\in\mathcal{A}_k} p_t\eta_{nk}\big(\tilde{\mathbf{g}}^H_{b_n u_k}+\sqrt{\alpha_{t_k}}\,\tilde{\mathbf{g}}^H_{b_n t_k u_k}s_{t_k}\big)\mathbf{w}_{nk}s_k s_k^*\mathbf{w}_{nk}^H\big(s^*_{t_k}\tilde{\mathbf{g}}_{b_n t_k u_k}\sqrt{\alpha_{t_k}}+\tilde{\mathbf{g}}_{b_n u_k}\big) \\
&\quad + \sum_{i\in\mathcal{A}_k}\sum_{\substack{j\in\mathcal{A}_k,\\ j\neq i}} p_t\sqrt{\eta_{ik}\eta_{jk}}\big(\tilde{\mathbf{g}}^H_{b_i u_k}+\sqrt{\alpha_{t_k}}\,\tilde{\mathbf{g}}^H_{b_i t_k u_k}s_{t_k}\big)\mathbf{w}_{ik}s_k s_k^*\mathbf{w}_{jk}^H\big(s^*_{t_k}\tilde{\mathbf{g}}_{b_j t_k u_k}\sqrt{\alpha_{t_k}}+\tilde{\mathbf{g}}_{b_j u_k}\big)\Bigg\} \\
&= \mathbb{E}\Bigg\{ \sum_{n\in\mathcal{A}_k} p_t\eta_{nk}\big(\tilde{\mathbf{g}}^H_{b_n u_k}\mathbf{w}_{nk}\mathbf{w}_{nk}^H\tilde{\mathbf{g}}_{b_n u_k}+\alpha_{t_k}|s_{t_k}|^2\,\tilde{\mathbf{g}}^H_{b_n t_k u_k}\mathbf{w}_{nk}\mathbf{w}_{nk}^H\tilde{\mathbf{g}}_{b_n t_k u_k}\big) \\
&\quad +\sum_{i\in\mathcal{A}_k}\sum_{\substack{j\in\mathcal{A}_k,\\ j\neq i}} p_t\sqrt{\eta_{ik}\eta_{jk}}\big(\tilde{\mathbf{g}}^H_{b_i u_k}\mathbf{w}_{ik}\mathbf{w}_{jk}^H\tilde{\mathbf{g}}_{b_j u_k}+\alpha_{t_k}|s_{t_k}|^2\,\tilde{\mathbf{g}}^H_{b_i t_k u_k}\mathbf{w}_{ik}\mathbf{w}_{jk}^H\tilde{\mathbf{g}}_{b_j t_k u_k}\big)\Bigg\} \\
&= \sum_{n\in\mathcal{A}_k} p_t\eta_{nk}\Bigg(|\mu_{1,nk}|^2\Big[\mathrm{tr}(\tilde{\mathbf{R}}_{b_n u_k}\hat{\mathbf{Q}}_{b_n u_k})+\alpha_{t_k}\mathrm{tr}(\tilde{\mathbf{R}}_{b_n t_k u_k}\hat{\mathbf{Q}}_{b_n u_k})\Big] \\
&\quad + |\mu_{2,nk}|^2\Big[\mathbb{E}\{\tilde{\mathbf{g}}^H_{b_n u_k}\hat{\mathbf{q}}_{b_n t_k u_k}\hat{\mathbf{q}}^H_{b_n t_k u_k}\tilde{\mathbf{g}}_{b_n u_k}\}+\alpha_{t_k}\mathrm{tr}(\tilde{\mathbf{R}}_{b_n t_k u_k}\hat{\mathbf{Q}}_{b_n t_k u_k})\Big]\Bigg) \\
&\quad +\sum_{i\in\mathcal{A}_k}\sum_{\substack{j\in\mathcal{A}_k,\\ j\neq i}} p_t\sqrt{\eta_{ik}\eta_{jk}}\,\mu_{2,ik}\,\mu^*_{2,jk}\,\mathbb{E}\{\tilde{\mathbf{g}}^H_{b_i u_k}\hat{\mathbf{q}}_{b_i t_k u_k}\}\mathbb{E}\{\hat{\mathbf{q}}^H_{b_j t_k u_k}\tilde{\mathbf{g}}_{b_j u_k}\}
\end{aligned} \tag{B.17}$$

and

$$\begin{aligned}
\mathbb{E}\{|a_3|^2\} &= \sum_{i\in\mathcal{A}_k}\sum_{j\in\mathcal{A}_k} p_t\sqrt{\eta_{ik}\eta_{jk}}\Big(\mathbb{E}\{\hat{\mathbf{g}}^H_{b_i u_k}\mathbf{w}_{ik}\mathbf{w}_{jk}^H\hat{\mathbf{g}}_{b_j u_k}\}+\alpha_{t_k}\mathbb{E}\{\hat{\mathbf{g}}^H_{b_i t_k u_k}\mathbf{w}_{ik}\mathbf{w}_{jk}^H\hat{\mathbf{g}}_{b_j t_k u_k}\} \\
&\quad +\mu_{1,ik}\mu^*_{1,jk}+\alpha_{t_k}\mu_{1,ik}\mu^*_{1,jk}-\mathbb{E}\{\hat{\mathbf{g}}^H_{b_i u_k}\mathbf{w}_{ik}\}\mu^*_{1,jk}-\alpha_{t_k}\mathbb{E}\{\hat{\mathbf{g}}^H_{b_i t_k u_k}\mathbf{w}_{ik}\}\mu^*_{2,jk} \\
&\quad -\mu_{1,ik}\mathbb{E}\{\mathbf{w}_{jk}^H\hat{\mathbf{g}}_{b_j u_k}\}-\alpha_{t_k}\mu_{2,ik}\mathbb{E}\{\mathbf{w}_{jk}\hat{\mathbf{g}}^H_{b_j t_k u_k}\}\Big) \\
&= \sum_{n\in\mathcal{A}_k} p_t\eta_{nk}\Big(\mathbb{E}\{\hat{\mathbf{g}}^H_{b_n u_k}\mathbf{w}_{nk}\mathbf{w}_{nk}^H\hat{\mathbf{g}}_{b_n u_k}\}+\alpha_{t_k}\mathbb{E}\{\hat{\mathbf{g}}^H_{b_n t_k u_k}\mathbf{w}_{nk}\mathbf{w}_{nk}^H\hat{\mathbf{g}}_{b_n t_k u_k}\}-|\mu_{1,nk}|^2-\alpha_{t_k}|\mu_{2,nk}|^2\Big) \\
&= \sum_{n\in\mathcal{A}_k} p_t\eta_{nk}\Big(\alpha_{t_k}|\mu_{1,nk}|^2\mathrm{tr}(\hat{\mathbf{R}}_{b_n t_k u_k}\hat{\mathbf{Q}}_{b_n u_k})+|\mu_{2,nk}|^2\mathrm{tr}(\hat{\mathbf{R}}_{b_n u_k}\hat{\mathbf{Q}}_{b_n t_k u_k})\Big)
\end{aligned} \tag{B.18}$$

To calculate $\mathbb{E}\{|R_1|^2\}$, we have

$$\begin{aligned}
\mathbb{E}\{|R_1|^2\} &= \sum_{n=1}^{N}\sum_{\substack{\ell\in\mathcal{U}_n,\\ \ell\neq k}} p_t\eta_{n\ell}\mathbb{E}\{\mathbf{g}^H_{b_n u_k}\mathbf{w}_{n\ell}\mathbf{w}_{n\ell}^H\mathbf{g}_{b_n u_k}\} \\
&\quad + \sum_{i=1}^{N}\sum_{\substack{j=1,\\ j\neq i}}^{N}\sum_{\substack{\ell\in\mathcal{U}_i\cap\mathcal{U}_j,\\ \ell\neq k}} p_t\sqrt{\eta_{i\ell}\eta_{j\ell}}\,\mathbb{E}\{\mathbf{g}^H_{b_i u_k}\mathbf{w}_{i\ell}\}\mathbb{E}\{\mathbf{w}^H_{j\ell}\mathbf{g}_{b_j u_k}\}
\end{aligned} \tag{B.19}$$

To calculate the expectations in (B.19), we must consider two cases: when users ℓ and k share a pilot sequence, and when they do not. In the latter case, the vectors in

(B.19) are uncorrelated. Thus, the expectation in the first line of (B.19) reduces to $|\mu_{1,n\ell}|^2\mathrm{tr}(\mathbf{R}_{b_n u_k}\hat{\mathbf{Q}}_{b_n u_\ell}) + |\mu_{2,n\ell}|^2\mathrm{tr}(\mathbf{R}_{b_n u_k}\hat{\mathbf{Q}}_{b_n t_\ell u_\ell})$, and both expectations in the second line of (B.19) reduce to 0. In contrast, with a shared pilot sequence, the vectors for a given AP are correlated, but not between two different APs i and j.

The overall expression for $\mathbb{E}\{|R_1|^2\}$ is given as

$$\begin{aligned}\mathbb{E}\{|R_1|^2\} = &\sum_{n=1}^{N}\sum_{\substack{\ell\in\mathcal{U}_n,\\ \ell\neq k}} p_t\eta_{n\ell}\times\begin{cases}|\mu_{1,n\ell}|^2\mathrm{tr}(\mathbf{R}_{b_n u_k}\hat{\mathbf{Q}}_{b_n u_\ell})+|\mu_{2,n\ell}|^2\mathrm{tr}(\mathbf{R}_{b_n u_k}\hat{\mathbf{Q}}_{b_n t_\ell u_\ell}), & \text{if } k\notin\mathcal{S}_\ell,\\ |\mu_{1,n\ell}|^2\,\mathbb{E}\{\mathbf{g}_{b_n u_k}^H\hat{\mathbf{q}}_{b_n u_\ell}\hat{\mathbf{q}}_{b_n u_\ell}^H\mathbf{g}_{b_n u_k}\} & \\ +|\mu_{2,n\ell}|^2\,\mathbb{E}\{\mathbf{g}_{b_n u_k}^H\hat{\mathbf{q}}_{b_n t_\ell u_\ell}\hat{\mathbf{q}}_{b_n t_\ell u_\ell}^H\mathbf{g}_{b_n u_k}\} & \text{if } k\in\mathcal{S}_\ell\\ +2\,\Re\mathfrak{e}\Big\{\mu_{1,n\ell}\,\mu_{2,n\ell}^*\,\mathbb{E}\{\mathbf{g}_{b_n u_k}^H\hat{\mathbf{q}}_{b_n u_\ell}\hat{\mathbf{q}}_{b_n t_\ell u_\ell}^H\mathbf{g}_{b_n u_k}\}\Big\}, & \end{cases}\\ +\sum_{i=1}^{N}\sum_{\substack{j=1,\\ j\neq i}}^{N}&\sum_{\substack{\ell\in\mathcal{U}_i\cap\mathcal{U}_j,\\ \ell\neq k}} p_t\sqrt{\eta_{i\ell}\eta_{j\ell}}\times\begin{cases}0, & \text{if } k\notin\mathcal{S}_\ell,\\ \mu_{1,i\ell}\,\mu_{1,j\ell}^*\,\mathbb{E}\{\mathbf{g}_{b_i u_k}^H\hat{\mathbf{q}}_{b_i u_\ell}\}\mathbb{E}\{\hat{\mathbf{q}}_{b_j u_\ell}^H\mathbf{g}_{b_j u_k}\} & \\ +\mu_{2,i\ell}\,\mu_{2,j\ell}^*\,\mathbb{E}\{\mathbf{g}_{b_i u_k}^H\hat{\mathbf{q}}_{b_i t_\ell u_\ell}\}\mathbb{E}\{\hat{\mathbf{q}}_{b_j t_\ell u_\ell}^H\mathbf{g}_{b_j u_k}\} & \text{if } k\in\mathcal{S}_\ell\\ +2\,\Re\mathfrak{e}\Big\{\mu_{1,i\ell}\,\mu_{2,j\ell}^*\,\mathbb{E}\{\mathbf{g}_{b_i u_k}^H\hat{\mathbf{q}}_{b_i u_\ell}\}\mathbb{E}\{\hat{\mathbf{q}}_{b_j t_\ell u_\ell}^H\mathbf{g}_{b_j u_k}\}\Big\}, & \end{cases}\end{aligned} \tag{B.20}$$

The joint PDFs $f(\mathbf{g}_{b_n u_k}, \hat{\mathbf{q}}_{b_n u_\ell})$ and $f(\mathbf{g}_{b_n u_k}, \hat{\mathbf{q}}_{b_n t_\ell u_\ell})$ have the same form as in (B.13). For $f(\mathbf{g}_{b_n u_k}, \hat{\mathbf{q}}_{b_n u_\ell})$, $\mathbf{R}_x = \mathbf{R}_{b_n u_k}$, and $\mathbf{A} = \mathbf{A}_1$ and $\mathbf{R}_v = \mathbf{R}_{v,1}$ are given by

$$\mathbf{A}_1 = \sqrt{\rho_{\ell,1}\rho_{k,1}}\,\tau_1\mathbf{R}_{b_n u_\ell}\boldsymbol{\Theta}_{n\ell}^{-1} \tag{B.21}$$

$$\mathbf{R}_{v,1} = \hat{\mathbf{R}}_{b_n u_\ell} - \mathbf{A}_1\mathbf{R}_{b_n u_k}\mathbf{A}_1^H \tag{B.22}$$

For $f(\mathbf{g}_{b_n u_k}, \hat{\mathbf{q}}_{b_n t_\ell u_\ell})$, $\mathbf{R}_x = \mathbf{R}_{b_n u_k}$ again, and $\mathbf{A} = \mathbf{A}_2$ and $\mathbf{R}_v = \mathbf{R}_{v,2}$ are given by

$$\mathbf{A}_2 = \sqrt{\rho_{\ell,2}}\,\tau_1\mathbf{R}_{b_n t_\ell u_\ell}\boldsymbol{\Phi}_{n\ell}^{-1}\big(\sqrt{\rho_{k,2}}\,\mathbf{I}_L - \sqrt{\rho_{\ell,2}\rho_{\ell,1}\rho_{k,1}}\,\tau_1\mathbf{R}_{n\ell}\boldsymbol{\Theta}_{n\ell}^{-1}\big)$$

$$\mathbf{R}_{v,2} = \hat{\mathbf{R}}_{b_n t_\ell u_\ell} - \mathbf{A}_2\mathbf{R}_{b_n u_k}\mathbf{A}_2^H \tag{B.23}$$

The joint PDF $f(\mathbf{g}_{b_n u_k}, \hat{\mathbf{q}}_{b_n u_\ell}, \hat{\mathbf{q}}_{b_n t_\ell u_\ell})$ is found from $f(\hat{\mathbf{q}}_{b_n t_\ell u_\ell}|\mathbf{g}_{b_n u_k}, \hat{\mathbf{q}}_{b_n u_\ell})f(\mathbf{g}_{b_n u_k}, \hat{\mathbf{q}}_{b_n u_\ell})$, which equals $f(\hat{\mathbf{q}}_{b_n t_\ell u_\ell}|\mathbf{g}_{b_n u_k})f(\mathbf{g}_{b_n u_k}, \hat{\mathbf{q}}_{b_n u_\ell})$ since $\hat{\mathbf{q}}_{b_n t_\ell u_\ell}$ is not dependent on $\hat{\mathbf{q}}_{b_n u_\ell}$. The joint PDF is therefore

$$f(\mathbf{g}_{b_n u_k}, \hat{\mathbf{q}}_{b_n u_\ell}, \hat{\mathbf{q}}_{b_n t_\ell u_\ell}) = \frac{\mathbf{X}_f}{\pi^{3n}\|\hat{\mathbf{q}}_{b_n u_\ell}\|^{4n}\|\hat{\mathbf{q}}_{b_n t_\ell u_\ell}\|^{4n}\det(\mathbf{R}_{v,1}\mathbf{R}_{v,2}\mathbf{R}_{b_n u_k})} \tag{B.24}$$

where

$$\mathbf{X}_f = \exp\Bigg[\Big(-\tfrac{\hat{\mathbf{q}}_{b_n u_\ell}}{\|\hat{\mathbf{q}}_{b_n u_\ell}\|^2} - \mathbf{A}_1 \mathbf{g}_{b_n u_k}\Big)^H \mathbf{R}_{v,1}^{-1} \Big(\tfrac{\hat{\mathbf{q}}_{b_n u_\ell}}{\|\hat{\mathbf{q}}_{b_n u_\ell}\|^2} - \mathbf{A}_1 \mathbf{g}_{b_n u_k}\Big) - \Big(\tfrac{\hat{\mathbf{q}}_{b_n t_\ell u_\ell}}{\|\hat{\mathbf{q}}_{b_n t_\ell u_\ell}\|^2} - \mathbf{A}_2 \mathbf{g}_{b_n u_k}\Big)^H \mathbf{R}_{v,2}^{-1} \Big(\tfrac{\hat{\mathbf{q}}_{b_n t_\ell u_\ell}}{\|\hat{\mathbf{q}}_{b_n t_\ell u_\ell}\|^2} - \mathbf{A}_2 \mathbf{g}_{b_n u_k}\Big) - \mathbf{g}_{b_n u_k}^H \mathbf{R}_{b_n u_k}^{-1} \mathbf{g}_{b_n u_k}\Bigg] \tag{B.25}$$

The calculation of $\mathbb{E}\{|R_2|^2\}$ is similar to that of $\mathbb{E}\{|R_1|^2\}$, with the inclusion of α_{t_k} and $\mathbf{g}_{b_n t_k u_k}$ replacing $\mathbf{g}_{b_n u_k}$. Importantly, since $\mathbf{g}_{b_n t_k u_k}$ is only part of the estimation of cascaded links, it will only ever be correlated with $\hat{\mathbf{q}}_{b_n t_\ell u_\ell}$ (if $k \in \mathcal{S}_\ell$), but not $\hat{\mathbf{q}}_{b_n u_\ell}$. As such, terms involving $\mu_{1,n\ell}$ (the direct-link part of $\mathbf{w}_{n\ell}$) will not contain correlation. The expression for $\mathbb{E}\{|R_2|^2\}$ is given as

$$\mathbb{E}\{|R_2|^2\} = \sum_{n=1}^{N} \sum_{\substack{\ell \in \mathcal{U}_n, \\ \ell \neq k}} p_t \alpha_{t_k} \eta_{n\ell} \Bigg(|\mu_{1,n\ell}|^2 \mathrm{tr}(\mathbf{R}_{b_n t_k u_k} \hat{\mathbf{Q}}_{b_n u_\ell}) + |\mu_{2,n\ell}|^2 \times \begin{cases} \mathrm{tr}(\mathbf{R}_{b_n t_k u_k} \hat{\mathbf{Q}}_{b_n t_\ell u_\ell}), & \text{if } \ell \notin \mathcal{S}_k, \\ \mathbb{E}\{\mathbf{g}_{b_n t_k u_k}^H \hat{\mathbf{q}}_{b_n t_\ell u_\ell} \hat{\mathbf{q}}_{b_n t_\ell u_\ell}^H \mathbf{g}_{b_n t_k u_k}\}, & \text{if } \ell \in \mathcal{S}_k, \end{cases} \Bigg) \tag{B.26}$$

$$+ \sum_{i=1}^{N} \sum_{\substack{j=1, \\ j \neq i}}^{N} \sum_{\substack{\ell \in \mathcal{U}_i \cap \mathcal{U}_j, \\ \ell \neq k}} p_t \alpha_{t_k} \sqrt{\eta_{i\ell} \eta_{j\ell}} \times \begin{cases} 0, & \text{if } \ell \notin \mathcal{S}_k, \\ \mu_{2,i\ell} \mu_{2,j\ell}^* \, \mathbb{E}\{\mathbf{g}_{b_i t_k u_k}^H \hat{\mathbf{q}}_{b_i t_\ell u_\ell}\} \mathbb{E}\{\hat{\mathbf{q}}_{b_j t_\ell u_\ell}^H \mathbf{g}_{b_j t_k u_k}\}, & \text{if } \ell \in \mathcal{S}_k \end{cases}$$

The joint PDF $f(\mathbf{g}_{b_n t_k u_k}, \hat{\mathbf{q}}_{b_n t_\ell u_\ell})$ once again has the same form as in (B.13), this time with $\mathbf{A} = \sqrt{\rho_{\ell,2}\rho_{k,2}}\, \tau_2 \mathbf{R}_{b_n t_\ell u_\ell} \mathbf{\Theta}_{n\ell}^{-1}$ and $\mathbf{R}_v = \hat{\mathbf{R}}_{b_n t_\ell u_\ell} - \mathbf{A}\mathbf{R}_{b_n t_k u_k}\mathbf{A}^H$.

Finally, the SINR when decoding s_k is $\frac{\mathbb{E}\{|a_1|^2\}}{\mathbb{E}\{|a_2|^2\}+\mathbb{E}\{|a_3|^2\}+\mathbb{E}\{|R_1|^2\}+\mathbb{E}\{|R_2|^2\}+\sigma_n^2}$ as presented in (5.20)(cf. [181, Eq. (19)–(23)]). In (5.20) and (5.21), when forming $I_{\mathcal{A}_k} = \mathbb{E}\{|a_2|^2\} + \mathbb{E}\{|a_3|^2\}$, we combine $\mathrm{tr}(\hat{\mathbf{R}}_{b_n t_k u_k} \hat{\mathbf{Q}}_{b_n u_k}) + \mathrm{tr}(\tilde{\mathbf{R}}_{b_n t_k u_k} \hat{\mathbf{Q}}_{b_n u_k})$ to make $\mathrm{tr}(\mathbf{R}_{b_n t_k u_k} \hat{\mathbf{Q}}_{b_n u_k})$.

B.3 SINR Derivation of BD Transmissions

The useful part of the received signal after SIC, i.e., the first double sum in (5.24), consists of the sum of S_2 and R_2 from (5.19). Meanwhile, the interference plus noise $y_{\mathrm{I+N}}$ is as indicated in (5.24). We here denote the first interference term in $y_{\mathrm{I+N}}$ as y_{res} with power $\mathbb{E}\{|y_{\mathrm{res}}|^2\} = I_{\mathrm{res}}$, whereas the second term is the same as R_1 in (5.19).

After adding together the M phase-corrected received signals with EGC, the power of the useful part of the combined signals is $\mathbb{E}\{\big(\sum_{m=1}^{M}|g_{\mathrm{BD}}(m)|\big)^2\}$. Meanwhile, the power of the combined interference plus noise is $\mathbb{E}\{\big|\sum_{m=1}^{M}y_{\mathrm{I+N}}(m)\big|^2\}$. Because both g_{BD} and $y_{\mathrm{I+N}}$ consist of the sum of many random variables, by the Central Limit Theorem, we can treat them as being distributed as a single complex Gaussian random variable with the same mean and the same total variance. For the useful power, since $g_{\mathrm{BD}} = S_2 + R_2$, its mean is $\mathbb{E}\{g_{\mathrm{BD}}\} = \mathbb{E}\{S_2\} + \mathbb{E}\{R_2\} = 0$ since S_2 and R_2 both have zero mean, and its variance is

$$\begin{aligned}\mathbb{E}\{|g_{\mathrm{BD}}|^2\} &= \mathbb{E}\{(S_2+R_2)(S_2^*+R_2^*)\} = \mathbb{E}\{|S_2|^2+|R_2|^2+S_2R_2^*+S_2^*R_2\} \qquad \text{(B.27)}\\ &= \mathbb{E}\{|S_2|^2\}+\mathbb{E}\{|R_2|^2\}+\mathbb{E}\{S_2\}\mathbb{E}\{R_2^*\}+\mathbb{E}\{S_2^*\}\mathbb{E}\{R_2)\} = \mathbb{E}\{(|S_2|^2\}+\mathbb{E}\{|R_2|^2\},\end{aligned}$$

where the last line holds due to S_2 and R_2 being uncorrelated. The real and imaginary parts of g_{BD} will therefore each have a variance of $(\mathbb{E}\{(|S_2|^2\}+\mathbb{E}\{|R_2|^2\})/2$.

Expanding the squared sum of the useful components, we get

$$\mathbb{E}\left\{\left(\sum_{m=1}^{M}|g_{\mathrm{BD}}(m)|\right)^2\right\} = \sum_{m=1}^{M}\mathbb{E}\{|g_{\mathrm{BD}}(m)|^2\} + \sum_{i=1}^{M}\sum_{\substack{j=1,\\ j\neq i}}^{M}\mathbb{E}\{|g_{\mathrm{BD}}(i)|\}\mathbb{E}\{|g_{\mathrm{BD}}(j)|\} \qquad \text{(B.28)}$$

Since g_{BD} has a complex Gaussian distribution, its magnitude $|g_{\mathrm{BD}}|$ will be Rayleigh distributed, with a mean of $\sigma_{g_{(\Re,\Im)}}\sqrt{\pi/2}$ [172, Ch. 2.3], where $\sigma_{g_{(\Re,\Im)}}$ is the standard deviation of its real and imaginary parts. Hence, $\mathbb{E}\{|g_{\mathrm{BD}}|\} = \frac{\sqrt{\pi(\mathbb{E}\{(|S_2|^2\}+\mathbb{E}\{|R_2|^2\})}}{2}$.

For the interference plus noise, since $y_{\mathbf{res}}$, R_1, and n_k are all zero mean and uncorrelated with each other, by a similar calculation as in (B.27), we get $\mathbb{E}\{|y_{\mathrm{I+N}}|^2\} = I_{\mathrm{res}} + \mathbb{E}\{(|R_1|^2\} + \sigma_n^2$. Multiplying $y_{\mathrm{I+N}}$ by $\exp(-j\angle g_{\mathrm{BD}})$ as part of the phase cancellation of y_k^{SIC} will not change the distribution of $y_{\mathrm{I+N}}$, as its phase will still be uniformly distributed in $[0, 2\pi)$ (modulo 2π). Furthermore, since the sum of the M interference components is a sum of M independent complex Gaussian random variables, the sum will end up as a complex Gaussian variable whose mean is the sum of the individual component means and the variance is the sum of the individual component variances.

Putting all this together, we end up that the SINR for the BD transmission from t_k after EGC will be

$$\begin{aligned}\mathrm{SINR}_k^{(2)}&=\frac{\mathbb{E}\Big\{\Big(\sum\limits_{m=1}^{M}|g_{\mathrm{BD}}(m)|\Big)^2\Big\}}{\mathbb{E}\Big\{\Big|\sum\limits_{m=1}^{M}y_{\mathrm{I+N}}(m)\Big|^2\Big\}}=\frac{\sum\limits_{m=1}^{M}\mathbb{E}\{|g_{\mathrm{BD}}(m)|^2\}+\sum\limits_{i=1}^{M}\sum\limits_{\substack{j=1,\\ j\neq i}}^{M}\mathbb{E}\{|g_{\mathrm{BD}}(i)|\}\mathbb{E}\{|g_{\mathrm{BD}}(j)|\}}{\sum\limits_{m=1}^{M}\mathbb{E}\{|y_{\mathrm{I+N}}(m)|^2\}}\\ &=\frac{\left(\begin{array}{c}\sum\limits_{m=1}^{M}\Big(\mathbb{E}\{|S_2(m)|^2\}+\mathbb{E}\{|R_2(m)|^2\}\Big)+\\ \frac{\pi}{4}\sum\limits_{i=1}^{M}\sum\limits_{\substack{j=1,\\ j\neq i}}^{M}\sqrt{\big(\mathbb{E}\{|S_2(i)|^2\}+\mathbb{E}\{|R_2(i)|^2\}\big)\big(\mathbb{E}\{|S_2(j)|^2\}+\mathbb{E}\{|R_2(j)|^2\}\big)}\end{array}\right)}{M\sigma_n^2+\sum\limits_{m=1}^{M}\Big(I_{\mathrm{res}}(m)+\mathbb{E}\{|R_1(m)|^2\}\Big)}\end{aligned} \tag{B.29}$$

$\mathbb{E}\{|R_1|^2\}$ and $\mathbb{E}\{|R_2|^2\}$ were derived in Appendix B.2 and are given by (B.20) and (B.26), respectively. Making note of the same correlations between certain vectors (or lack thereof) as described in Appendix B.2, for $\mathbb{E}\{|S_2|^2\}$, we have

$$\begin{aligned}&\mathbb{E}\{|S_2|^2\}\\ &=p_t\alpha_{t_k}\Big(\sum_{n\in\mathcal{A}_k}\eta_{nk}\mathbb{E}\{\mathbf{g}_{b_nt_ku_k}^H\mathbf{w}_{nk}\mathbf{w}_{nk}^H\mathbf{g}_{b_nt_ku_k}\}+\sum_{i\in\mathcal{A}_k}\sum_{\substack{j\in\mathcal{A}_k,\\ j\neq i}}\sqrt{\eta_{ik}\eta_{jk}}\,\mathbb{E}\{\mathbf{g}_{b_it_ku_k}^H\mathbf{w}_{ik}\mathbf{w}_{jk}^H\mathbf{g}_{b_jt_ku_k}\}\Big)\\ &=p_t\alpha_{t_k}\Big(\sum_{n\in\mathcal{A}_k}\eta_{nk}\Big[|\mu_{1,nk}|^2\,\mathbb{E}\{\mathbf{g}_{b_nt_ku_k}^H\hat{\mathbf{q}}_{b_nu_k}\hat{\mathbf{q}}_{b_nu_k}^H\mathbf{g}_{b_nt_ku_k}\}\\ &+|\mu_{2,nk}|^2\,\mathbb{E}\{\mathbf{g}_{b_nt_ku_k}^H\hat{\mathbf{q}}_{b_nt_ku_k}\hat{\mathbf{q}}_{b_nt_ku_k}^H\mathbf{g}_{b_nt_ku_k}\}\Big]\\ &+\sum_{i\in\mathcal{A}_k}\sum_{\substack{j\in\mathcal{A}_k,\\ j\neq i}}\sqrt{\eta_{ik}\eta_{jk}}\,\mu_{2,ik}\mu_{2,jk}^*\mathbb{E}\{\mathbf{g}_{b_it_ku_k}^H\hat{\mathbf{q}}_{b_it_ku_k}\}\mathbb{E}\{\hat{\mathbf{q}}_{b_jt_ku_k}^H\mathbf{g}_{b_jt_ku_k}\}\Big)\\ &=p_t\alpha_{t_k}\Big(\sum_{n\in\mathcal{A}_k}\eta_{nk}\Big[|\mu_{1,nk}|^2\mathrm{tr}(\mathbf{R}_{b_nt_ku_k}\hat{\mathbf{Q}}_{b_nu_k})+|\mu_{2,nk}|^2\Big(1+\mathrm{tr}(\tilde{\mathbf{R}}_{b_nt_ku_k}\hat{\mathbf{Q}}_{b_nt_ku_k})\Big)\Big]\\ &+\sum_{i\in\mathcal{A}_k}\sum_{\substack{j\in\mathcal{A}_k,\\ j\neq i}}\sqrt{\eta_{ik}\eta_{jk}}\,\mu_{2,ik}\mu_{2,jk}^*\Big)\end{aligned} \tag{B.30}$$

We note that within the first summation of the last line of (B.30), the term $\eta_{nk}|\mu_{2,nk}|^2\times 1$ is the same as $\sqrt{\eta_{nk}\eta_{nk}}\,\mu_{2,nk}\mu_{2,nk}^*$. We can therefore pull that term out of the first summation and add it to the second double summation, while dropping

the $j\neq i$ restriction on the second. We then end up with

$$\mathbb{E}\{|S_2|^2\} = p_t\alpha_{t_k}\Bigg(\sum_{n\in\mathcal{A}_k} \eta_{nk}\Big[|\mu_{1,nk}|^2 \mathrm{tr}(\mathbf{R}_{b_n t_k u_k}\hat{\mathbf{Q}}_{b_n u_k}) + |\mu_{2,nk}|^2 \mathrm{tr}(\tilde{\mathbf{R}}_{b_n t_k u_k}\hat{\mathbf{Q}}_{b_n t_k u_k})\Big] + \sum_{i\in\mathcal{A}_k}\sum_{j\in\mathcal{A}_k} \sqrt{\eta_{ik}\eta_{jk}}\,\mu_{2,ik}\mu_{2,jk}^*\Bigg) \tag{B.31}$$

For y_{res}, we first note from (B.7) that $\mathbb{E}\{\hat{\mathbf{g}}_{b_n u_k}^H \mathbf{w}_{nk}\} = \mu_{1,nk}$. We have $\mathbb{E}\{\mathbf{g}_{b_n u_k}^H \mathbf{w}_{nk}\} = \mathbb{E}\big\{(\hat{\mathbf{g}}_{b_n u_k}^H + \tilde{\mathbf{g}}_{b_n u_k}^H)\big(\mu_{1,nk}\frac{\hat{\mathbf{g}}_{b_n u_k}}{\|\hat{\mathbf{g}}_{b_n u_k}\|^2} + \mu_{2,nk}\frac{\hat{\mathbf{g}}_{b_n t_k u_k}}{\|\hat{\mathbf{g}}_{b_n t_k u_k}\|^2}\big)\big\} = \mu_{1,nk} + \mu_{2,nk}\mathbb{E}\{\tilde{\mathbf{g}}_{b_n u_k}^H \hat{\mathbf{q}}_{b_n t_k u_k}\}$. Then, for $I_{\mathrm{res}} = \mathbb{E}\{|y_{\mathrm{res}}|^2\}$, we have

$$\begin{aligned}
I_{\mathrm{res}} &= p_t\Bigg(\sum_{n\in\mathcal{A}_k}\eta_{nk}\Big[\mathbb{E}\{\mathbf{g}_{b_n u_k}^H \mathbf{w}_{nk}\mathbf{w}_{nk}^H \mathbf{g}_{b_n u_k}\} - \mathbb{E}\{\mathbf{g}_{b_n u_k}^H \mathbf{w}_{nk}\}\mu_{1,nk}^* - \mu_{1,nk}\mathbb{E}\{\mathbf{w}_{nk}^H \mathbf{g}_{b_n u_k}\} + |\mu_{1,nk}|^2\Big] \\
&+ \sum_{i\in\mathcal{A}_k}\sum_{\substack{j\in\mathcal{A}_k,\\ j\neq i}}\sqrt{\eta_{ik}\eta_{jk}}\Big[\mathbb{E}\{\mathbf{g}_{b_i u_k}^H \mathbf{w}_{ik}\mathbf{w}_{jk}^H \mathbf{g}_{b_j u_k}\} - \mathbb{E}\{\mathbf{g}_{b_i u_k}^H \mathbf{w}_{ik}\}\mu_{1,jk}^* - \mu_{1,ik}\mathbb{E}\{\mathbf{w}_{jk}^H \mathbf{g}_{b_j u_k}\} + \mu_{1,ik}\mu_{1,jk}^*\Big]\Bigg) \\
&= p_t\Bigg(\sum_{n\in\mathcal{A}_k}\eta_{nk}\Big[|\mu_{1,nk}|^2 + |\mu_{2,nk}|^2\big(\mathbb{E}\{\hat{\mathbf{g}}_{b_n u_k}^H \hat{\mathbf{q}}_{b_n t_k u_k}\hat{\mathbf{q}}_{b_n t_k u_k}^H \hat{\mathbf{g}}_{b_n u_k}\} \\
&+ \mathbb{E}\{\tilde{\mathbf{g}}_{b_n u_k}^H \hat{\mathbf{q}}_{b_n t_k u_k}\hat{\mathbf{q}}_{b_n t_k u_k}^H \tilde{\mathbf{g}}_{b_n u_k}\}\big) + |\mu_{1,nk}|^2\,\mathbb{E}\{\tilde{\mathbf{g}}_{b_n u_k}^H \hat{\mathbf{q}}_{b_n u_k}\hat{\mathbf{q}}_{b_n u_k}^H \tilde{\mathbf{g}}_{b_n u_k}\} \\
&+ \mu_{2,nk}\mu_{1,nk}^*\mathbb{E}\{\tilde{\mathbf{g}}_{b_n u_k}^H \hat{\mathbf{q}}_{b_n t_k u_k}\} + \mu_{1,nk}\mu_{2,nk}^*\mathbb{E}\{\hat{\mathbf{q}}_{b_n t_k u_k}^H \tilde{\mathbf{g}}_{b_n u_k}\} \\
&+ \mu_{2,nk}\mu_{1,nk}^*\mathbb{E}\Big\{\frac{\hat{\mathbf{g}}_{b_n u_k}^H \hat{\mathbf{q}}_{b_n t_k u_k}\hat{\mathbf{g}}_{b_n u_k}^H \tilde{\mathbf{g}}_{b_n u_k}}{\|\hat{\mathbf{g}}_{b_n u_k}\|^2}\Big\} + \mu_{1,nk}\mu_{2,nk}^*\mathbb{E}\Big\{\frac{\tilde{\mathbf{g}}_{b_n u_k}^H \hat{\mathbf{g}}_{b_n u_k}\hat{\mathbf{q}}_{b_n t_k u_k}^H \hat{\mathbf{g}}_{b_n u_k}}{\|\hat{\mathbf{g}}_{b_n u_k}\|^2}\Big\} \\
&- \big(\mu_{1,nk} + \mu_{2,nk}\mathbb{E}\{\tilde{\mathbf{g}}_{b_n u_k}^H \hat{\mathbf{q}}_{b_n t_k u_k}\}\big)\mu_{1,nk}^* - \mu_{1,nk}\big(\mu_{1,nk}^* + \mu_{2,nk}^*\mathbb{E}\{\hat{\mathbf{q}}_{b_n t_k u_k}^H \tilde{\mathbf{g}}_{b_n u_k}\}\big) + |\mu_{1,nk}|^2\Big] \\
&+ \sum_{i\in\mathcal{A}_k}\sum_{\substack{j\in\mathcal{A}_k,\\ j\neq i}}\sqrt{\eta_{ik}\eta_{jk}}\Big[\big(\mu_{1,ik} + \mu_{2,ik}\mathbb{E}\{\tilde{\mathbf{g}}_{b_i u_k}^H \hat{\mathbf{q}}_{b_i t_k u_k}\}\big)\big(\mu_{1,jk}^* + \mu_{2,jk}^*\mathbb{E}\{\hat{\mathbf{q}}_{b_j t_k u_k}^H \tilde{\mathbf{g}}_{b_j u_k}\}\big) \\
&- \big(\mu_{1,ik} + \mu_{2,ik}\mathbb{E}\{\tilde{\mathbf{g}}_{b_i u_k}^H \hat{\mathbf{q}}_{b_i t_k u_k}\}\big)\mu_{1,jk}^* - \mu_{1,ik}\big(\mu_{1,jk}^* + \mu_{2,jk}^*\mathbb{E}\{\hat{\mathbf{q}}_{b_j t_k u_k}^H \tilde{\mathbf{g}}_{b_j u_k}\}\big) + \mu_{1,ik}\mu_{1,jk}^*\Big]\Bigg)
\end{aligned} \tag{B.32}$$

In (B.32), there are terms with $\mathbb{E}\Big\{\frac{\tilde{\mathbf{g}}_{b_n u_k}^H \hat{\mathbf{g}}_{b_n u_k}\hat{\mathbf{q}}_{b_n t_k u_k}^H \hat{\mathbf{g}}_{b_n u_k}}{\|\hat{\mathbf{g}}_{b_n u_k}\|^2}\Big\}$ (or its conjugate). For simplicity of notation, we'll denote $\hat{\mathbf{c}} = \frac{\hat{\mathbf{g}}_{b_n u_k}}{\|\hat{\mathbf{g}}_{b_n u_k}\|}$ and temporarily drop the subscripts on the vectors. The expectation is $\mathbb{E}\{\tilde{\mathbf{g}}^H\hat{\mathbf{c}}\hat{\mathbf{q}}^H\hat{\mathbf{c}}\} = \mathbb{E}\{\hat{\mathbf{q}}^H\hat{\mathbf{c}}\tilde{\mathbf{g}}^H\hat{\mathbf{c}}\} = \mathbb{E}_{\tilde{\mathbf{g}},\hat{\mathbf{q}}}\big\{\hat{\mathbf{q}}^H\mathbb{E}_{\hat{\mathbf{c}}}\{\hat{\mathbf{c}}\tilde{\mathbf{g}}^H\hat{\mathbf{c}}|\tilde{\mathbf{g}}\}\big\}$. Next, because $\hat{\mathbf{g}}$ is a circularly-symmetric complex Gaussian vector, it has a pseudo-covariance matrix $\mathbb{E}\{\mathbf{g}\mathbf{g}^T\} = \mathbf{0}_{L\times L}$. Thus, the pseudo-covariance matrix of $\hat{\mathbf{c}}$ will also be $\mathbf{0}_{L\times L}$. In other words, for any two elements $\hat{c}_i$ and $\hat{c}_j$ of $\hat{\mathbf{c}}$, $\mathbb{E}\{\hat{c}_i^2\}$, $\mathbb{E}\{\hat{c}_j^2\}$, and

$\mathbb{E}\{\hat{c}_i\hat{c}_j\}$ will all be zero. Thus, we will have

$$\mathbb{E}_{\hat{\mathbf{c}}}\{\hat{\mathbf{c}}\tilde{\mathbf{g}}^H\hat{\mathbf{c}}|\tilde{\mathbf{g}}\} = \begin{bmatrix} \tilde{g}_1^*\mathbb{E}\{\hat{z}_1^2\} & +\tilde{g}_2^*\mathbb{E}\{\hat{z}_1\hat{z}_2\} + \cdots + \tilde{g}_L^*\mathbb{E}\{\hat{z}_1\hat{z}_L\} \\ \tilde{g}_1^*\mathbb{E}\{\hat{z}_2\hat{z}_1\} + & \tilde{g}_2^*\mathbb{E}\{\hat{z}_2^2\} & + \cdots + \tilde{g}_L^*\mathbb{E}\{\hat{z}_2\hat{z}_L\} \\ \vdots & \vdots & \vdots \\ \tilde{g}_1^*\mathbb{E}\{\hat{z}_L\hat{z}_1\} + & \tilde{g}_2^*\mathbb{E}\{\hat{z}_L\hat{z}_2\} + \cdots + & \tilde{g}_L^*\mathbb{E}\{\hat{z}_L^2\} \end{bmatrix} = \begin{bmatrix} 0 \\ 0 \\ \vdots \\ 0 \end{bmatrix}, \tag{B.33}$$

and so $\mathbb{E}\{\tilde{\mathbf{g}}^H\hat{\mathbf{c}}\hat{\mathbf{q}}^H\hat{\mathbf{c}}\} = 0$. Hence, (B.32) reduces to

$$\mathbb{E}\{|I_{\text{res}}|^2\} = p_t\Bigg(\sum_{n\in\mathcal{A}_k}\eta_{nk}\Big[|\mu_{1,nk}|^2\text{tr}(\tilde{\mathbf{R}}_{b_nu_k}\hat{\mathbf{Q}}_{b_nu_k}) + |\mu_{2,nk}|^2\big(\text{tr}(\hat{\mathbf{R}}_{b_nu_k}\hat{\mathbf{Q}}_{b_nt_ku_k}) \tag{B.34}$$
$$+\mathbb{E}\{\tilde{\mathbf{g}}_{b_nu_k}^H\hat{\mathbf{q}}_{b_nt_ku_k}\hat{\mathbf{q}}_{b_nt_ku_k}^H\tilde{\mathbf{g}}_{b_nu_k}\}\big)\Big] + \sum_{i\in\mathcal{A}_k}\sum_{j\in\mathcal{A}_k\setminus i}\sqrt{\eta_{ik}\eta_{jk}}\,\mu_{2,ik}\mu_{2,jk}^*\mathbb{E}\{\tilde{\mathbf{g}}_{b_iu_k}^H\hat{\mathbf{q}}_{b_it_ku_k}\}\mathbb{E}\{\hat{\mathbf{q}}_{b_jt_ku_k}^H\tilde{\mathbf{g}}_{b_ju_k}\}\Bigg)$$